

COMPLEX SCATTERED RADIATION FIELDS AND MULTIPLE MAGNETIC FIELDS
IN THE PROTOSTELLAR CLUSTER IN NGC 2264

JUNGMI KWON^{1,2}, MOTOHIDE TAMURA^{1,2}, RYO KANDORI¹, NOBUHIKO KUSAKABE¹, JUN HASHIMOTO¹, YASUSHI NAKAJIMA¹, FUMITAKA NAKAMURA¹, TAKAHIRO NAGAYAMA³, TETSUYA NAGATA⁴, JAMES H. HOUGH⁵, MICHAEL W. WERNER⁶, AND PAULA S. TEIXEIRA⁷

¹ National Astronomical Observatory of Japan, 2-21-1 Osawa, Mitaka, Tokyo 181-8588, Japan; jungmi.kwon@nao.ac.jp

² Department of Astronomical Science, Graduate University for Advanced Studies (Sokendai), 2-21-1 Osawa, Mitaka, Tokyo 181-8588, Japan

³ Department of Astrophysics, Nagoya University, Nagoya 464-8602

⁴ Department of Astronomy, Kyoto University, Kyoto 606-8502

⁵ Centre for Astrophysics Research, University of Hertfordshire, Hatfield, Herts AL10 9AB, UK

⁶ Jet Propulsion Laboratory, California Institute of Technology, Pasadena, CA 91109, USA

⁷ European Southern Observatory, Karl-Schwarzschild-Straße 2, D-85748 Garching bei München, Germany

ABSTRACT

Near-infrared (IR) imaging polarimetry in the J , H , and K_s bands has been carried out for the protostellar cluster region around NGC 2264 IRS 2 in the Monoceros OB1 molecular cloud. Various infrared reflection nebulae clusters (IRNCs) associated with NGC 2264 IRS 2 and IRAS 12 S1 core were detected as well as local infrared reflection nebulae (IRNe). The illuminating sources of the IRNe were identified with known or new near- and mid-IR sources. In addition, 314 point-like sources were detected in all three bands and their aperture polarimetry was studied. Using a color–color diagram, reddened field stars and diskless pre-main sequence stars were selected to trace the magnetic field (MF) structure of the molecular cloud. The mean polarization position angle of the point-like sources is $81^\circ \pm 29^\circ$ in the cluster core, and $58^\circ \pm 24^\circ$ in the perimeter of the cluster core, which is interpreted as the projected direction on the sky of the MF in the observed region of the cloud. The Chandrasekhar–Fermi method gives a rough estimate of the MF strength to be about $100 \mu\text{G}$. A comparison with recent numerical simulations of the cluster formation implies that the cloud dynamics is controlled by the relatively strong MF. The local MF direction is well associated with that of CO outflow for IRAS 12 S1 and consistent with that inferred from submillimeter polarimetry. In contrast, the local MF direction runs roughly perpendicular to the Galactic MF direction.

Subject headings: circumstellar matter — infrared: stars — ISM: individual (NGC 2264) — ISM: structure — polarization — stars: formation

1. INTRODUCTION

NGC 2264, including the Cone Nebula, Fox Fur Nebula and Christmas Tree Cluster in the Monoceros OB1 molecular cloud, is a site of active star formation (Walker 1954, 1956) and is a cornerstone for the study of the formation and time evolution of young stellar objects (YSOs). The median age of NGC 2264 is 1–3 Myr with an age dispersion of ~ 5 Myr (Dahm & Simon 2005). It is located at a distance of ~ 760 pc (Sung et al. 1997, but see also Baxter et al. 2009, Sung et al. 2010) and lies 37 pc above the galactic plane (Pérez 1991) in front of a dark molecular cloud complex. The mass of the cloud complex is estimated to be at least $\sim 3.7 \times 10^4 M_\odot$ (Dahm 2008). NGC 2264 has an intermediate stellar density and its stellar population, which is known down to very low masses, is dominated by the O7V multiple star S Monocerotis (Schwartz et al. 1985).

The NGC 2264 region has been exceptionally well studied at various wavelengths from centimeters to X-rays. Previous studies have revealed that active star formation is ongoing in this region, as evidenced by the presence of numerous embedded clusters of protostars, molecular outflows, and Herbig–Haro objects (e.g., Adams et al. 1979; Margulis et al. 1989; Walsh et al. 1992; Hodapp 1994; Reipurth et al. 2004; Young et al. 2006, hereafter YTL). There are two prominent sites of star formation activity centered near NGC 2264, identified by IR and millimeter observations, IRAS 06384+0932 (hereafter IRS 1) and IRAS 06382+0939 (hereafter IRS 2). NGC 2264 IRS 1, known as Allen’s source (Allen 1972), is a deeply embedded early-type (B2–B5) star. NGC 2264 IRS 2, discovered by Sargent et al. (1984), was identified as a Class I source. NGC 2264 IRS 2 was

designated as IRAS 12 (06^h 41^m 02^s.7 +09° 36′ 10″) by Margulis et al. (1989), and Castelaz & Grasdalen (1988) showed that NGC 2264 IRS 2 is a binary source (RNO-E and RNO-W) separated by $2''.8$.

Krügel et al. (1987) presented an extended ammonia map of the central region of the molecular cloud associated with NGC 2264 including both IRS 1 and IRS 2. Williams & Garland (2002) also observed the dust and gas near the two young stellar clusters IRS 1 and IRS 2 in NGC 2264 and presented an $870 \mu\text{m}$ continuum emission map. The elongated shape of IRS 1 shows signs of substructure, while IRS 2 is more fragmented, indicating a more evolved cluster of protostars. IRAS 12 S1 located south-west of NGC 2264 IRS 2 was found by Cohen et al. (1985), and it is located precisely at the peak of the IRAS 12 S1 in the submillimeter maps of Wolf-Chase et al. (2003). It is also associated with the core C of Williams & Garland (2002), the NGC 2264 D-MM1 of Peretto et al. (2006), and the dense microcluster of Class 0 protostars of Teixeira et al. (2007). Wolf-Chase et al. (2003) derived an envelope mass of $17.6 M_\odot$ within a $29''$ diameter, and Peretto et al. (2006) estimated a mass infall rate of $\dot{M}_{D-MM1} \sim 1.1 \times 10^{-4} M_\odot \text{yr}^{-1}$ from millimeter observations, toward the rotating IRAS 12 S1. However, YTL and Teixeira et al. (2007) showed that IRAS 12 S1 is in fact a multiple source, composed of at least 7 protostars.

Teixeira et al. (2006) identified bright $24 \mu\text{m}$ protostars that are radially distributed around NGC 2264 IRS 2, and embedded within dusty filaments. The cluster of protostars was therefore named the Spokes cluster. The projected separation of the $24 \mu\text{m}$ protostars is $20 \pm 5''$, similar to the Jeans length of the

cloud, $27''$, implying the filaments had undergone thermal fragmentation. In addition, the evolutionary stages of protostars in the NGC 2264 IRS 2 region were studied through detailed spectral energy distributions (SEDs) (Forbrich et al. 2010, hereafter FTR), and the outflow activity was derived in the vicinity of IRAS 12 S1. Bourke et al. (2001), from OH Zeeman observations using the NRAO Green Bank 43-m telescope (FWHM beam size $\sim 18'$), estimated the magnetic field strength for NGC 2264 to be $21 \pm 16 \mu\text{G}$.

The outflows and the Herbig–Haro objects are considered as indicators of recent star formation activity. The characteristics of outflows and jets associated with YSOs are related to the magnetic field and the rotation of the protostar and circumstellar disk. The outflows and jets commonly tend to be aligned with each other and with the cloud-scale magnetic field, as determined from polarization observations (e.g., Cohen et al. 1984; Strom et al. 1986; Vrba et al. 1986, 1988; Tamura & Sato 1989; Jones & Amini 2003). Herbig (1974) performed early surveys of the NGC 2264 region and identified several candidate Herbig–Haro objects, as well as a survey of emission line stars (Herbig 1954).

Multi-color near-IR polarimetry is useful for understanding magnetic fields and the properties of dust grains that cause scattering and absorption in various environments (e.g., Tamura et al. 2007). Polarimetric studies of the NGC 2264 region have been reported previously by several authors (e.g., Breger & Hardorp 1973; Kobayashi et al. 1978; Dyck & Lonsdale 1979; Heckert & Zeilik 1981, 1984; Schreyer et al. 2003; Dotson et al. 2010) but almost all of these studies only covered the NGC 2264 IRS 1 region. The polarization position angle of NGC 2264 IRS 1 was found to be $\sim 106^\circ$ – 117° in the near-IR (Breger & Hardorp 1973; Kobayashi et al. 1978; Heckert and Zeilik 1981). Dotson et al. (2010) recently reported $350 \mu\text{m}$ polarimetry in the direction of IRS 1 and IRAS 12 S1 near IRS 2 in NGC 2264.

In this paper, we first present wide-field near-IR imaging polarimetry of the IRS 2 region, as part of our ongoing survey project of JHK_s polarimetry for star forming regions. In Section 2, we describe the observations. In Section 3, we present the results of the imaging and aperture polarimetry. In Section 4, we discuss the illuminating sources of infrared reflection nebulae and the magnetic field structure related to the star forming activity in the NGC 2264 IRS 2 region. A summary is given in Section 5.

2. OBSERVATIONS

The observations in the direction of the IRAS 12 S1 region were carried out using the SIRPOL imaging polarimeter on the Infrared Survey Facility (IRSF) 1.4-m telescope at the South African Astronomical Observatory. SIRPOL consists of a single-beam polarimeter (an achromatic half-wave plate rotator unit and a polarizer) and an imaging camera (Nagayama et al. 2003). The camera, SIRIUS, has three 1024×1024 HgCdTe infrared detectors. IRSF/SIRPOL enables deep and wide-field (7.7×7.7 with a scale of 0.45 pixel^{-1}) imaging polarimetry in the J , H , and K_s bands simultaneously (Kandori et al. 2006).

The observations were made on the night of 2007 February 19. We performed 10-s exposures at four wave-plate angles (in the sequence 0° , 45° , 22.5° , and 67.5°) at 10 dithered positions for each set. The same observation sets were repeated 10 times toward the target object and for the sky background to increase the signal-to-noise ratio. The total integration time was 1000 s per wave plate angle. The typical seeing size during the observations was ~ 1.3 (2.9 pixels) in the J band. SIRPOL has been

routinely used since 2006 and the instrumental polarization is negligible (Kandori et al. 2006). The polarization efficiencies are 95.5 %, 96.3 %, and 98.5 % in the J , H , and K_s bands, respectively.

The data were processed using IRAF in the standard manner, which included dark-field subtraction, flat-field correction, median sky subtraction, and frame registration. The remaining artificial stripe pattern was then removed using IDL. The pixel coordinates of point-like sources found on the reduced images were matched with the celestial coordinates of their counterparts in the Two Micron All Sky Survey (2MASS) point source catalog. The IRAF IMCOORDS package was applied to the matched list to obtain plate transform parameters. The rms uncertainty in the coordinate transformation was ~ 0.1 .

Figure 1 shows the J - H - K_s color composite intensity image of the 8.0×8.0 region around NGC 2264 IRS 2 (hereafter the IRS 2 field) including IRAS 12 S1 core. The field is larger than the field-of-view of the camera because of dithering.

Mid-IR data obtained from Spitzer IRAC and MIPS were used for data analysis as well as our near-IR data. The IRAC $5.8 \mu\text{m}$ data were acquired in two epochs 7 months apart (2004 March 6 and October 8), with two dithers at each epoch to allow easy removal of asteroids and other transients, as part of Spitzer Guaranteed Time Observation program 37. Basic data reduction and calibration were done with the Spitzer Science Center (SSC) pipeline, version S14.0. The MIPS $24 \mu\text{m}$ data were obtained on 2004 March 16 using the scan-map mode, as part of Spitzer Guaranteed Time Observation program 58, and the data were reduced using the MIPS Data Analysis Tool, version S9.5. Since the spatial resolution of the MIPS $24 \mu\text{m}$ data is low, we paid considerable attention to finding the appropriate IRAC $5.8 \mu\text{m}$ and SIRPOL counterparts.

Figure 2 shows the J - H - K_s - $5.8 \mu\text{m}$ - $24 \mu\text{m}$ color composite intensity image of the IRS 2 region. Since protostars have significant circumstellar disks and envelopes, the $24 \mu\text{m}$ band may be particularly useful for identifying the Class I and Class 0 objects.

In this paper, we designate individual infrared reflection nebula(e) as IRN(e) and clusters of those infrared reflection nebulae as IRNC(s). We also designate the IRN associated with an IR source X as IRN (X) such as IRN (AR 6), IRN (IRS 2), and IRN (D-MM15), rather than numbering each.

3. RESULTS

3.1. Polarimetry of extended sources

Polarimetry of extended sources was carried out on the combined intensity images for each exposure cycle (a set of exposures at four wave plate angles at the same dithered position). The Stokes parameters I , Q , and U were calculated by

$$I = \frac{1}{2}(I_0 + I_{22.5} + I_{45} + I_{67.5}), \quad (1)$$

$$Q = I_0 - I_{45}, \quad (2)$$

and

$$U = I_{22.5} - I_{67.5}, \quad (3)$$

where I_a is the intensity with the half wave plate oriented at a° . The polarization degree P and the polarization position angle θ were calculated by

$$P = \frac{\sqrt{Q^2 + U^2}}{I} \quad (4)$$

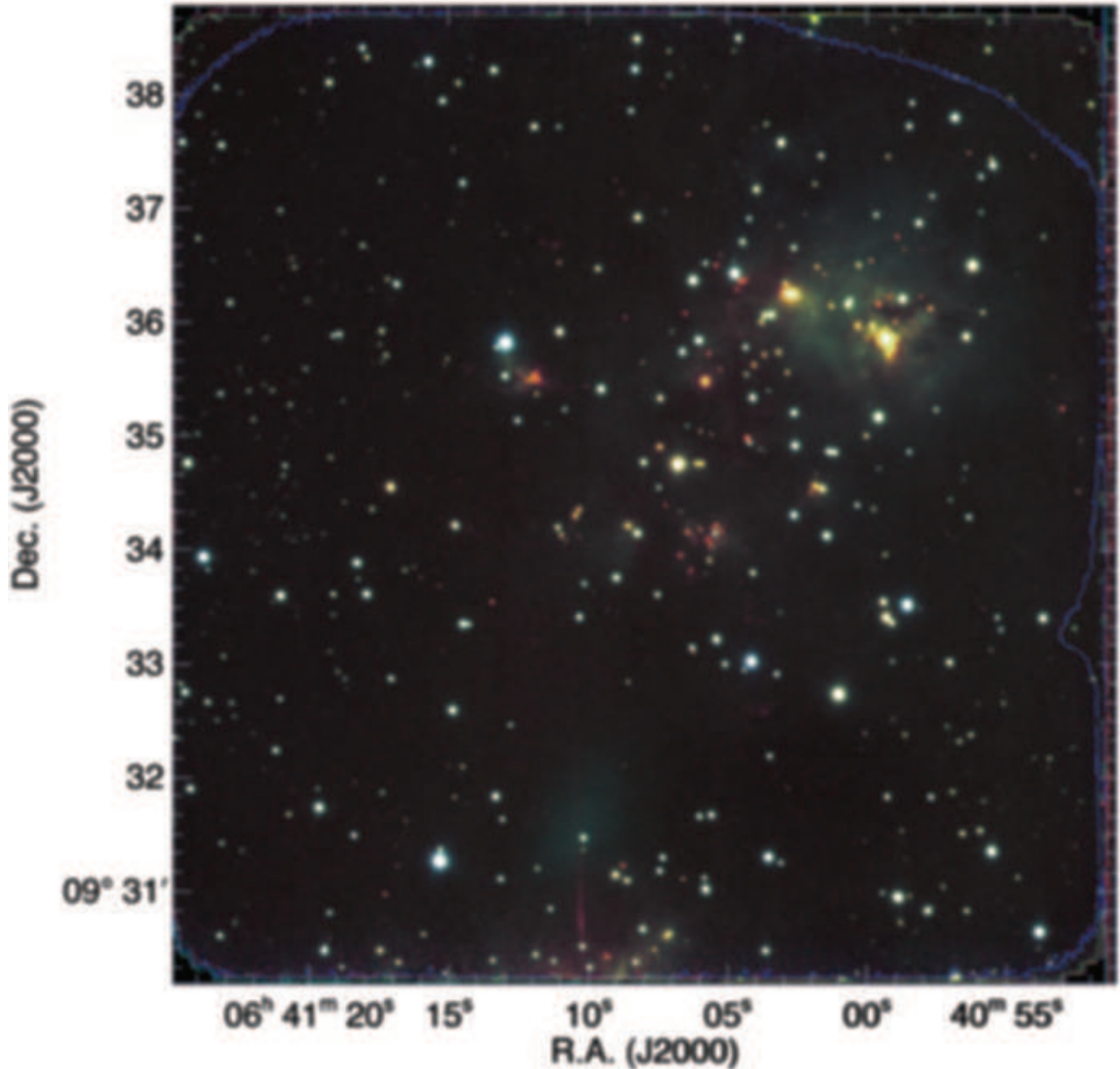


Fig. 1.— Color composite Stokes I image of the IRS 2 region in the J (blue), H (green), and K_s (red) bands from the IRSF/SIRPOL observations. The thin lines of red, green, and blue around the perimeter are boundaries of Stokes I images associated with each band. Note that there are bad pixel clusters around the upper-left and upper-right corners and the middle of the right boundary. See Figure 2 for identification of selected sources.

and

$$\theta = \frac{1}{2} \arctan \frac{U}{Q}. \quad (5)$$

The degree of polarization P was corrected using the polarization efficiencies of SIRPOL.

Figure 3 shows the H polarization vector map of the whole IRS 2 region superposed on the intensity I image combined with SIRPOL+Spitzer image data. This figure shows prominent and extended polarization nebulosities over the IRS 2 region for the first time. The polarimetry of extended sources can reveal the locations of illuminating sources within nebulae because the observed polarization is perpendicular to ray from illuminating source to scatterer.

3.2. Polarimetry of point-like sources

3.2.1. Photometry

The IRAF DAOPHOT package was used for source detection (Stetson 1987). The DAOPHOT program automatically detected point-like sources with peak intensities greater than 10σ above the local sky background, where σ is the rms uncertainty. The automatic detection procedure misidentified some spurious sources, which were removed by careful visual inspection, and missed a few real sources such as AR 6B. We included AR 6B because we were interested in AR 6B (see Section 4.1.1). Then the IDL photometry package adapted from DAOPHOT was used to perform aperture photometry. The aperture radius

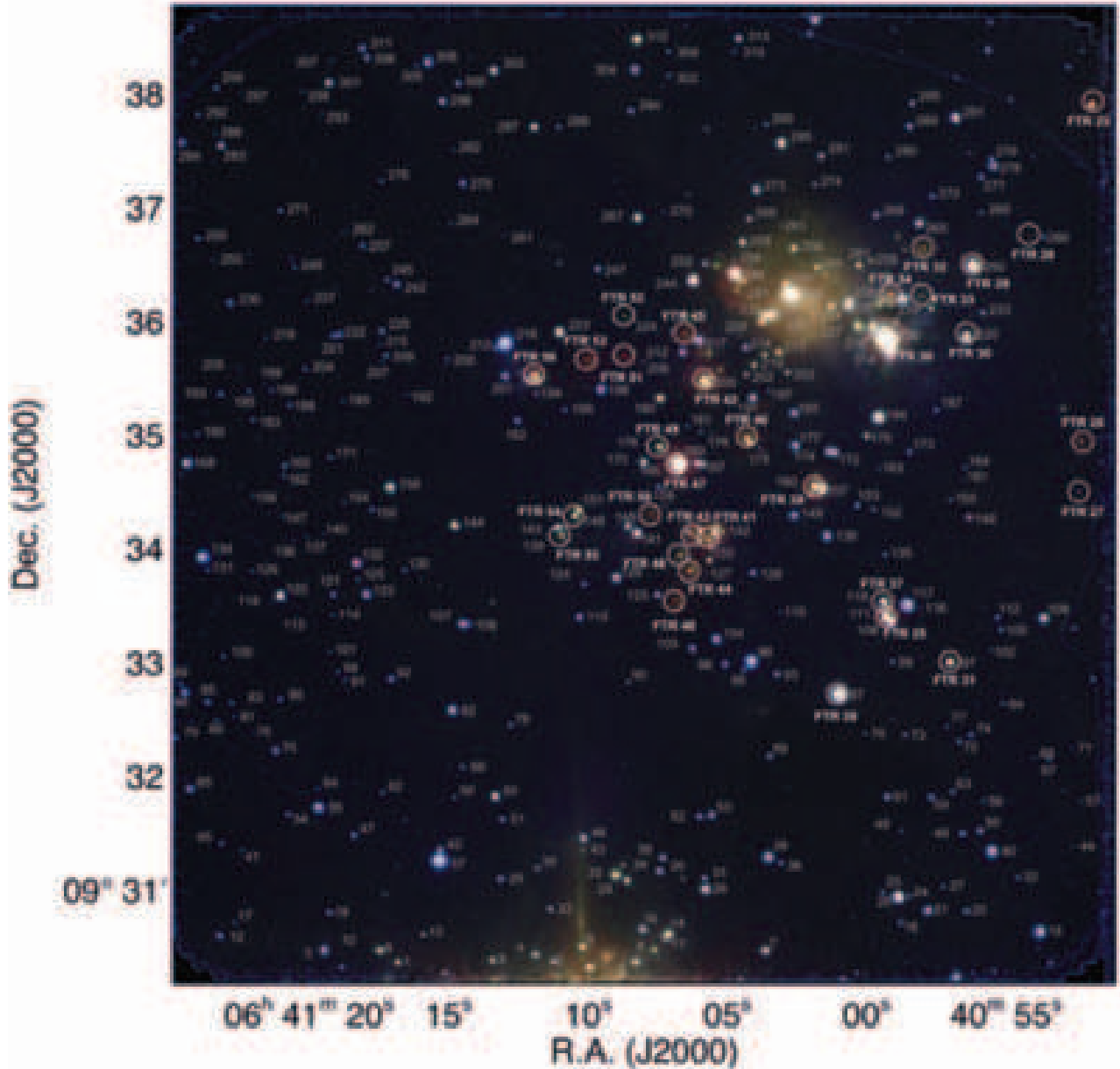


Fig. 2.— Finding chart of the IRS 2 field on the color composite image in the IRSF/SIRPOL JHK_s (blue), Spitzer/IRAC $5.8 \mu\text{m}$ (green), and Spitzer/MIPS $24 \mu\text{m}$ (red) bands. Detected point-like sources are labeled (Table 1). $24 \mu\text{m}$ sources from Forbrich et al. (2010) are denoted by both white circles and labels.

was 3 pixels and the sky annulus radius was set to 10 pixels with a 5-pixel width. The pixel coordinates of the detected sources were matched with the celestial coordinates of their counterparts in the 2MASS point source catalog.

The Stokes I intensity of each point-like source was calculated using equation (1). The magnitude and color of the photometry were transformed into the 2MASS system by

$$\text{MAG}_{2\text{MASS}} = \text{MAG}_{\text{IRSF}} + \alpha_1 \times \text{COLOR}_{\text{IRSF}} + \beta_1 \quad (6)$$

and

$$\text{COLOR}_{2\text{MASS}} = \alpha_2 \times \text{COLOR}_{\text{IRSF}} + \beta_2, \quad (7)$$

where MAG_{IRSF} is the instrumental magnitude from the IRSF images and $\text{MAG}_{2\text{MASS}}$ is the magnitude from the 2MASS

Point Source Catalog. The parameters were determined by fitting the data using a robust least absolute deviation method, and the mean absolute deviation for each data are 0.11393877, 0.072393811, and 0.084156421 for J , H , and K_s , respectively. For the magnitudes, $\alpha_1 = 0.0484596$, -0.0307835 , and $8.31423\text{e}-05$, and $\beta_1 = -4.75512$, -4.50592 , and -5.22532 for J , H , and K_s , respectively. For the colors, $\alpha_2 = 1.066$ and 0.989 and $\beta_2 = -0.283$ and 0.732 for $J-H$ and $H-K_s$, respectively. The coefficients β_1 and β_2 include both the zero-point correction and aperture correction. The derived magnitudes are listed in Table 1. The 10σ limiting magnitudes were 19.2, 18.8, and 16.8 for J , H , and K_s , respectively.

The resulting list contains 314 sources whose photometric uncertainties are less than 0.1 mag in all three bands (Table 1).

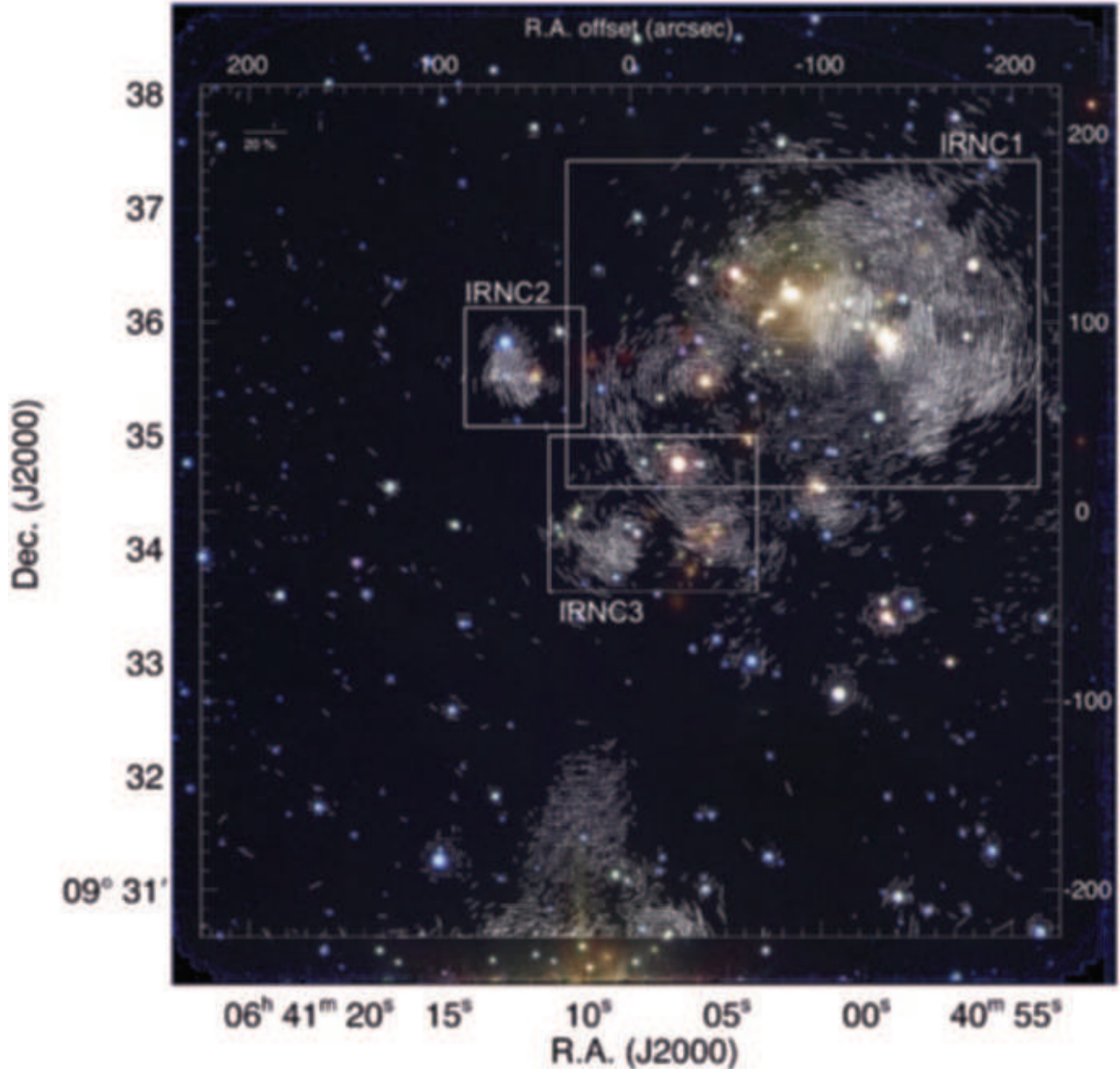


Fig. 3.— H polarization vector map superposed on the color composite image in the IRSF/SIRPOL JHK_s (blue), Spitzer/IRAC $5.8 \mu\text{m}$ (green), and Spitzer/MIPS $24 \mu\text{m}$ (red) bands. The length of the vectors is proportional to the degree of polarization. Shown in the upper left corner is a 20% vector. The vectors were made by 6×6 pixel smoothing (twice the seeing size), and the vectors were shown every 6 pixels with intensities greater than 3σ above the mean sky level, where σ is the standard deviation of sky brightness. Three IRNCs are labeled.

3.2.2. Aperture Polarimetry

Polarimetry of point-like sources (hereafter aperture polarimetry) was carried out on the combined intensity images for each wave plate angle at 10 dithered positions for each set, instead of using the Stokes Q and U images. This is because the center of the sources cannot be determined satisfactorily in the Q and U images. From the aperture photometry for each wave plate angle image, the Stokes parameters of each point-like source were derived by equations (2) and (3). The aperture and sky radii were the same as those used in the aperture photometry of the I images. The degree of polarization P and the

polarization position angle θ can be calculated by

$$P_0 = \frac{\sqrt{Q^2 + U^2}}{I}, \quad (8)$$

$$P = \sqrt{P_0^2 - \delta P^2}, \quad (9)$$

and

$$\theta = \frac{1}{2} \arctan \frac{U}{Q}, \quad (10)$$

where δP is the uncertainty in P_0 . Equation (9) is necessary to de-bias the polarization degree (Wardle & Kronberg 1974). The

degree of polarization P was corrected using the polarization efficiencies of SIRPOL.

Table 2 shows the derived source parameters. The uncertainties given in Table 2 (and elsewhere in this paper) are 1σ values. The aperture polarimetry can indicate the structure of magnetic fields by measuring dichroic polarization of background stars which is produced by aligned interstellar dust grains.

4. DISCUSSION

4.1. Scattered Radiation Field in the NGC 2264 IRS 2 Region

There are at least three IRNCs as well as several local IRNe in the outer parts of three IRNCs in Figure 3, characterized by both a high degree of polarization and a centrosymmetric pattern of polarization vectors, albeit often only partial, around an illuminating source whose location can often be identified. Some IRNe overlap with ill-defined boundaries. The polarization vector patterns around illuminating sources are often complex, and rarely entirely centrosymmetric. For example, illuminating sources may be close together, circumstellar disks and envelopes can involve multiple scattering and dichroic extinction, and foreground dust in the molecular cloud can also produce dichroic polarization. That significant regions of centrosymmetric patterns are observed implies that the amount of foreground dichroic extinction is relatively small, and/or patchy. In Figure 3, it is clear that each of the protostar cluster members indicated by $24\ \mu\text{m}$ sources (FTR sources), is associated with their own local nebulosity, indicating that each protostar is self-luminous and associated with the circumstellar matter such as envelopes or disks. We discuss the illuminating sources of IRNe in each IRNC in the following subsections.

4.1.1. IRNC 1

Figure 4 shows a close-up of the H polarization vector map of IRNC 1 shown in Figure 3. It is clear that the IRNC 1 region is dominated by various highly polarized local IRNe with illuminating sources, while the outer parts are roughly centrosymmetric around the central stellar sources (Figure 4).

The main illuminating source showing a large, centrosymmetric nebulosity extending to the south-west (more than $1'$) and also probably to the north-east (up to the middle point between AR 6 and IRS 2) is most likely to be AR 6. AR 6 consists of three stellar components, the brightest star AR 6A, the southern source 6B, and the faintest companion 6C. Unfortunately, our data could not resolve AR 6C because the distance between AR 6A and AR 6C is only $0''.84$, smaller than our seeing size. AR 6A+6C and AR 6B correspond to our source 218 and 314, respectively. The polarization of source 218 is 5–7% at $\sim 74^\circ$, and the polarization of source 314 is 2–5% at 42° – 74° .

The large IRN clearly shows a centrosymmetric pattern, indicating that the nebulosity is most likely associated with the central source AR 6. Therefore, we call it IRN (AR 6). This nebula corresponds to the blue region surrounding AR 6 in Figure 1, suggesting the central source is “evolved”. It is consistent with the illuminating source AR 6 being a visible YSO.

As shown in Figure 5, an enlargement of IRN (AR 6), AR 6 itself shows a compact ($\sim 20'' \times 10''$) cometary nebulosity, extending from the west of the stars and curving around them to the south (Aspin & Reipurth 2003). To the east of AR 6, polarizations are partly offset and not always centrosymmetric around AR 6 but are directing south-east of AR 6. There may be a polarization disk (Bastien & M enard 1988, 1990; Tamura et al. 1991) around AR 6. However, it is rare that a polarization disk

is observed around a visible YSO because the polarization disk is believed to be caused by multiple scattering in the dense disk. Aspin & Reipurth (2003) suggested that AR 6A is a young star within the NGC 2264, as an FUor-like pre-main-sequence object, and all of the nebulosity seen may be connected to AR 6A. AR 6B is also in an elevated FUor state as an FUor-like object, but it does not appear intimately associated with the nebulosity.

IRS 2 also belongs to the infrared reflection nebula cluster IRNC 1. It shows a generally centrosymmetric pattern, even though there are slight changes in the vector pattern at several parts of the nebula. The IRN (IRS 2) is approximately centrosymmetric out to $\sim 30''$, except for around point-sources in Figure 4. In the outer part of up to $1.5'$ to the north-west, the nebula also seems to be illuminated by IRS 2 rather than AR 6. Note that near the middle point between IRS 2 and AR 6, the polarization pattern is a mixture of the two polarization patterns.

IRS 2 is resolved into two sources in our images (RNO-E and RNO-W; Castelaz & Grasdalen 1988). RNO-E and RNO-W correspond to our sources 241 and 240, respectively (see Table 1). It is noteworthy that the polarization pattern very close to these sources (a few arcsec) is not centrosymmetric but rather aligned in IRN (IRS 2); this can trace the magnetic fields rather than the local nebula.

There are other notable reflection nebulae and their illuminating sources in this field besides those associated with AR 6 and IRS 2 as described below.

The most interesting feature of Figure 4 is the small nebula, IRN (D-MM15), associated with a faint source or a cluster of faint sources $\sim 30''$ to the east of IRS 2. This does not follow the centrosymmetric pattern around IRS 2 or the nearest source 246, suggesting that this faint source is an independent self-luminous source. This source is not point-like and is only visible in the K_s band. It appears that this source corresponds to a millimeter/submillimeter source D-MM15 of Peretto et al. (2006). The position of D-MM15 is $\alpha = 06^h 41^m 04^s.6$, $\delta = +09^\circ 36' 19''$ [J2000.0]. Hashimoto et al. (2008) proposed an evolutionary sequence of massive YSOs based on the morphology of the associated IRNe. The Type A IRNe defined by Hashimoto et al. (2008) have a non-point-like morphology and extend in a direction relatively perpendicular to the polarization vectors, and is similar to IRN (D-MM15) as shown in Figure 4. They suggested that the monopolar or bipolar IRN of aligned vectors corresponds to the earlier phase because multiple scattering is dominant in the circumstellar matter around the youngest YSOs.

Source 200 is within the red nebula around IRS 2, and the vector pattern is partly centrosymmetric in the outer part of source 200. However, the vectors in the inner part are well aligned in one direction that is associated with the magnetic field direction in the IRS 2 region. It is highly polarized ($P = 4$ – 9%) in all three bands (Table 2).

Source 169 shows similar vector patterns to source 200. The vector pattern is partly centrosymmetric in the outer part of source 169, and it is also highly polarized ($P = 5$ – 10%) in all three bands (Table 2).

4.1.2. IRNC 2

A faint red nebula around FTR 51 and FTR 53 (sources 51 and 53 of FTR) extends to the east of source 200 in Figure 4. The vector pattern of this nebula is not centrosymmetric around source 198, suggesting that the scattered radiation field here is dominated by the sources in IRNC 1. However, there is another IR cluster to the east whose nebulae are distinct from IRNC 1.

Figure 6 shows the polarization vector maps around FTR 56,

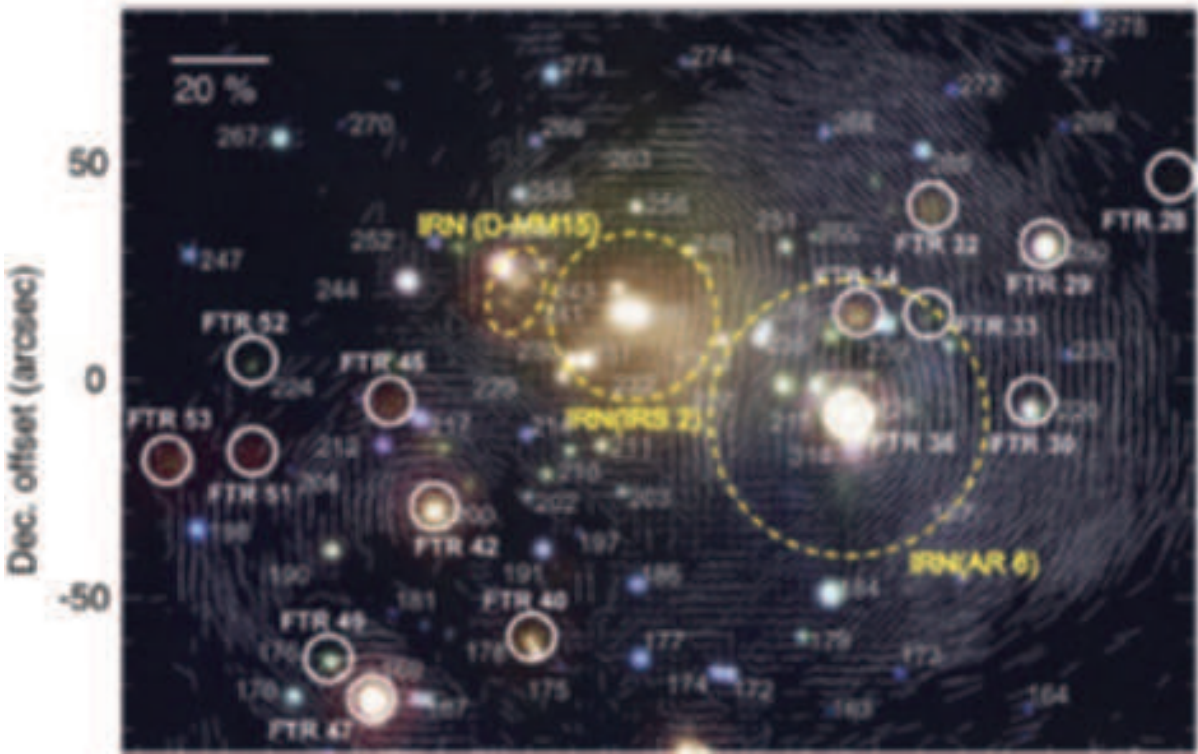


Fig. 4.— H polarization vector map of IRNC 1 superposed on the color composite image in the IRSF/SIRPOL JHK_s (blue), Spitzer/IRAC $5.8 \mu\text{m}$ (green), and Spitzer/MIPS $24 \mu\text{m}$ (red) bands. The length of the vectors is proportional to the degree of polarization. Shown in the upper left corner is a 20% vector. The vectors were made by 6×6 pixel smoothing (twice the seeing size). Detected point-like sources are labeled (Table 1). $24 \mu\text{m}$ sources from Forbrich et al. (2010) are denoted by both white circles and labels. Note that the size of yellow circles that indicate the position of IRNe does not mean the size of IRNe.

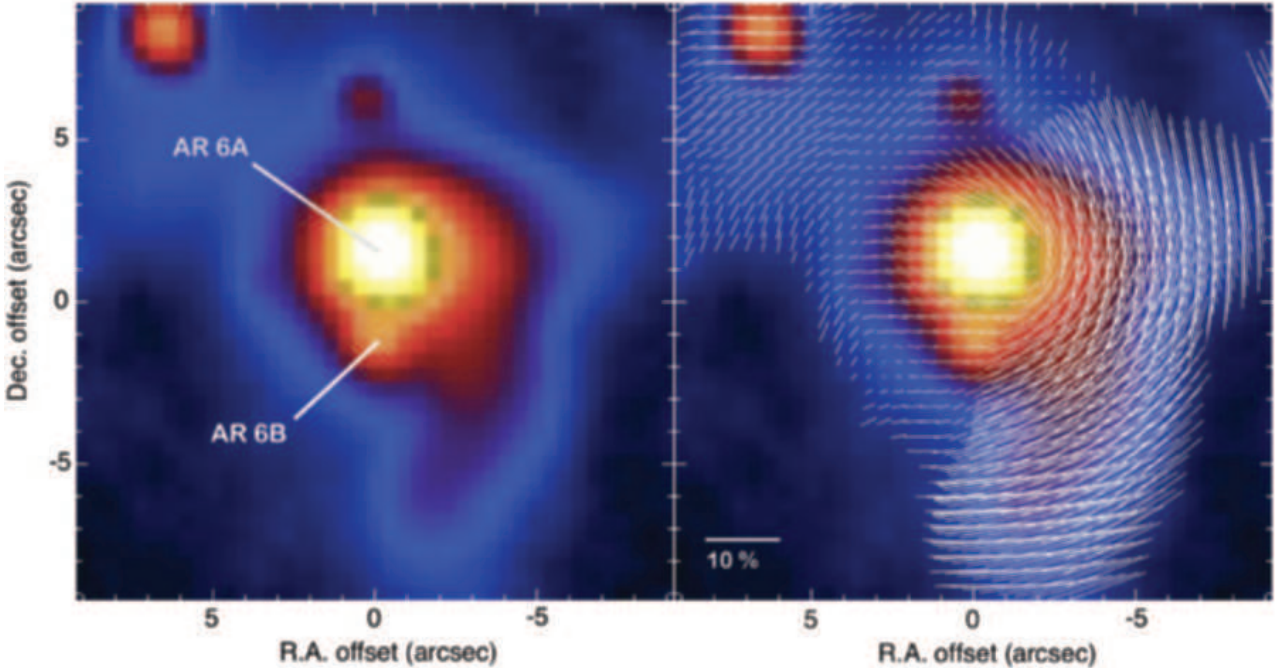


Fig. 5.— (left panel) Stokes I image of IRN (AR 6) in the H band. AR 6A and AR 6B are labeled. (right panel) H polarization vector map of IRN (AR 6). Shown in the bottom left corner is a 10% vector. The vectors were made by 3×3 pixel smoothing (the seeing size).

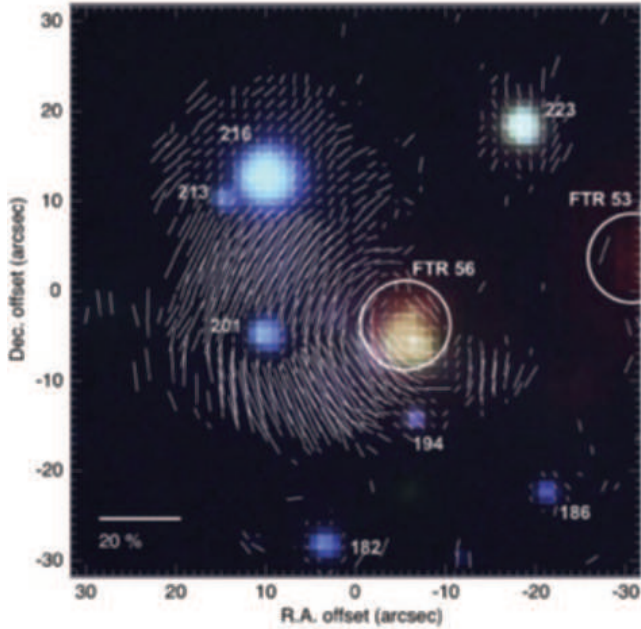


Fig. 6.— Same as Figure 4 for IRNC 2.

as a close-up of the H polarization vector map of IRNC 2 shown in Figure 3. This source is very red and in fact not point-like. The polarization map shows that the source itself is a reflection nebula and it extends significantly to the east (up to $\sim 20''$) but is partly interrupted by the blue point source 201. A small ($\sim 10''$) reflection nebula extending to the west is also clearly recognized. There is an independent nebula around the north-east blue sources 216 and 213 but the polarization pattern is not centrosymmetric. The north-west source 223 is also associated with a nebula but again its polarization pattern is not simple. The bright $24\ \mu\text{m}$ sources FTR 51 and FTR 53 are totally invisible in the near-IR.

4.1.3. IRNC 3

Figure 7 shows a close-up of the H polarization vector map of IRNC 3 shown in Figure 3, including the IRAS 12 S1. As shown in Figure 7, the vector pattern around IRAS 12 S1 itself is not highly polarized ($\sim 10\%$ or less) compared with those in IRNC 1 and IRNC 2 ($\sim 10\%$ or more), but our data suggest a clear association of a medium-size reflection nebula with a centrosymmetric pattern around this “microcluster” of protostars (Teixeira et al. 2006; YTL). In the outer part (up to $\sim 20''$), the nebula is roughly centrosymmetric, in particular to the south, south-west, and north-west in the H band. There is a more simple, interesting pattern in the K_s band. However, the central part and the region to the north-east are very complex.

Figure 8 shows enlargements of the H and K_s polarization vector maps for the IRAS 12 S1, i.e., in the right lower quadrant of Figure 7. These vector maps show very complex vector patterns slightly different from each other because of the sources only detected in the K_s band, or the difference between the amount of foreground dichroic extinction by different wavelengths. It also indicates that there might be other hidden sources as well as infrared sources and submillimeter sources in Figure 8.

In the H polarization vector map, the positions of the sources detected in the K_s band with Baade/PANIC (YTL) are marked

with circles and their source numbers. YTL reported several knots of molecular hydrogen in this “microcluster”, for example, between YTL 47 and YTL 49 and between YTL 40 and YTL 37. They also showed that YTL 44, associated with molecular hydrogen emission, has a distinctly bipolar appearance with an opaque dust lane, most likely caused by a circumstellar disk. Of particular interest is YTL 44, which shows a monopolar IRN of aligned vectors (Type A; Hashimoto et al. 2008). In the K_s polarization vector map, the positions of the seven SMA continuum data using the Submillimeter Array whose synthesized beam had dimensions of $1''.4 \times 1''.3$ (Teixeira et al. 2007) are marked with plus signs on the basis of the source positions from their K_s band image ($0''.125\ \text{pixel}^{-1}$). Teixeira et al. (2007) reported that SMA 1 and SMA 3 have mid-IR counterparts and SMA 2, SMA 6, and SMA 7 are associated with diffuse mid-IR emission. SMA 4 and SMA 5 do not appear to have any near- and/or mid-IR emission, even though there is near- and mid-IR diffuse emission located between these sources. In Figure 8 (bottom panel), the position of the SMA sources are slightly shifted (by $\sim 1''$), which is within the positional errors of the submillimeter array. We found that the shifted position show a better correlation between the near-IR nebula and the submillimeter sources.

FTR 50 and FTR 44 was classified as “genuine protostars” based on detailed SEDs (FTR). FTR 41 and FTR 43 that are multiple sources in IRAS 12 S1 also clearly showed protostar SEDs (FTR). They all do not show a centrosymmetric pattern of polarization vectors in Figure 7.

4.1.4. Local IRNe

We found that several $24\ \mu\text{m}$ sources such as FTR 39, FTR 38, FTR 37, and FTR 35 are associated with a local IRNe outside of three IRNCs in the observed region. The vector patterns around these local IRNe except for FTR 39 were not highly polarized compared with those in three IRNCs. IRN (FTR 39) is considered as one of members of IRNC 1.

4.2. Multiple Magnetic Fields in the IRS 2 Region

Figures 9–11 show the polarization maps of point-like sources superposed on the Stokes I images. The aperture polarimetry of the 314 point-like sources resulted in the positive detection ($P/\delta P \geq 3$) of 181, 212, and 97 sources in the J , H , and K_s bands, respectively, and 241 sources in at least one of the three bands.

The relation between the polarimetric and spectral data may be useful in understanding the nature of the polarization. The degree of polarization appears to be correlated with near-IR colors (Figure 12). The empirical relation for the upper limit of interstellar polarization suggested by Jones (1989) is

$$P_{K,\text{max}} = \tanh \left\{ 1.5E(H - K) \frac{1 - \eta}{1 + \eta} \right\}, \quad (11)$$

where $\eta = 0.875$ and $E(H - K)$ is the reddening arising from extinction. As shown in Figure 12, most of the sources are within this limit. A few sources are above the P_{max} limit, but their uncertainties are large. The near-IR polarization-to-extinction efficiency of the point-like sources in the IRS 2 field is consistent with that caused by aligned dust grains in the dense interstellar medium. Therefore, the near-IR polarizations of these sources are most likely dominated by dichroic extinction from aligned dust grains by a magnetic field, and the intrinsic polarization, if any, does not significantly affect the observed

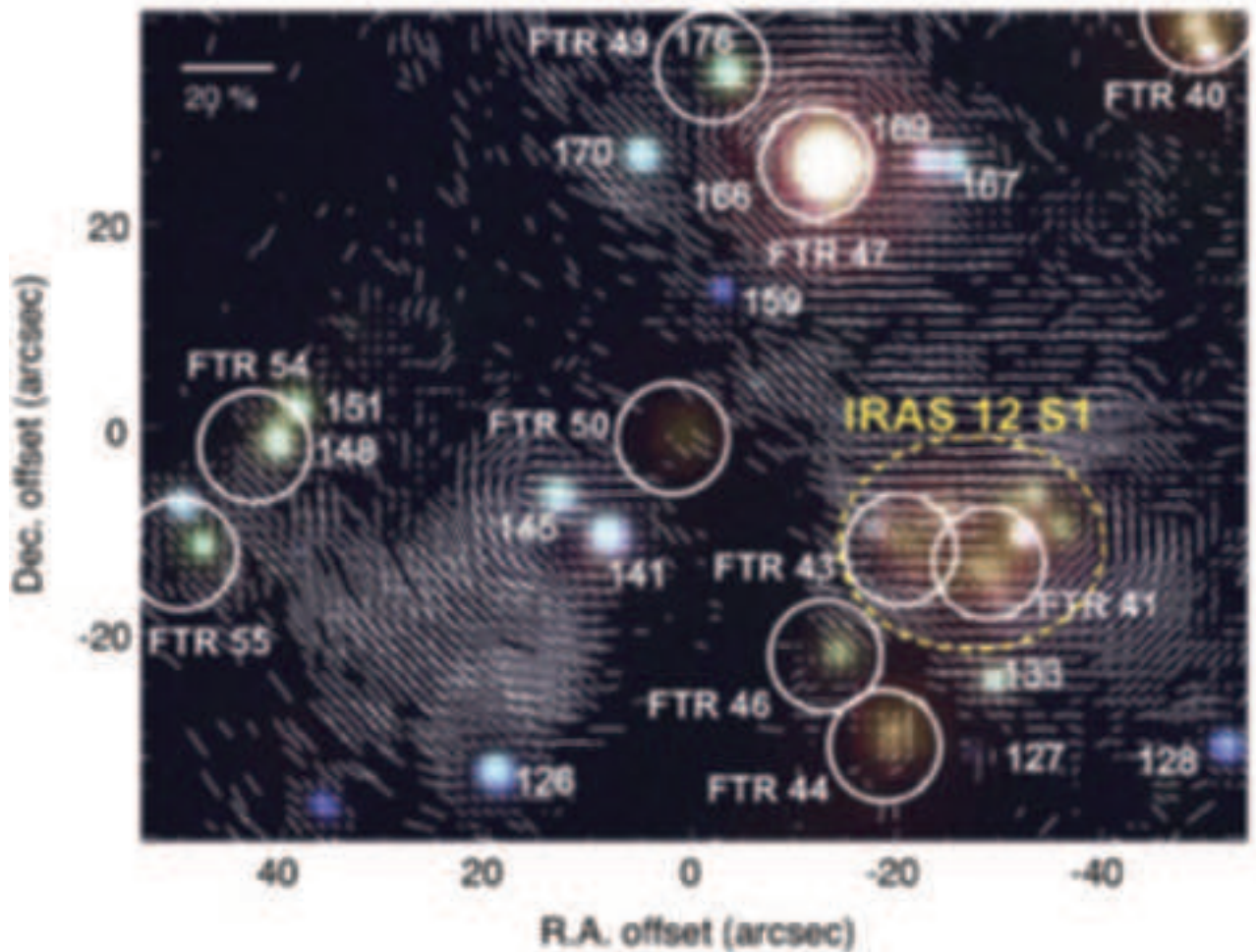


Fig. 7.— Same as Figure 4 for IRNC 3.

degree of polarization. However, this result does not completely exclude the possibility that some of the sources have intrinsic polarization because depolarization is also possible.

Aperture polarimetry in the K band using a $4''$ aperture is reported by Castelaz & Grasdalen (1988), for both RNO-E and RNO-W. The polarization degree of RNO-E was $3.3 \pm 0.3\%$ with a position angle of $30^\circ \pm 3^\circ$, and the polarization degree of RNO-W was $3.5 \pm 0.3\%$ with a position angle of $7^\circ \pm 3^\circ$. In our near-IR data, the polarization degree of RNO-E is 4–8% with a position angle of 91° – 98° with smaller errors. The polarization position angle of Castelaz & Grasdalen (1988) is somewhat smaller than our near-IR measurements. It is not clear what caused the difference in these sources.

4.2.1. Source Classification

The magnetic field structure of molecular clouds can be inferred from the polarization produced by dichroic extinction, provided sources are selected with no intrinsic polarization. YSOs in the cloud can exhibit a substantial degree of intrinsic polarization caused by circumstellar material. Such sources may show a large IR excess which can be identified from multiwavelength photometry.

Figure 13 shows a color–color diagram for all sources detected in all three bands. The diagram is divided into several

domains. Based on the location in this diagram, sources can be classified into a few groups (Lada & Adams 1992). The area near the locus of main-sequence/giant stars is called domain A0. Sources in domain A0 are either field stars (dwarfs and giants) or pre-main-sequence (PMS) stars with little IR excess (weak-lined T Tauri stars and some classical T Tauri stars) and with little reddening. There is a clear gap just above domain A0, and the area above this gap in the direction of the reddening vector is called domain Ar. Sources in domain Ar are either field stars or PMS stars with little IR excess and with substantial reddening. Domain B is the area next to domain Ar in the direction of higher $H - K_s$ (to the right) and above the locus of classical T Tauri stars. Sources in domain B are PMS stars with IR excess emission from disks. Domain C is the area next to and to the right of domain B. Sources in domain C are IR protostars or Class I sources. Herbig AeBe stars tend to occupy lower parts of domains B and C. This classification based on the color–color diagram, however, is far from perfect. A certain fraction of classical T Tauri stars may reside in domains A0 or Ar, some protostars can be found in domain B, and some extremely reddened AeBe stars may be found among protostars (Lada & Adams 1992). This “contamination” will eventually contribute to the uncertainty in statistical quantities derived from the classification, but the estimation of this uncertainty is beyond the scope

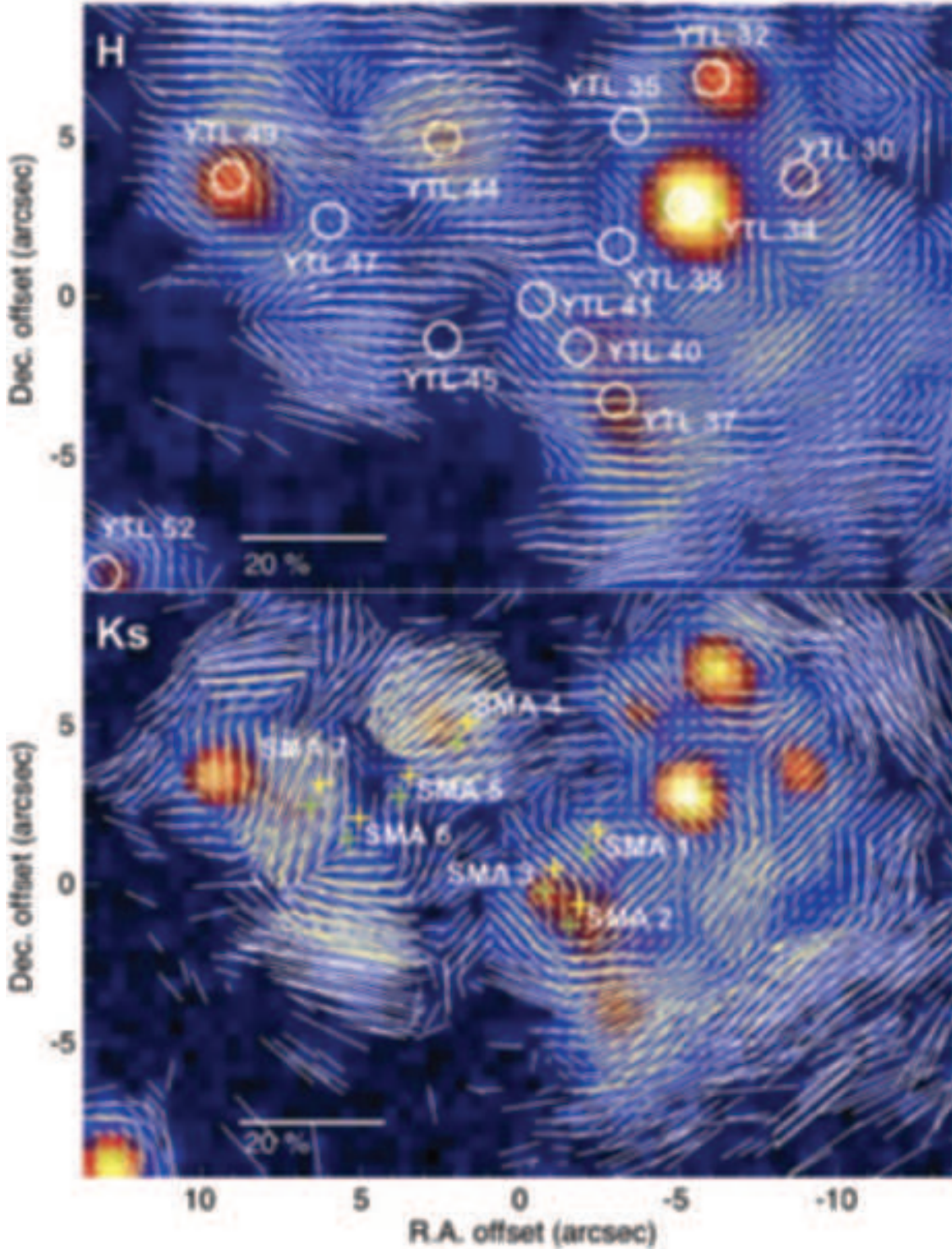


Fig. 8.— H and K_s polarization vector maps around the IRAS 12 S1 core of IRNC 3 superposed on each Stokes I image. The vectors were made by 3×3 pixel smoothing (the seeing size), and shown every 1 pixels with intensities greater than 3σ and 5σ above the mean sky level in the H and K_s bands, respectively. Additionally, the yellow vectors were drawn for greater than 6σ and 10σ in the H and K_s bands, respectively. (top panel) H polarization vector map. The circles mark the positions of the sources detected at the K band with Baade/PANIC with a stellar FWHM of $0''.37$ – $0''.44$ (Young et al. 2006). (bottom panel) K_s polarization vector map. The seven plus signs mark the positions of the SMA continuum data (Teixeira et al. 2007). Yellow plus signs: Original positions corresponding with Figure 1 of Teixeira et al. (2007). Green plus signs: Shifted positions to match their counterparts.

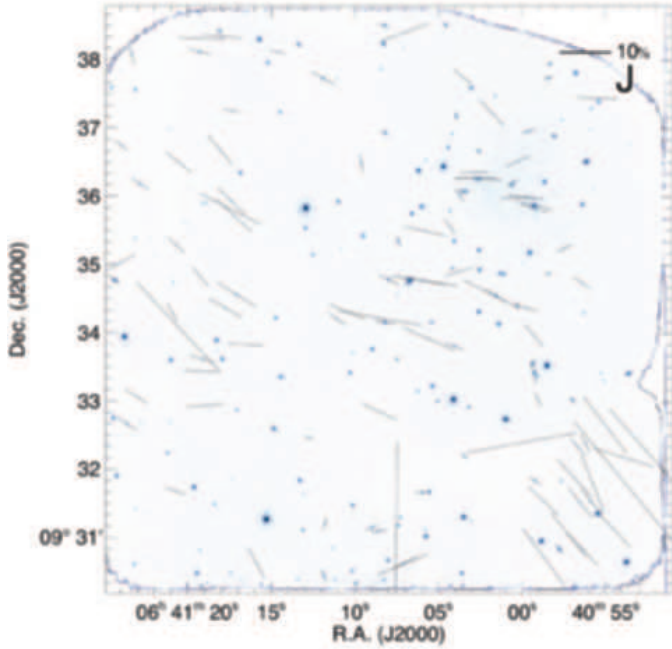


Fig. 9.— Stokes I image of the J band with polarization vectors for point-like sources having $P/\delta P \geq 3$. The length of the vectors is proportional to the degree of polarization. Shown in the upper right corner is a 10% vector. Note that there are bad pixel clusters around the upper-left and upper-right corners and the middle of the right boundary.

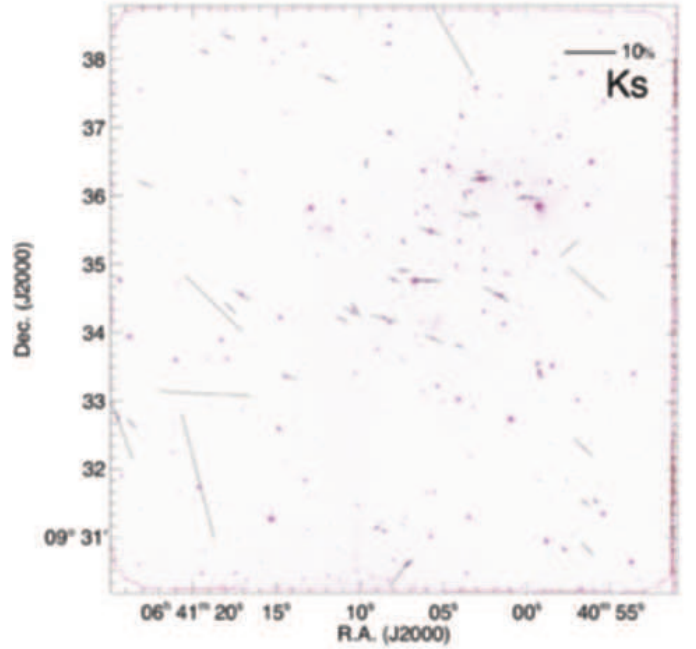


Fig. 11.— Same as Figure 9 for the K_s band.

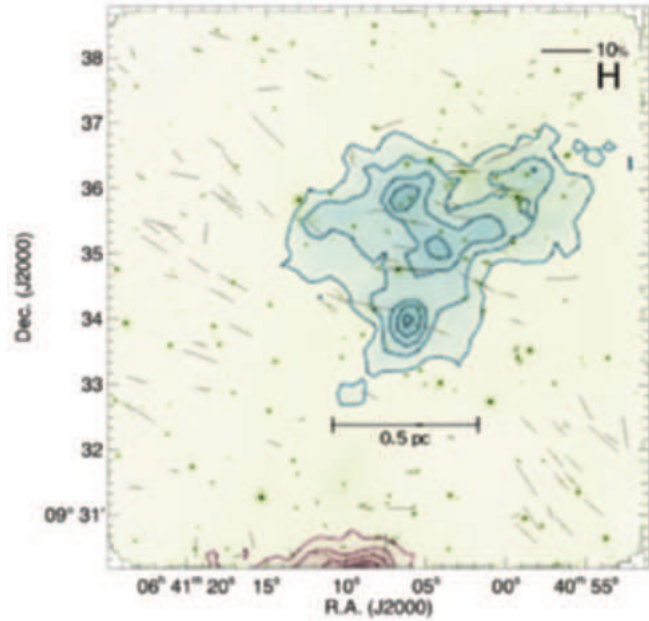


Fig. 10.— Same as Figure 9 for the H band with contours of $870 \mu\text{m}$ continuum emission (Williams & Garland 2002). Contours are at 0.5, 1.0, 1.5, 2.0, and 2.5 Jy beam^{-1} . Red contours: dense cluster of IRS 1 region. Blue contours: dense cluster of IRS 2 region.

of this paper.

There are 125 sources in domain A0, and they are collectively called group A0. They are either foreground stars or those seen along the line of sight with little extinction. One hundred fifty one sources were found in domain Ar. These sources (group Ar) are either background stars or PMS stars in the Monoceros OB1 cloud. They are the most useful sources for the study of the magnetic fields in the cloud (see Section 4.4 of Kwon et al. 2010).

Forty-five sources were found in domain B. These sources (group B) may be PMS stars associated with the Monoceros OB1 cloud.

Three sources (sources 255, 307, and 314) are located in domain C. AR 6B (source 314) is considered a variable star of FU Ori type (Aspin & Reipurth 2003).

4.2.2. Magnetic Field Strength

The sources in group Ar (Figure 13) are best for studying the magnetic fields in the molecular cloud because they are likely to have little intrinsic polarization, and the high reddening can lead to polarization through dichroic extinction that is selective attenuation of different components of the electric vector when light passes through a medium in which the grains are aligned by a magnetic field. Since there is significant difference between the vectors of the cluster core and outer parts in Figures 9–11, only the sources in the cluster core were chosen to estimate the magnetic field strength of the IRS 2 region, among group Ar sources. In Figure 10, contours of $870 \mu\text{m}$ continuum emission (Williams & Garland 2002) were superposed on the H polarization vector map. In the following discussion, we designate the sources within blue contours (dense cluster of IRS 2 region) as that of cluster core, and the sources outside blue and red contours as that of the perimeter of the cluster core. Note that the sources within red contours (dense cluster of IRS 1 region) are excluded from following discussions for magnetic fields.

Figure 14 shows the histogram for the H polarization posi-

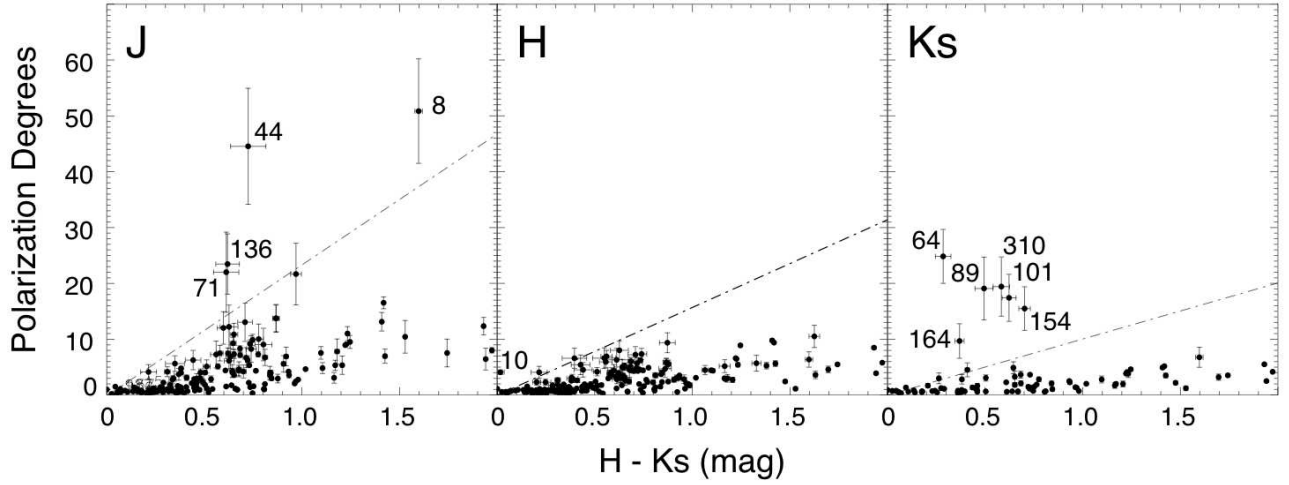


Fig. 12.— Degree of polarization vs. $H - K_s$ color. Several sources with large uncertainties are labeled (Table 2). Dot-dashed lines: empirical upper limits (P_{\max} ; Jones 1989).

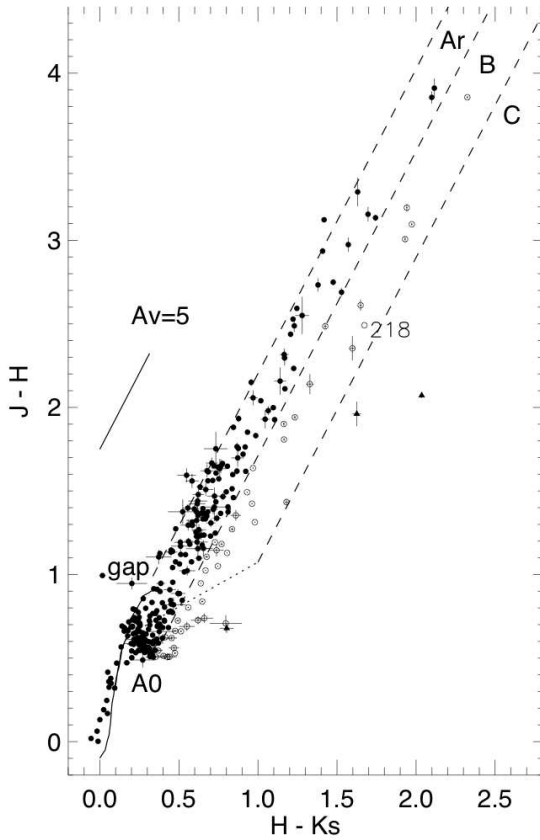


Fig. 13.— Color-color diagram of the point-like sources in the IRAS 12 S1 field. Filled circles: group A0 and Ar sources. Open circles: group B sources. Open triangles: group C sources. Solid curve: locus of main sequence and giant branch stars (Bessell & Brett 1988). Dotted line: locus of classical T Tauri stars (Meyer et al. 1997). Dashed lines: boundaries between domains A, B, and C (see Section 4.2.2). Solid line: reddening vector.

tion angles of the group Ar sources in both the cluster core and perimeter. The dispersion of the polarization position angles toward the IRAS 12 S1 core, covering a region of about a $4' \times$

$4'$, is larger than that of the point-like sources in the perimeter of the cluster core. For the point-like sources of the dense cluster, the mean angle is 81° with a standard deviation of 29° . For the sources in the perimeter of the cluster core, the mean angle is 58° with a standard deviation of 24° . The difference between the cluster core and the perimeter is 23° , which is smaller than the standard deviation of each of them. Note that there is a systematic gradient in the magnetic field orientation over the imaged field, even though there is relatively large dispersion of polarization angles in the cluster core.

Although the polarization measurement does not provide a direct estimate of the magnetic field strength at each data point in the image, a rough estimate over a large region is possible by statistically comparing the dispersion of the polarization orientation with the degree of turbulence in the cloud (Chandrasekhar & Fermi 1953). Assuming that velocity perturbations are isotropic, the strength of the magnetic field projected on the plane of the sky can be calculated by

$$B_p = Q \sqrt{4\pi\rho} \frac{\delta v_{\text{los}}}{\delta\theta}, \quad (12)$$

where Q is a factor to account for various averaging effects, ρ is the mean density of the cloud, δv_{los} is the rms line-of-sight velocity, and $\delta\theta$ is the dispersion of the polarization angles. Ostriker et al. (2001) suggested that $Q \sim 0.5$ is a good approximation when the angle dispersion is small ($\delta\theta \lesssim 25^\circ$) from numerical simulations, and Houde (2004) also suggested that a correction factor of ~ 0.5 is appropriate in most cases when the magnetic field is not too weak. Since the magnetic field seems to be ordered over the IRS 2 region, the magnetic field is expected to be strong and we adopt a correction factor of 0.5 to estimate the magnetic field strength, even though the angle dispersion (29°) in the cluster core is a little larger than the 25° suggested by Ostriker et al. (2001). From observations of cluster forming clumps in the N_2H^+ (1–0), Peretto et al. (2006) estimated a mean H_2 density of $6.0 \times 10^4 \text{ cm}^{-3}$ assuming a spherical volume and a mean clump diameter of 0.9 pc. They also estimated a 3D velocity dispersion of 1.4 km s^{-1} , assuming isotropic motion. Then, from equation (12), the strength of the magnetic field projected on the plane of the sky is derived to be $B_p \approx 100 \mu\text{G}$. The uncertainty in this estimate is rather large because the observed IRS 2 field is only a part of the Monoceros OB1 cloud and be-

4.2.3.1 Galactic vs. Local-cloud Magnetic Fields

Previous observations suggest that the local magnetic field associated with molecular clouds correlates with the Galactic magnetic field (Kobayashi et al. 1978; Dyck & Lonsdale 1979). This indicates that the Galactic magnetic field is likely to play an important role in the formation and evolution of molecular clouds. For example, Dyck & Lonsdale (1979) compared infrared aperture polarization for 31 protostellar sources buried in compact HII regions and molecular clouds with the interstellar polarization in the vicinity of the sources as determined from field stars. There was a strong tendency for the infrared and interstellar polarization vectors to be approximately parallel, with sixty-five percent of the sample (29 sources) having position angles of polarization lying within 30° of the average local interstellar polarization direction. NGC 2264 IRS 1 was one of the exceptions, with the infrared polarization vector closer to the orientation of the galactic plane than to the average interstellar polarization direction, but is not close to either. In the following, we compare near-infrared and optical polarization data to reveal the relationship between the local and Galactic magnetic fields in the IRS 2 region.

Interstellar polarizations in a ($20^\circ \times 20^\circ$) region centered around IRS 2, were taken from the optical polarization data in the Heiles catalogue (2000).¹ Figure 15 shows the relations between both polarization degrees and polarization angles against distances for the optical data. It shows larger polarization degrees at larger distances, as expected, as well as larger dispersion. For the position angles there is a peak in the angles beyond the distance of 760 pc in contrast to the sources in front of that. Figure 16 shows histograms of the polarization position angles for the local (our near-IR data) and Galactic magnetic field, and Figure 17 shows the interstellar polarization vector map of the Galactic magnetic field from optical polarization data. The direction of the Galactic magnetic field runs roughly perpendicular to the direction of the local magnetic field. In other words, the local magnetic field is not aligned with the Galactic magnetic field. Therefore, some other factors other than the Galactic magnetic field may have played a role in the formation and evolution of the cluster core in this region. It is interesting to note that the IRAS 12 S1 core may be rotating (Wolf-Chase & Walker 1995) and that the suggested axis of rotation in NGC 2264 coincides with the axis of the Galaxy (Dyck & Lonsdale 1979).

4.2.3.2 Comparisons with Theory of Cluster Formation

Very recently, Nakamura & Li (2010) performed numerical simulations of clustered star formation in parsec-scale dense clumps with different magnetic field strength and discussed the role of magnetic fields in cluster formation. The initial cloud was a centrally condensed spherical clump with a simulation box length of 2 pc. The central density was $5.0 \times 10^{-20} \text{ g cm}^{-3}$ ($1.5 \times 10^4 \text{ cm}^{-3}$), yielding a total clump mass of $884 M_\odot$. These physical quantities appear to be in a reasonable agreement with those of the observed IRS 2 field. They also assumed an isothermal equation of state with a sound speed of 0.23 km s^{-1} for a mean molecular weight of 2.33 and a gas temperature of 15 K. In addition, the magnetic field strength was specified by the plasma beta β , the ratio of thermal pressure to magnetic pressure at the clump center, through $B_0 = 25.8\beta^{-1/2}$

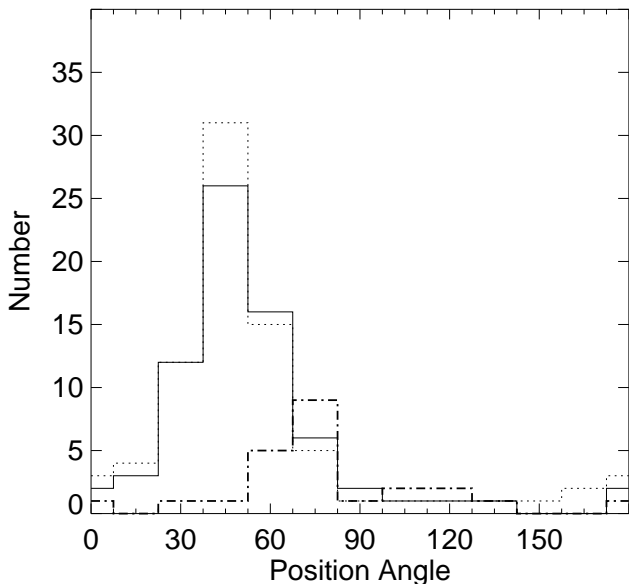


Fig. 14.— Histograms for the H polarization position angles of the group Ar sources in both the cluster core and perimeter. Note that 15° bin is used because the sample size is small. For the point-like sources of the cluster core, the mean angle is 81° and for the sources in the perimeter of the cluster core the mean angle is 58° . The mean angle is 60° . Dot-dashed line: histogram of polarization position angles for the group Ar sources having $P/\delta P \geq 3$ in the cluster core, from our near-IR data. Solid line: histogram of polarization position angles for the group Ar sources having $P/\delta P \geq 3$ in the perimeter of the cluster core, from our near-IR data. Note that for the point-like sources of the dense cluster the distribution is relatively widespread, but the sample size is too small to discuss in detail. Also shown is the histogram of polarization position angles at a wavelength of $350 \mu\text{m}$. The distribution of the polarization position angles at $350 \mu\text{m}$ is in better agreement with that of the H band in the perimeter of the cluster core than in the cluster core. Dotted line: histogram of polarization position angles of all the 77 sources in IRS 2 region obtained from $350\text{-}\mu\text{m}$ observations (Table 2 of Dotson et al. 2010) with the criterion $F > 3\sigma_F$, where F is the total unpolarized flux density.

cause the mean density ρ used in above equation is small due to imperfect coupling between ions and neutrals. It has been suggested that the gas densities are too low toward the edge of the CO outflow in the IRS 2 region (Wolf-Chase & Walker 1995). Thus, it should be taken as an order-of-magnitude estimate. The estimated magnetic field strength of the IRS 2 region is similar to that of other molecular clouds ($20\text{--}200 \mu\text{G}$) derived using the Chandrasekhar–Fermi method (e.g., Andersson & Potter 2005; Poidevin & Bastien 2006; Alves et al. 2008; Kwon et al. 2010; Sugitani et al. 2010).

¹An agglomeration of stellar polarization catalogs with results for 9286 stars

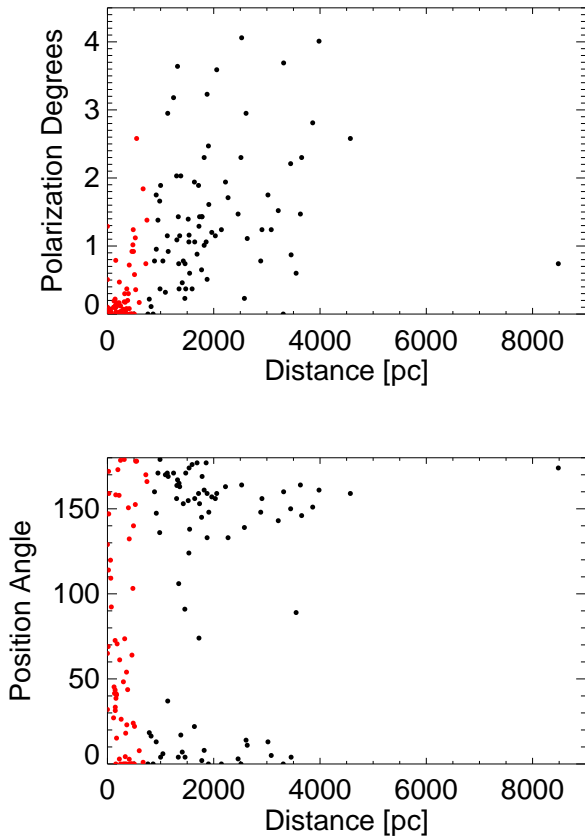


Fig. 15.— Polarization degrees (top panel) and polarization position angles (bottom panel) against the distance from the Heiles catalogue (2000). Red circles: sources on below a distance of 760 pc. Black circles: sources beyond a distance of 760 pc.

μG . In their numerical models it was found that the filamentary clumps are almost perpendicular to the global magnetic fields when the cluster forming clumps are created out of a strongly-magnetized cloud. In contrast, when the magnetic field associated with the parent molecular clouds is dynamically weak, the random component parallel to the filamentary clumps tends to be stronger preferentially in the dense parts when the turbulent flows play a role in the formation of the dense clumps. The observed, spatially ordered magnetic field seems consistent with their strongly-magnetized model for which the cloud dynamics is regulated by the strong magnetic field. Therefore, our comparison between local and global magnetic fields may indicate that the cluster forming clumps of the IRS 2 region including the protostars in the distribution corresponding to the Jeans length may be created out of such a cloud, in the presence of strong magnetic fields. However, even in a magnetically subcritical cloud, partly distorted field components exist. This could explain the difference in the polarization position angles between the cluster core and the perimeter.

4.2.4. Protostellar Outflows and Magnetic Fields

Most cloud cores are magnetically supercritical (Nakano 1998, 1999; Crutcher 1999; Shu et al. 1999), and outflows are closely related to the magnetic field in the cloud as well as the

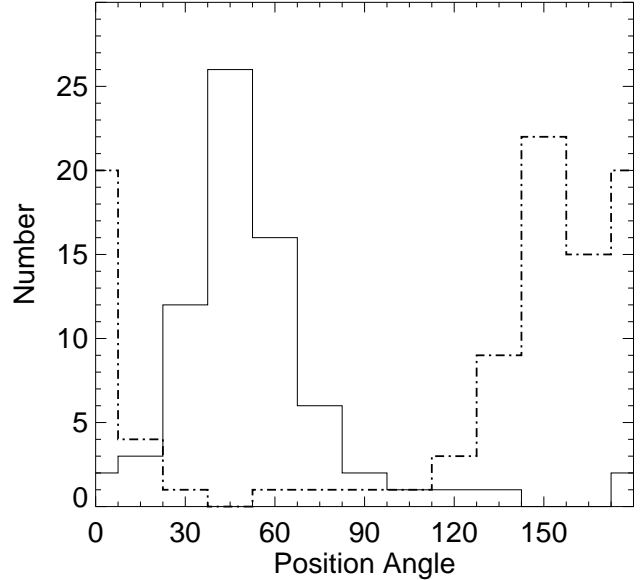


Fig. 16.— Histograms of polarization position angles. Dot-dashed line: polarization position angles of the sources from the Heiles catalogue (2000). Solid line: polarization position angles for the group Ar sources in the perimeter of the cluster core for the H band.

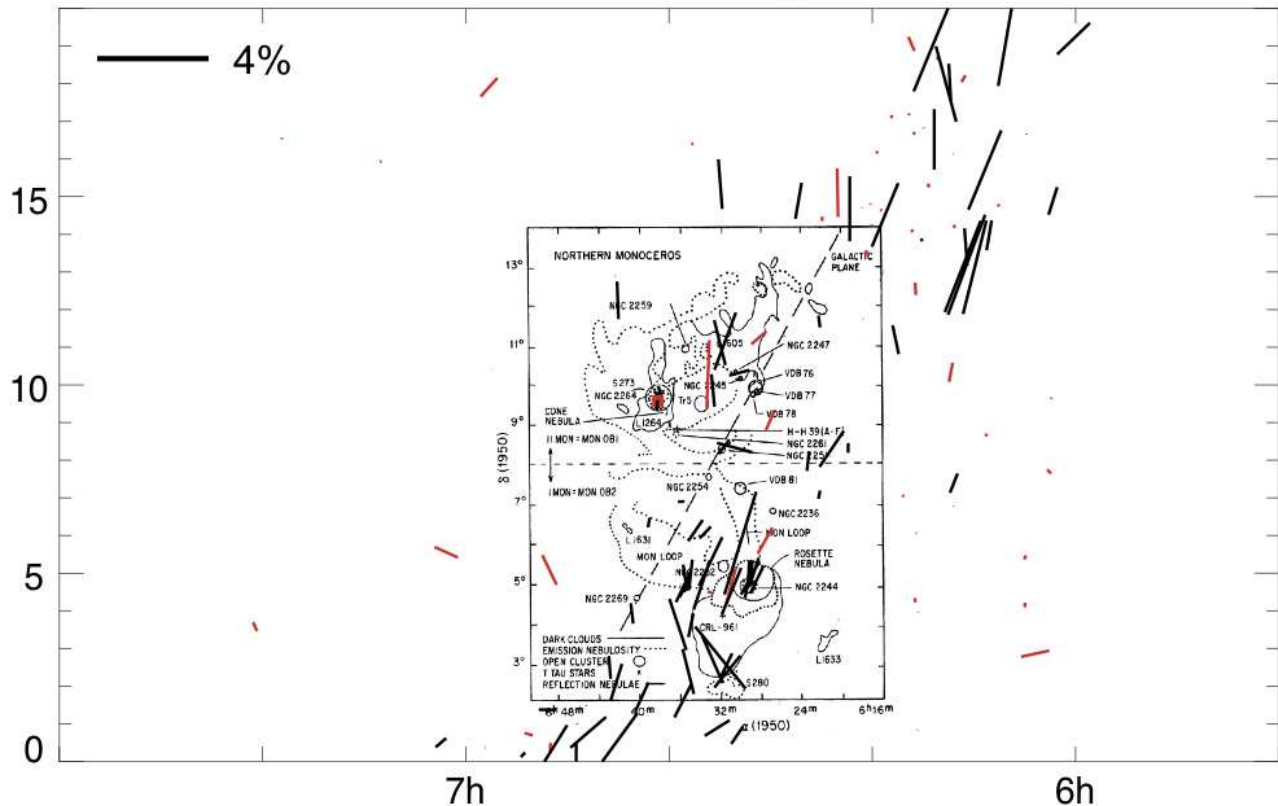
accretion process, angular momentum transportation.

Molecular outflows in the Monoceros OB1 cloud were reported previously by Margulis & Lada (1988). The direction ($\sim 60^\circ$) of the CO molecular outflow measured by connecting the peaks of the red- and blue-shifted components is well aligned with that of our observed local magnetic field in the IRS 2 region ($\sim 60^\circ$). Based on Wolf-Chase et al. (2003), if IRAS 12 S1, a multiple source, is the main contributor to this outflow, then the outflow momentum flux is roughly an order of magnitude greater than expected for a Class I object of comparable bolometric luminosity. It means that IRAS 12 S1 consists of young Class 0 objects (Bontemps et al. 1996).

Outflow formation has been simulated by many researchers, as has protostellar collapse (e.g., Tomisaka 1998, 2002; Machida et al. 2005a, 2005b, 2006; Matsumoto & Tomisaka 2004; Matsumoto et al. 2006; Ziegler 2005; Banerjee & Pudritz 2006; Fromang et al. 2006). According to these simulations, outflow axes tend to be aligned parallel to the local magnetic fields and perpendicular to rotating disks, when the magnetic fields associated with parent cloud cores are not weak. This implies that the magnetic field strength in the IRS 2 region may be strong enough to align the outflows in the direction of the local-scale magnetic field.

In addition, the NGC 2264 cluster contains stars at different stages of formation, and the star formation process appears to have continued for a few Myrs (Dahm & Simon 2005), corresponding to more than 10 free-fall times for a gas clump with a few 10^4 cm^{-3} . In other words, the star formation in NGC 2264 is likely to be relatively slow. Such slow star formation could be explained by protostellar outflow feedback that can impede the global gravitational collapse by regenerating super-

Heiles Catalog



Center: 06h 41m 05.9s 09d 34m 11.3s (J2000)

Fig. 17.— Comparison of the polarization vector map from the Heiles catalogue (2000) with the map of the Northern Monoceros region including NGC 2264 (Pérez 1991). The length of the vectors is proportional to the degree of polarization. Shown in the upper left corner is a 4% vector. The red box is associated with the IRS 2 region. Red lines: vectors for sources below a distance of 760 pc. Black lines: vectors for sources beyond a distance of 760 pc.

sonic turbulence. Recent numerical simulations have shown that the star formation rate is significantly reduced to an observed low level particularly in the presence of moderately-strong magnetic field. (e.g., Li & Nakamura 2006; Nakamura & Li 2007, 2010; Wang et al. 2010).

4.2.5. Comparison with Submillimeter Polarimetry

An interesting issue is how useful near-IR polarimetry is in tracing the magnetic field structure of dense clouds. Goodman et al. (1995) suggested that the polarizing power of dust grains may drop in the dense interior of some dark clouds and that near-IR polarization maps of background sources may be unreliable. However, the relevant physics is surprisingly complex (Lazarian 2007) and there are various pieces of observational evidence and theoretical explanations for aligned grains in dense cloud cores (Ward-Thompson et al. 2000; Cho & Lazarian 2005; Hough et al. 2008). To compare the magnetic field direction derived from dichroic polarization at near-IR wavelengths with that from thermal emission polarization at submillimeter wavelengths, it may be a worthwhile experiment to confirm the potential inefficiency of grain alignment in a dense region, even though previous observations have already shown agreement in the magnetic field structures at various wavelengths such as near-, far-IR, or submillimeter wave-

lengths (Tamura et al. 1996, 2007; Houde et al. 2004; Kandori et al. 2007). Figure 18 shows a comparison with submillimeter polarization vector map (Dotson et al. 2010), and Figure 14 shows histograms of polarization position angles at H and at a wavelength of $350 \mu\text{m}$ (Dotson et al. 2010). Interestingly, the distribution of the polarization position angles at $350 \mu\text{m}$ is in better agreement with that of the H band in the perimeter of the cluster core than in the cluster core. The mean angle of the polarization position angles at $350 \mu\text{m}$ is 60° .

The general trend derived from the above two wavelengths represents a good agreement with each other, although their spatial scale is somewhat different. Therefore, our results indicate that both near-IR dichroic polarization and submillimeter emission polarization may trace the magnetic field structures associated with the IRS 2 region.

4.2.6. Wavelength Dependence of Interstellar Polarization

Though the near-IR polarizations of selected point-like sources are most likely dominated by dichroic extinction with no nebulosity, we cannot rule out the possibility of the presence of unresolved reflection nebulae in some of the sources. To discriminate between the contributions from the dichroic extinction and from the scattering, the wavelength dependence of polarization can be measured by calculating the ratio of polar-

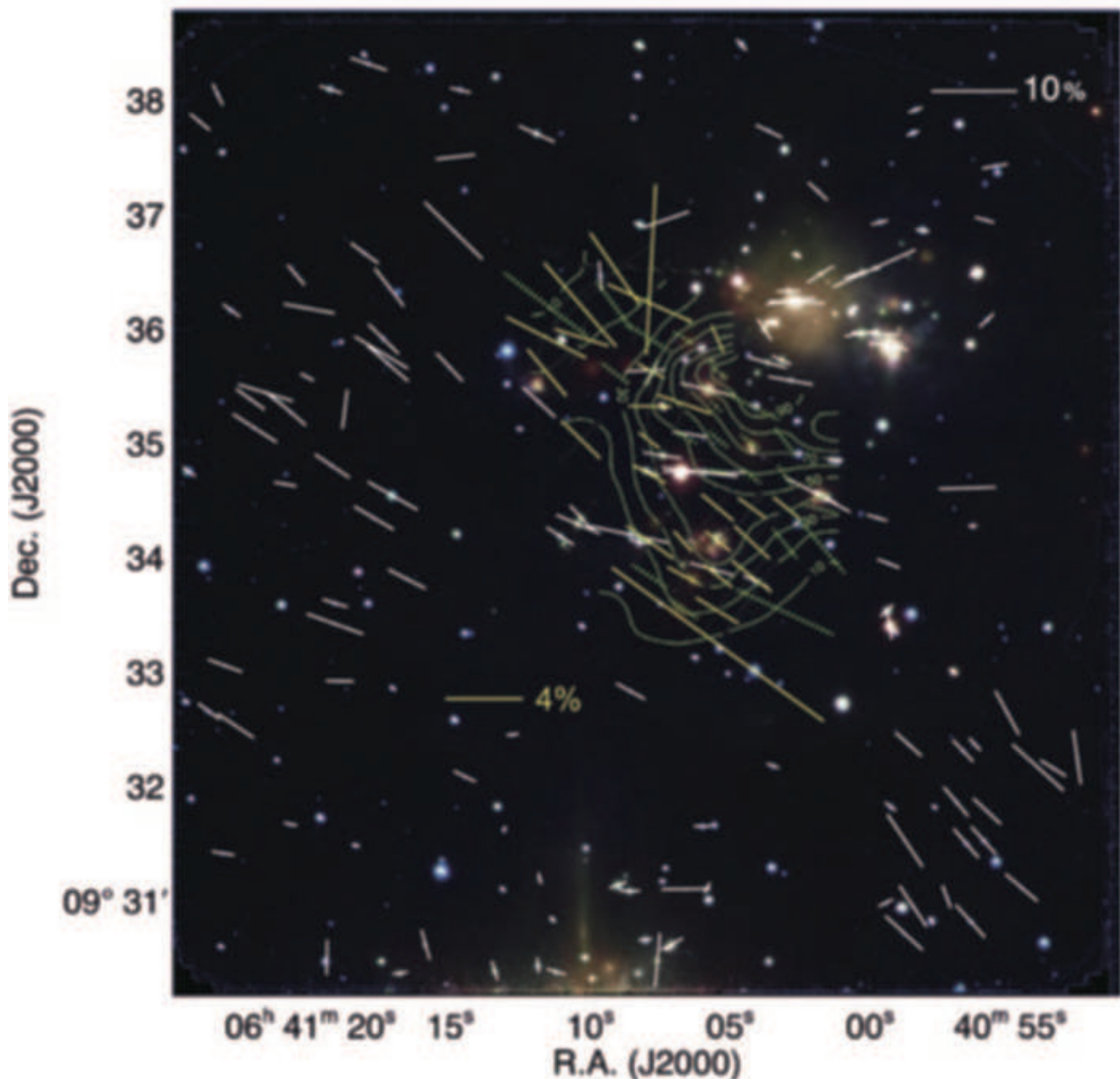


Fig. 18.— Submillimeter polarization vector map (Dotson et al. 2010) superposed on H polarization vector map. Note that the submillimeter polarization vectors were rotated by 90° to show the inferred magnetic field direction and directly to compare our near-IR polarization vectors. White vectors: H polarization vectors. Yellow vectors: submillimeter polarization vectors ($P/\sigma_p \geq 3$). Green dotted vectors: submillimeter polarization vectors ($2 \leq P/\sigma_p < 3$). Green contours: contours at 10%, 20%, ..., 90% of the peak intensity of 62 Jy beam^{-1} .

ization degrees. In the IR wavelength range, the polarization by dichroic extinction decreases with wavelength, while the polarization by scattering is not a strong function of wavelength (Whittet et al. 1992; Casali 1995). Figure 19 shows the P_J/P_{K_s} and P_H/P_{K_s} ratios for the sources in the IRS 2 region. It is very clear that group A0 and Ar show very different behavior. Within group Ar, the ratios are reasonably constant, and the weighted average values are $P_J/P_{K_s} = 2.22$ and $P_H/P_{K_s} = 1.54$ with standard deviations of 0.80 and 0.50, respectively. These values are consistent with the empirical relation $P \propto \lambda^{-\beta} = 1.6\text{--}2.0$

(Whittet 1992). Therefore, the polarization of group Ar sources can be very well explained by dichroic extinction. Source 11 shows an unusually high ratio in Figure 19 (top panel). The J polarization degree of source 11 is too high with large errors, while the P_H/P_{K_s} ratio is near 1 as expected. Since source 11 is located around boundary, it may be possible that it was caused by a bad pixel in the J band.

In contrast, the P_J/P_{K_s} and P_H/P_{K_s} ratios of group A0 sources are near unity, which is significantly different from those of group Ar sources. Therefore, the polarization mechanism for low extinction sources may be dominated by the cir-

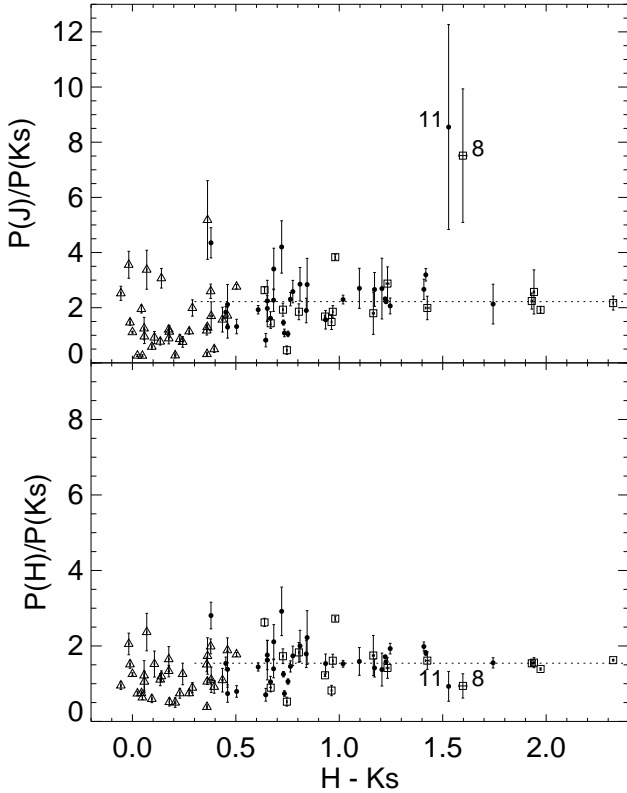


Fig. 19.— Ratio of J to K_s polarizations (top panel) and the ratio of H to K_s polarizations (bottom panel) against the $H - K_s$ color for the sources detected in the J , H , K_s bands (Table 2). Triangles: sources in group A0. Filled circles: sources in group Ar. Squares: sources in group B. Dotted lines: weighted average for group Ar.

cumstellar scattering (see more discussions in Section 5.4 of Casali 1995).

The P_J/P_{K_s} and P_H/P_{K_s} ratios of group B are similar to that of group Ar, and Source 8 also shows an unusually high ratio in Figure 19 (top panel). The J polarization degree is too high with large errors, while the P_H/P_{K_s} ratio is near 1 as expected. It is the same as source 11.

5. SUMMARY

We conducted deep and wide-field J - H - K_s imaging polarimetry in the direction of a $8' \times 8'$ region around NGC 2264 IRS 2 in the Monoceros OB1 cloud. The main results in this study are summarized as follows.

1. Our polarization data revealed three IRNCs associated with IRS 2, and several local IRNe. In addition, the illuminating sources of the IRNe were identified with near- and mid-IR sources.
2. Aperture photometry of point-like sources, with 314 detected in all three bands, was used to classify sources using a color-color diagram.

3. Aperture polarimetry of the point-like sources allowed positive detection of 241 sources in at least one of the three bands. Most of the near-IR polarizations of the point-like sources can be explained by dichroic polarization.
4. Sources in group Ar are expected to be either background stars or PMS stars with little intrinsic polarization. The histogram of polarization position angles of group Ar sources in the cluster core has a well-defined peak at $\sim 81^\circ$, which we interpret as the projected direction, on the sky, of the magnetic fields in the IRS 2 region. From the 29° standard deviation of the polarization position angles, the strength of the magnetic field projected on the plane of the sky is roughly estimated at $\sim 100 \mu\text{G}$ using the Chandrasekhar-Fermi method.
5. By comparing the observed magnetic field lines and those derived from recent numerical simulations, we suggest that the clump including the IRS 2 region is likely to have formed under the influence of a strong magnetic field. The local magnetic field runs roughly perpendicular to the Galactic magnetic field. The significant difference between the local and Galactic magnetic field directions may imply that the local magnetic field is strong enough to control the cloud dynamics. In fact, the direction of the powerful molecular outflow from IRAS 12 S1 is along the local magnetic field, instead of the Galactic magnetic field.
6. The magnetic field direction inferred from our observations appears to be consistent with that inferred from $350 \mu\text{m}$ thermal continuum emission polarimetry centered around IRAS 12 S1. The $350 \mu\text{m}$ polarization position angles were especially consistent with the group Ar sources in the outer parts of the cluster core.
7. For the group Ar sources, the wavelength dependence of polarization is consistent with the dichroic extinction. Sources in group A0 have a small amount of extinction, and their polarization seems to be caused by the circumstellar scattering. Sources in group B show similar behavior to the group Ar sources in our data.

This work was supported by the Korean Scholarship Foundation. M. T. has been supported by the MEXT, Grants-in-Aid 19204018 and 22000005. This work is based on observations made at the South African Astronomical Observatory (Department of Astronomy, Nagoya University). This work is based in part on observations made with the Spitzer Space Telescope, which is operated by the Jet Propulsion Laboratory, California Institute of Technology under a contract with NASA. This publication makes use of data products from the Two Micron All Sky Survey, which is a joint project of the University of Massachusetts and the Infrared Processing and Analysis Center/California Institute of Technology, funded by the National Aeronautics and Space Administration and the National Science Foundation. This research has made use of the SIMBAD database, operated at CDS, Strasbourg, France, as well as IRAF and the IDL Astronomy Library.

REFERENCES

Adams, M. T., Strom, K. M., & Strom, S. E. 1979, *ApJ*, 230, L183

- Allen, D. A. 1972, *ApJ*, 172, L55
- Alves, F. O., Franco, G. A. P., & Girart, J. M. 2008, *A&A*, 486, L13
- Andersson, B.-G., & Potter, S. B. 2005, *MNRAS*, 356, 1088
- Aspin, C., & Reipurth, B. 2003, *AJ*, 126, 2936
- Banerjee, R., & Pudritz, R. E. 2006, *ApJ*, 641, 949
- Bastien, P., & Menard, F. 1988, *ApJ*, 326, 334
- Bastien, P., & Menard, F. 1990, *ApJ*, 364, 232
- Baxter, E. J., Covey, K. R., Muench, A. A., Fűrész, G., Rebull, L., Szentgyorgyi, A. H. 2009, *AJ*, 138, 963
- Bourke, T. L., Myers, P. C., Robinson, G., & Hyland, A. R. 2001, *ApJ*, 554, 916
- Breger, M., & Hardorp, J. 1973, *ApJ*, 183, L77
- Casali, M. M. 1995, *MNRAS*, 277, 1385
- Caselli, P., Benson, P. J., Myers, P. C., & Tafalla, M. 2002, *ApJ*, 572, 238
- Castelaz, M. W. & Grasdalen, G. 1988, *ApJ*, 335, 150
- Chandrasekhar, S., & Fermi, E. 1953, *ApJ*, 118, 113
- Cho, J., & Lazarian, A. 2005, *ApJ*, 631, 361
- Cohen, M., Harvey, P. M., Wilking, B. A., & Schwartz, R. D. 1984, *ApJ*, 278, 671
- Crutcher, R. M. 1999, *ApJ*, 520, 706
- Dahm, S. E., & Simon, T. 2005, *AJ*, 129, 829
- Dahm, S. E. 2008, in *Handbook of Star Forming Regions Vol. I*
- Dotson, J. L., Vaillancourt, J. E., Kirby, L., Dowell, C. D., Hildebrand, R. H., & Davidson, J. A. 2010, *ApJ*, 186, 406
- Dyck, H. M., & Lonsdale, C. J. 1979, *AJ*, 84, 1339
- Forbrich, J., Tappe, A., Robitaille, T., Muench, A. A., Teixeira, P. S., Lada, E. A., Stolte, A., & Lada, C. J. 2010, *ApJ*, 716, 1453
- Fromang, S., Hennebelle, P., & Teyssier, R. 2006, *A&A*, 457, 371
- Goodman, A. A., Benson, P. J., Fuller, G. A., & Myers, P. C. 1993, *ApJ*, 406, 528
- Goodman, A. A., Jones, T. J., Lada, E. A., & Myers, P. C. 1995, *ApJ*, 448, 748
- Hashimoto, J., Tamura, M., Kandori, R., Kusakabe, N., Nakajima, Y., Kurita, M., Nagata, T., Nagayama, T., Hough, J., & Chrysostomou, A. 2008, *ApJ*, 677, L39
- Heckert, P. A., & Zeilik, M., II. 1981, *AJ*, 86, 1076
- Heckert, P. A., & Zeilik, M. 1984, *AJ*, 89, 1379
- Heiles, C. 2000, *AJ*, 119, 923
- Herbig, G. H. 1954, *ApJ*, 119, 483
- Herbig, G. H. 1974, *ApJ*, *Lick Obs. Bull.*, No. 658
- Hodapp, K.-W. 1994, *ApJ*, 94, 615
- Holland, W. S., Greaves, J. S., Ward-Thompson, D., & Andre, P. 1996, *A&A*, 309, 267
- Houde, M., Dowell, C. D., Hildebrand, R. H., Dotson, J. L., Vaillancourt, J. E., Phillips, T. G., Peng, R., & Bastien, P. 2004, *ApJ*, 604, 717
- Hough, J. H., Aitken, D. K., Whittet, D. C. B., Adamson, A. J., & Chrysostomou, A. 2008, *MNRAS*, 387, 797
- Jones, T. J. 1989, *ApJ*, 346, 728
- Jones, T. J., & Amini, H. 2003, *AJ*, 125, 1418
- Kandori, R., et al. 2006, *Proc. SPIE*, 6269, 159
- Kandori, R., Tamura, M., Kusakabe, N., Nakajima, Y., Nagayama, T., Nagashima, C., Hashimoto, J., Ishihara, A., Nagata, T., Hough, J. H. 2007, *PASJ*, 59, 487
- Kobayashi, Y., Kawara, K., Maihara, T., Okuda, H., Sato, S., & Noguchi, K. 1978, *PASJ*, 30, 377
- Krügel, E., Guesten, R., Schulz, A., & Thum, C. 1987, *A&A*, 185, 283
- Kwon, J., Choi, M., Pak, S., Kandori, R., Tamura, M., Nagata, T., & Sato, S. 2010, *ApJ*, 708, 758
- Lada, C. J., & Adams, F. C. 1992, *ApJ*, 393, 278
- Larson, R. B. 1969, *MNRAS*, 145, 271
- Lazarian, A. 2007, *J. Quant. Spectrosc. Radiat. Transfer*, 106, 225
- Li, Z.-Y., & Nakamura, F. 2006, *ApJ*, 640, 187
- Machida, M. N., Matsumoto, T., Tomisaka, K., & Hanawa, T. 2005a, *MNRAS*, 362, 369
- Machida, M. N., Matsumoto, T., Hanawa, T., & Tomisaka, K. 2005b, *MNRAS*, 362, 382
- Machida, M. N., Inutsuka, S.-I., Matsumoto, T. 2006, *ApJ*, 647, L151
- Margulis, M., Lada, C. J., & Snell, R. L. 1988, *ApJ*, 333, 316
- Margulis, M., Lada, C. J., & Young, E. T. 1989, *ApJ*, 345, 906
- Matsumoto, T., & Tomisaka, K. 2004, *ApJ*, 616, 266
- Matsumoto, T., Nakazato, T., & Tomisaka, K. 2006, *ApJ*, 637, L105
- Nagayama, T., Nagashima, C., Nakajima, Y., Nagata, T., Sato, S., Nakaya, H., Yamamuro, T., Sugitani, K., & Tamura, M. 2003, *Proc. SPIE*, 4841, 459
- Nakamura, F., & Li, Z.-Y. 2007, *ApJ*, 662, 395
- Nakamura, F., & Li, Z.-Y. 2010, in *Proceedings IAU Symposium No. 270*
- Nakano, T. 1998, *ApJ*, 494, 587
- Nakano, T. 1999, in *Proceedings of Star Formation 1999*
- Nakano, T., Nishi, R., & Umebayashi, T. 2002, *ApJ*, 573, 199
- Ostriker, E. C., Stone, J. M., & Gammie, C. F. 2001, *ApJ*, 546, 980
- Peretto, N., André, Ph., & Belloche, A. 2006, *A&A*, 445, 979
- Pérez, M. R., The, P. S., & Westerlund, B. E. 1987, *PASP*, 99, 1050
- Poidevin, F., & Bastien, P. 2006, *ApJ*, 650, 945
- Reipurth, B., Yu, K. C., Moriarty-Schieven, G., Bally, J., Aspin, C., & Heathcote, S. 2004, *AJ*, 127, 1969
- Sargent, A. I., Van Duinen, R. J., Nordh, H. L., Fridlund, C. V. M., Aalders, J. W., & Beintema, D. 1984, *A&A*, 135, 377
- Schreyer, K., Stecklum, B., Linz, H., & Henning, Th. 2003, *ApJ*, 599, 335
- Schwartz, P. R., Thronson, H. A., Jr., Odenwald, S. F., Glaccum, W., Loewenstein, R. F., Wolf, G. 1985, *ApJ*, 292, 231
- Shu, F. H., Allen, A., Shang, H., Ostriker, E. C., Li, Z.-Y. 1999, *The Origin of Stars and Planetary Systems*. Edited by Charles J. Lada and Nikolaos D. Kylafis.
- Stetson, P. B. 1987, *PASP*, 99, 191
- Strom, K. M., Strom, S. E., Wolff, S. C., Morgan, J. & Wenz, M. 1986, *ApJS*, 62, 39
- Sugitani, K., Nakamura, F., Tamura, M., Watanabe, M., Kandori, R., Nishiyama, S., Kusakabe, N., Hashimoto, J., Nagata, T., & Sato, S. 2010, *ApJ*, 716, 299
- Sung, H., Bessell, M. S., & Lee, S.-W. 1997, *AJ*, 114, 2644
- Sung, H., & Bessell, M. S. 2010, *AJ*, 140, 2070
- Tamura, M., & Sato, S. 1989, *AJ*, 98, 1368
- Tamura, M., Gatley, Ian, Joyce, R. R., Ueno, M., Suto, H. & Sekiguchi, M. 1991, *ApJ*, 378, 611
- Tamura, M., Hayashi, S., Itoh, Y., Hough, J. H., & Chrysostomou, A. 1996, *ASPC*, 97, 372
- Tamura, M., et al. 2007, *PASJ*, 59, 467
- Teixeira, P. S., et al. 2006, *ApJ*, 636, L45
- Teixeira, P. S., Zapata, L. A., & Lada, C. J. 2007, *ApJ*, 667, L179
- Tomisaka, K. 1998, *ApJ*, 502, L163
- Tomisaka, K. 2002, *ApJ*, 575, 306
- Vrba, F. J. 1977, *AJ*, 82, 198
- Vrba, F. J., Luginbuhl, C. B., Strom, S. E., Strom, K. M., & Heyer, M. H. 1986, *AJ*, 92, 633
- Vrba, F. J., Strom, S. E., & Strom, K. M. 1988, *AJ*, 96, 680
- Walker, M. F. 1954, *AJ*, 59, 333
- Walker, M. F. 1956, *ApJS*, 2, 365
- Walsh, J. R., Ogura, K., & Reipurth, B. 1992, *MNRAS*, 257, 110

Wang, P., Li, Z.-Y., Abel, T. & Nakamura, F. 2010, *ApJ*, 709, 27
Wardle, J. F. C., & Kronberg, P. P. 1974, *ApJ*, 194, 249
Ward-Thompson, D., Kirk, J. M., Crutcher, R. M., Greaves, J. S., Holland, W. S., & André, P. 2000, *ApJ*, 537, L135
Whittet, D. C. B. 1992, *Dust in the Galactic Environment* (Bristol: Institute of Physics Publishing)
Whittet, D. C. B., Martin, P. G., Hough, J. H., Rouse, M. F., Bailey, J. A., & Axon, D. J. 1992, *ApJ*, 386, 562
Williams, J. P., & Garland, Catherine A. 2002, *ApJ*, 568, 259
Wolf-Chase, G. A., & Walker, C. K. 1995, *ApJ*, 447, 244
Wolf-Chase, G., Moriarty-Schieven, G., Fich, M., & Barsony, M. 2003, *MNRAS*, 344, 809
Young, E. T., Teixeira, P. S., Lada, C. J., Muzerolle, J., Persson, S. E., Murphy, D. C., Siegler, N., Merengo, M., Krause, O., & Mainzer, A. K. 2006, *ApJ*, 642, 972
Ziegler, U. 2005, *A&A*, 435, 385

TABLE 1
PHOTOMETRY OF POINT-LIKE SOURCES IN THE SPOKES CLUSTER

Source	Position		2MASS	J (mag)	H (mag)	K_s (mag)	Group ^a	note
	α J2000.0	δ J2000.0						
1	6 41 16.79	9 30 22.5	J06411679+0930225	15.655	13.819	12.850	Ar	FMS 2-1404, LBM 6274
2	6 41 11.21	9 30 23.3	J06411121+0930235	14.651	14.068	13.823	A0	FMS 2-1308, FMS 397, LBM 6112, RMS 3667
3	6 41 13.40	9 30 23.8	J06411340+0930237	14.554	13.362	12.606	B	FMS 2-1355, LBM 6182, RMS 3727
4	6 41 11.85	9 30 26.7	J06411185+0930267	14.354	13.332	12.807	Ar	FMS 2-1321, LBM 6128, RMS 3680
5	6 41 19.45	9 30 28.7	J06411945+0930286	12.195	11.779	11.728	A0	FMS 2-1464, FMS 431, [FMS2006] 374, LBM 6390, LBM 6391, RMS 3862, PSB 173 SBL 352, VAS 154, [NGC 2264 454, GEN +2.22640454
6	6 41 17.44	9 30 28.7	J06411744+0930287	14.378	12.753	11.847	Ar	FMS 2-1422, [FMS2006] 357, LBM 6308, RMS 3816
7	6 41 03.61	9 30 29.0	J06410360+0930290	12.780	12.049	11.699	A0	FMS 2-1022, FMS 334, [FMS2006] 207, LBM 5810, RMS 3447, PSB 1467, DS 302
8	6 41 07.58	9 30 29.3	J06410757+0930292	17.653	15.283	13.716	B	FMS 2-1195
9	6 41 10.18	9 30 31.1		13.809	13.174	12.902	A0	FMS 2-1287, FMS 389, [FMS2006] 306, LBM 6079, DS 380, ESO-H α 506
10	6 41 19.41	9 30 30.6		14.988	14.004	13.987	A0	
11	6 41 07.16	9 30 36.3		16.680	13.983	12.483	Ar	FMS 2-1177, [FMS2006] 264
12	6 41 23.20	9 30 36.5	J06412320+0930364	13.876	13.222	13.000	A0	FMS 2-1534, FMS 448, [FMS2006] 391, LBM 6595, RMS 3944, DS 453, IfAH α 465
13	6 41 15.88	9 30 37.4	J06411587+0930373	16.136	14.753	13.957	Ar	FMS 2-1392, [FMS2006] 351, LBM 6249
14	6 41 07.05	9 30 37.9	J06410706+0930375	15.486	13.368	12.220	Ar	FMS 2-1171, LBM 5960
15	6 40 53.77	9 30 39.0	J06405377+0930389	10.634	10.385	10.340	A0	FMS 2-763, FMS 262, [FMS2006] 112, [FMS2000] X55, LBM 5400, PSB 86, SBL 218 GSC 00750-01637, TYC 750-1637-1, UBV M 31907, UCAC2 35177843, NGC 2264 116 VAS 83, GEN +2.22640116
16	6 41 08.02	9 30 40.3	J06410801+0930403	13.273	12.612	12.459	A0	FMS 2-1208, FMS 378, [FMS2006] 278, [FMS2000] X109, LBM 5994, RMS 3582, PSB 142 SBL 310, DS 365, IfAH α 411, UCAC2 35177894, CSI+09-063849, NSV 3128 (Eclipsing binary)
17	6 41 22.66	9 30 43.2		17.201	16.173	15.629	Ar	FMS 2-1519, LBM 6558
18	6 40 58.75	9 30 43.7	J06405874+0930439	17.033	15.265	14.413	Ar	FMS 2-882
19	6 41 19.26	9 30 48.7	J06411926+0930487	14.723	14.118	13.883	A0	FMS 2-1462, [FMS2006] 372, LBM 6383, RMS 3856, DS 440, IfAH α 455
20	6 40 56.38	9 30 50.1	J06405638+0930499	15.367	13.988	13.318	Ar	FMS 2-828, LBM 5550
21	6 40 57.77	9 30 50.3	J06405777+0930502	12.986	12.186	11.900	A0	FMS 2-862, FMS 290, [FMS2006] 142, RMS 3276, PSB 94, DS 242, SBL 238, KH α 102 NGC 2264 130, UCAC2 35177851
22	6 41 11.33	9 30 50.9	J06411132+0930508	14.913	14.391	14.079	A0	FMS 2-1311, LBM 6115
23	6 40 58.85	9 30 57.4	J06405884+0930573	11.641	10.932	10.559	A0	FMS 2-887, FMS 298, [FMS2006] 154, RMS 3307, PSB 98, DS 253, SBL 244, DS 253, VAS 93 CSV 822, HBC 226, NGC 2264 133, CSI+09-0638210, [AH2005] GL 989 8 [KW97] 31-38, GSC 00750-01832, UCAC2 35177857, SV* SON 4001, EM* LKH α 43 V* IO Mon (Variable Star of Orion Type)
24	6 40 58.43	9 30 57.9	J06405842+0930579	17.156	15.762	15.057	Ar	FMS 2-874
25	6 40 59.41	9 30 59.6	J06405940+0930595	15.682	15.113	14.808	A0	FMS 2-906, LBM 5627
26	6 41 05.75	9 31 1.3	J06410574+0931012	12.405	11.630	11.390	A0	FMS 2-1109, FMS 353, [FMS2006] 240, [FMS2000] X100, LBM 5902, PSB 126, RMS 3514, DS 337, ESO-H α 486 SBL 298, NGC 2264 162, UCAC2 35177887 [AH2005] GL 989 3 (PMS)
27	6 40 57.23	9 31 2.8	J06405723+0931029	17.035	15.662	15.022	Ar	FMS 2-851, LBM 5597
28	6 41 08.57	9 31 5.9	J06410857+0931058	14.910	13.442	12.613	Ar	FMS 2-1229, LBM 6012
29	6 41 13.11	9 31 6.7	J06411311+0931066	14.355	13.677	13.374	A0	FMS 2-1346, [FMS2006] 330, LBM 6168, RMS 3717, IfAH α 434, DS 401
30	6 41 06.56	9 31 6.8		18.494	16.343	15.040	B	
31	6 41 05.80	9 31 7.3	J06410579+0931072	14.867	14.351	14.004	B	FMS 2-1114, [FMS2006] 243, LBM 5906
32	6 40 54.55	9 31 7.7	J06405455+0931076	16.491	15.309	14.673	Ar	FMS 2-782, LBM 5440
33	6 41 08.99	9 31 8.9	J06410899+0931088	14.191	12.545	11.595	B	FMS 2-1249, LBM 6033, DS 375, ESO-H α 501 (Emission-line Star)
34	6 41 07.41	9 31 11.1	J06410740+0931110	14.047	13.439	13.190	A0	FMS 2-1188, FMS 373, [FMS2006] 271, LBM 5976, RMS 3563, DS 360, IfAH α 408
35	6 41 11.80	9 31 12.3	J06411180+0931123	15.606	14.873	14.388	B	FMS 2-1317, [FMS2006] 316, LBM 6125, RMS 3677
36	6 41 03.05	9 31 15.4	J06410305+0931154	15.017	14.470	14.271	A0	FMS 2-998, LBM 5779, DS 295, IfAH α 374
37	6 41 15.30	9 31 16.2	J06411530+0931163	9.425	9.289	9.287	A0	FMS 2-1384, FMS 414, [FMS2006] 347, PSB 163, VAS 145, HD 262014, NGC 2264 193 BD+09 1347, GEN +2.22640193, GSC 00750-01525, TYC 750-1525-1, UBV M 31949 UCAC2 35177908, uvby98 222640193, [VGK85] NGC 2264 +09 250
38	6 41 07.29	9 31 18.0	J06410729+0931180	13.982	13.356	13.120	A0	FMS 2-1184, FMS 372, [FMS2006] 268, [FMS2000] X107, LBM 5973, PSB 1499, RMS 3556
39	6 41 03.50	9 31 18.4	J06410349+0931184	11.438	11.058	10.988	A0	FMS 2-1015, FMS 330, [FMS2006] 206, [FMS2000] X89, LBM 5803, PSB 117, RMS 3443 SBL 279, VAS 109, HBC 538, JP11 3994, NGC 2264 154, UBV M 31928, UCAC2 35177877 GEN +2.22640154 (PMS), GSC 00750-01201, CSI+09-06383 3, uvby98 222640154
40	6 40 55.49	9 31 21.5	J06405548+0931218	11.511	10.821	10.682	A0	FMS 2-803, FMS 272, [FMS2006] 121, LBM 5501, PSB 90, RMS 3212, NGC 2264 120 SBL 229, VAS 85
41	6 41 22.40	9 31 21.5		17.374	16.238	15.797	Ar	FMS 2-1512, LBM 6539
42	6 41 15.28	9 31 22.2	J06411528+0931222	14.849	13.999	13.362	B	FMS 2-1383
43	6 41 10.15	9 31 22.2	J06411016+0931223	16.863	16.124	15.514	B	FMS 2-1286, LBM 6077
44	6 40 52.49	9 31 24.2		18.408	16.999	16.288	Ar	
45	6 41 23.14	9 31 25.4	J06412313+0931253	15.729	14.919	14.516	A0	FMS 2-1531, LBM 6588, RMS 3941
46	6 41 10.14	9 31 28.5	J06411013+0931285	13.505	12.808	12.558	A0	FMS 2-1284, FMS 390, [FMS2006] 304, LBM 6078, RMS 3635, DS 381, ESO-H α 507
47	6 41 18.38	9 31 29.6	J06411839+0931296	14.294	13.735	13.477	A0	FMS 2-1444, FMS 427, [FMS2006] 368, [FMS2000] X136, LBM 6344, RMS 3840 (PMS)
48	6 40 56.53	9 31 31.0	J06405652+0931308	15.382	13.821	13.149	Ar	FMS 2-834, LBM 5559
49	6 40 58.72	9 31 32.4		17.340	15.996	15.270	Ar	
50	6 40 55.90	9 31 32.4	J06405590+0931324	15.125	13.473	12.764	Ar	FMS 2-813, LBM 5528
51	6 41 13.06	9 31 38.2	J06411306+0931382	14.991	14.301	13.874	A0	FMS 2-1345, FMS 403, LBM 6166, RMS 3714, DS 399, ESO-H α 512
52	6 41 05.97	9 31 39.9	J06410596+0931398	14.302	13.386	13.050	A0	FMS 2-1122, FMS 357, [FMS2006] 246, LBM 5914
53	6 41 05.55	9 31 40.6	J06410554+0931405	13.381	12.626	12.314	A0	FMS 2-1102, FMS 352, [FMS2006] 238, LBM 5897, DS 335, ESO-H α 485
54	6 41 20.72	9 31 40.8	J06412072+0931407	16.312	14.793	13.972	Ar	FMS 2-1486, LBM 6452
55	6 41 19.63	9 31 44.3	J06411963+0931443	11.912	11.246	11.072	A0	FMS 2-1469, FMS 434, [FMS2006] 375, [FMS2000] X138, LBM 6399, PSB 175, RMS 3865, DS 441 SBL 353, VAS 155, IfAH α 456, NGC 2264 455, NSV 3147, UCAC2 35177920 GEN +2.22640455 (PMS)
56	6 40 55.78	9 31 47.9		17.528	16.134	15.547	Ar	FMS 2-808, LBM 5519

TABLE 1—Continued

Source	Position		2MASS	<i>J</i> (mag)	<i>H</i> (mag)	<i>K_s</i> (mag)	Group ^{††}	note
	$\alpha_{J2000.0}$	$\delta_{J2000.0}$						
57	6 40 52.28	9 31 48.0		18.478	16.726	16.005	Ar	[MRC90] RS 1 (Radio-source, dist: 7.52 arcsec, 06 40 51.9, +09 31 53)
58	6 41 14.76	9 31 49.8	J06411477+0931498	18.328	16.028	14.881	Ar	FMS 2-1373
59	6 40 57.66	9 31 50.1	J06405766+0931501	14.395	13.817	13.547	AO	FMS 2-859, FMS 288, [FMS2006] 140, LBM 5624, RMS 3272, DS 241, IfAH α 353
60	6 41 13.29	9 31 50.3	J06411329+0931503	12.766	12.019	11.649	AO	FMS 2-1351, FMS 405, [FMS2006] 333, LBM 6175, PSB 1535, RMS 3722, DS 405, ESO-H α 513, V583 Mon SBL 1024, SVS 1724
61	6 40 59.24	9 31 50.3	J06405923+0931503	14.680	13.601	13.130	Ar	FMS 2-899, [FMS2006] 159, RMS 3317
62	6 41 17.36	9 31 52.2	J06411736+0931519	15.841	15.310	14.984	AO	FMS 2-1418, LBM 6302
63	6 40 56.89	9 31 52.9	J06405689+0931528	16.310	14.665	13.931	Ar	FMS 2-847, LBM 5584
64	6 41 19.69	9 31 54.2	J06411967+0931542	16.663	16.050	15.769	AO	FMS 2-1470, LBM 6401
65	6 41 24.25	9 31 54.2	J06412425+0931541	13.022	12.338	12.188	AO	FMS 2-1569, FMS 450, [FMS2006] 395, LBM 6685, PSB 183, RMS 3969
66	6 41 14.48	9 32 05.9	J06411447+0932058	17.617	15.467	14.527	Ar	FMS 2-1369
67	6 40 53.41	9 32 10.5	J06405341+0932105	16.762	15.465	14.891	Ar	FMS 2-756, LBM 5381
68	6 40 53.95	9 32 10.8		17.829	16.557	15.941	Ar	FMS 2-767, LBM 5409
69	6 41 03.45	9 32 11.7	J06410344+0932117	14.453	13.750	13.387	AO	FMS 2-1014, FMS 331, [FMS2006] 205, LBM 5798, RMS 3442
70	6 41 21.19	9 32 14.6	J06412119+0932146	13.991	13.268	13.045	AO	FMS 2-1496, FMS 441, [FMS2006] 384, [FMS2000] X142, LBM 6476, PSB 1571, DS 448 IfAH α 462 (PMS)
71	6 40 52.56	9 32 16.2		17.906	16.579	15.977	Ar	FMS 2-733, LBM 5324
72	6 40 56.64	9 32 19.6	J06405664+0932196	16.050	14.683	14.050	Ar	FMS 2-836, LBM 5567
73	6 40 58.59	9 32 23.0	J06405859+0932229	17.084	15.202	14.373	Ar	FMS 2-879
74	6 40 56.21	9 32 23.0	J06405621+0932229	15.868	14.595	14.123	Ar	FMS 2-820, LBM 5540, RMS 3232
75	6 41 21.99	9 32 23.6		18.049	16.850	16.246	Ar	FMS 2-1506, LBM 6514
76	6 41 00.03	9 32 23.8	J06410002+0932233	18.283	16.224	15.272	Ar	FMS 2-926
77	6 40 57.09	9 32 27.3	J06405708+0932273	16.563	15.909	15.641	AO	FMS 2-850, LBM 5595
78	6 41 12.76	9 32 28.0	J06411275+0932280	15.477	14.933	14.614	AO	FMS 2-1337, LBM 6154, RMS 3701, DS 395, IfAH α 430
79	6 41 24.23	9 32 29.5		17.300	16.357	16.157	AO	FMS 2-1568, LBM 6684
80	6 41 23.30	9 32 30.2		16.480	15.850	15.403	B	FMS 2-1540, LBM 6607
81	6 41 22.68	9 32 32.4		17.511	16.270	15.640	Ar	FMS 2-1521, LBM 6563
82	6 41 14.84	9 32 35.8	J06411484+0932358	12.549	11.693	11.422	AO	FMS 2-1375, FMS 411, [FMS2006] 343, [FMS2000] X127, LBM 6220, RMS 3746, SBL 336 DS 415, PSB 1541, IfAH α 443 (PMS)
83	6 41 22.77	9 32 39.4	J06412277+0932394	15.697	15.118	14.847	AO	FMS 2-1525, LBM 6572, RMS 3926
84	6 40 55.06	9 32 39.6	J06405505+0932395	17.255	15.630	14.779	Ar	FMS 2-790, LBM 5472
85	6 41 23.64	9 32 40.0	J06412363+0932399	14.708	13.807	13.432	AO	FMS 2-1555, LBM 6641
86	6 41 21.04	9 32 41.7	J06412104+0932417	15.185	14.650	14.335	AO	FMS 2-1495, [FMS2006] 382, LBM 6468, RMS 3895
87	6 41 00.98	9 32 44.5	J06410098+0932444	10.631	9.738	9.243	AO	FMS 2-943, FMS 313, [FMS2006] 179, [FMS2000] X78, LBM 5692, PSB 107, RMS 3373, DS 276, IP Mon [KW97] 31-44, HBH α 715-43, EM* LkH α 47, SBL 260 VAS 98, CSI-09-06383 7, CSV 824, GSC 00750-01777, [AH2005] GL 989 4 HBC 227, NGC 2264 139, SV* SON 4002, UCAC2 35177865, uvby98 222640139 V (Variable Star of Orion Type)
88	6 41 24.45	9 32 45.2	J06412445+0932451	13.008	12.279	12.075	AO	FMS 2-1572, FMS 452, [FMS2006] 396, [FMS2000] X148, LBM 6699, PSB 185, RMS 3977, DS 459 SBL 369, IfAH α 470 (PMS)
89	6 41 24.60	9 32 49.4	J06412459+0932493	16.153	15.260	14.774	AO	FMS 2-1576, LBM 6709
90	6 41 08.54	9 32 50.8	J06410854+0932508	16.557	15.476	14.906	Ar	FMS 2-1227, LBM 6010
91	6 41 18.70	9 32 52.1	J06411870+0932519	16.398	15.800	15.436	AO	FMS 2-1446, LBM 6355
92	6 41 17.05	9 32 52.3	J06411705+0932523	14.299	13.570	13.340	AO	FMS 2-1408, FMS 421, [FMS2006] 355, LBM 6285, RMS 3802, DS 426, IfAH α 449
93	6 41 03.19	9 32 55.0	J06410319+0932550	14.332	13.699	13.293	B	FMS 2-1006, [FMS2006] 201, LBM 5786
94	6 41 18.96	9 32 56.0	J06411896+0932560	17.307	15.783	15.160	Ar	FMS 2-1454, LBM 6367
95	6 41 04.37	9 32 57.4	J06410436+0932576	15.550	15.075	14.906	AO	FMS 2-1060, [FMS2006] 224, LBM 5850
96	6 41 05.06	9 33 00.2	J06410505+0933002	14.142	13.429	13.189	AO	FMS 2-1084, [FMS2006] 231, LBM 5876, DS 324, IfAH α 390
97	6 40 56.99	9 33 01.3	J06405699+0933013	13.814	12.581	11.980	Ar	FMS 2-849, FMS 283, [FMS2006] 136, LBM 5591, RMS 3260, DS 237, IfAH α 349
98	6 41 04.11	9 33 01.8	J06410411+0933018	10.196	10.173	10.226	AO	FMS 2-1044, FMS 340, LBM 5834, PSB 121, HD 261940, BD-09 1342, SBL 283, VAS 115 GEN +2.22640157, GSC 00750-01671, JP11 3995, NGC 2264 157, TYC 750-1671-1 UBV M 31931, UCAC2 35177880, uvby98 222640157, [VGR85] NGC 2264 +09 241
99	6 40 59.05	9 33 01.8	J06405906+0933019	15.858	15.266	14.934	AO	FMS 2-895
100	6 41 23.06	9 33 04.1	J06412305+0933039	16.474	15.350	14.847	Ar	FMS 2-1530, LBM 6583
101	6 41 19.25	9 33 06.5	J06411921+0933066	17.736	16.256	15.645	Ar	FMS 2-1460, LBM 6384
102	6 40 55.51	9 33 07.9		18.432	16.497	15.470	Ar	
103	6 41 06.23	9 33 08.8	J06410623+0933087	14.097	13.395	13.084	AO	FMS 2-1131, FMS 359, [FMS2006] 250, LBM 5927, RMS 3527, DS 343, IfAH α 400
104	6 41 05.37	9 33 13.4	J06410536+0933134	12.505	11.840	11.663	AO	FMS 2-1094, FMS 351, [FMS2006] 234, [FMS2000] X98, LBM 5894, PSB 125, RMS 3500, DS 333 V812 Mon, J 1046, MR 3470, SBL 296, VVO 41C, VVO C41, IfAH α 395 NGC 2264 160, UCAC2 35177886, [YTL2006] 33 (Variable Star of Orion Type)
105	6 40 55.15	9 33 18.6	J06405514+0933186	15.256	14.602	14.378	AO	FMS 2-792, FMS 268, [FMS2006] 116, LBM 5475, RMS 3199, DS 212, IfAH α 334
106	6 41 14.25	9 33 21.3		14.800	14.192	13.932	AO	FMS 2-1366, LBM 6203
107	6 41 14.46	9 33 21.4	J06411446+0933214	12.613	11.897	11.716	AO	FMS 2-1368, FMS 409, [FMS2006] 340, [FMS2000] X126, LBM 6209, PSB 161, RMS 3738, DS 411 IfAH α 442, HBH α 715-69, SBL 335, NGC 2264 191 UCAC2 35177906, [KW97] 32-9 (PMS)
108	6 40 59.06	9 33 22.2	J06405905+0933222	13.894	13.043	12.603	AO	FMS 2-894, [FMS2006] 158, DS 257, ESO-H α 446 (Emission-line Star)
109	6 40 53.63	9 33 24.7	J06405363+0933247	12.359	11.663	11.306	AO	FMS 2-762, FMS 263, [FMS2006] 111, [FMS2000] X54, LBM 5394, PSB 85, RMS 3157, DS 206, EM* LkH α 35 [AH2005] GL 989 6, V419 Mon, SBL 217 VAS 82, CSI-09-06382 2, GEN +2.22640115, HBC 223, NGC 2264 115 SV* SON 5196, UCAC2 35177842, [KW97] 31-28 (Variable Star of Orion Type)
110	6 41 10.28	9 33 25.0	J06411027+0933250	13.578	12.832	12.587	AO	FMS 2-1290, FMS 392, [FMS2006] 307, LBM 6081, RMS 3639, DS 382, IfAH α 420
111	6 40 59.27	9 33 25.0	J06405926+0933250	12.979	11.477	10.563	B	FMS 2-900, [FMS2006] 160, DS 258, ESO-H α 448 (Emission-line Star)
112	6 40 55.28	9 33 25.0	J06405527+0933249	15.111	14.463	14.253	AO	FMS 2-796, FMS 271, [FMS2006] 118, LBM 5486, RMS 3206
113	6 41 20.41	9 33 25.6		18.587	17.212	16.697	Ar	

TABLE 1—Continued

Source	Position		2MASS	J (mag)	H (mag)	K_s (mag)	Group ^a	note
	$\alpha_{J2000.0}$	$\delta_{J2000.0}$						
114	6 41 19.13	9 33 26.1		17.217	16.016	15.465	Ar	FMS 2-1457, LBM 6378
115	6 41 03.08	9 33 27.6		16.801	16.258	15.974	A0	FMS 2-999, LBM 5781
116	6 40 58.05	9 33 29.9		17.211	16.511	15.970	B	
117	6 40 58.51	9 33 31.7	J06405851+0933317	10.262	10.195	10.210	A0	FMS 2-878, FMS 294, [FMS2006] 149, [FMS2000] X65, PSB 96, HD 261902, BD+09 1339 SBL 242, VAS 91, GEN +2.22640132, GSC 00750-01767, JP11 3987 NGC 2264 132, TYC 750-1767-1, UBVM 31914, UCAC2 35177855, uvby98 222640132 [VGK85] NGC 2264 +09 233 (PMS)
118	6 41 21.30	9 33 32.7		17.951	16.791	16.181	Ar	FMS 2-1499, LBM 6481
119	6 40 59.37	9 33 33.4	J06405936+0933333	13.433	12.232	11.517	B	FMS 2-905, FMS 302, [FMS2006] 163, PSB 101, SBL 1015, ESO-H α 449, NGC 2264 135
120	6 41 21.01	9 33 36.1	J06412100+0933361	12.324	11.537	11.182	A0	FMS 2-1493, FMS 440, [FMS2006] 383, [FMS2000] X141, LBM 6467, PSB 177, RMS 3893, DS 447 EM* LkH α 70, OV Mon, SBL 357, VAS 159, CSI-09-06386 6, HBC 540 NGC 2264 204, SV* SON 5201, [KW97] 32-18 (Variable Star of Orion Type)
121	6 41 19.12	9 33 37.0	J06411911+0933369	15.408	14.223	13.663	Ar	FMS 2-1456, LBM 6377
122	6 41 17.93	9 33 37.0	J06411792+0933370	12.651	11.960	11.755	A0	FMS 2-1432, FMS 424, [FMS2006] 360, [FMS2000] X134, LBM 6327, PSB 170, RMS 3827, DS 432, IfAH α 452 SBL 348, VAS 152, NGC 2264 198, UCAC2 35177915 (PMS)
123	6 41 07.48	9 33 36.9	J06410748+0933369	14.310	13.613	13.236	A0	FMS 2-1192, LBM 5980, RMS 3566
124	6 41 10.12	9 33 42.6	J06411011+0933427	14.914	14.378	14.154	A0	FMS 2-1283, LBM 6075, RMS 3634
125	6 41 18.23	9 33 45.0	J06411822+0933448	16.375	15.786	15.590	A0	FMS 2-1439, LBM 6337, DS 434, IfAH α 453
126	6 41 08.96	9 33 46.0	J06410896+0933460	12.993	12.158	11.833	A0	FMS 2-1247, FMS 382, [FMS2006] 291, LBM 6032, PSB 1508, RMS 3611, DS 374, ESO-H α 500 RMS 3611, SBL 1021
127	6 41 05.76	9 33 48.0		17.965	17.238	16.456	B	FMS 2-1110, LBM 5901
128	6 41 04.05	9 33 48.6	J06410405+0933486	14.996	13.599	12.959	Ar	FMS 2-1041, [FMS2006] 215, LBM 5831
129	6 41 22.04	9 33 49.1	J06412202+0933491	17.243	16.013	15.401	Ar	FMS 2-1508, LBM 6518
130	6 41 16.55	9 33 49.7	J06411653+0933498	16.930	15.365	14.663	Ar	FMS 2-1401, LBM 6266
131	6 41 23.62	9 33 49.8	J06412363+0933497	15.681	15.131	14.882	A0	FMS 2-1554, LBM 6639, DS 456, IfAH α 468
132	6 41 18.27	9 33 53.6	J06411827+0933535	12.583	11.858	11.631	A0	FMS 2-1440, FMS 426, [FMS2006] 364, [FMS2000] X135, LBM 6339, PSB 171, RMS 3836, DS 435 EM* LkH α 68, V432 Mon, SBL 349, VAS 153, CSI-09-06386 4, HBC 237 GEN +2.22640199, HBH α 715-55, NGC 2264 199, SV* SON 5200, UCAC2 35177916 [KW97] 32-16 (Variable Star of Orion Type)
133	6 41 05.62	9 33 55.0	J06410562+0933549	16.538	14.585	13.375	B	FMS 2-1105, LBM 5898
134	6 41 23.78	9 33 56.6	J06412378+0933565	10.659	10.465	10.440	A0	FMS 2-1556, FMS 449, [FMS2006] 394, LBM 6648, PSB 182, SBL 366, VAS 165, JP11 4005 CSI-09-06386 2, GEN +2.22640209, GSC 00750-01779, NGC 2264 209, UBVM 31957 UCAC2 35177926, uvby98 222640209
135	6 40 59.31	9 33 58.2	J06405930+0933583	16.886	15.161	14.272	Ar	FMS 2-902
136	6 41 20.57	9 34 05.4		18.121	16.680	16.072	Ar	
137	6 41 20.10	9 34 07.1		17.718	16.546	16.044	Ar	FMS 2-1479, LBM 6418
138	6 41 01.41	9 34 08.1	J06410141+0934081	12.357	11.723	11.548	A0	FMS 2-953, FMS 315, [FMS2006] 184, [FMS2000] X80, LBM 5704, PSB 108, RMS 3378 [AH2005] GL 989 5, V605 Mon, SBL 263, VAS 100, GEN +2.22640141, NGC 2264 141 SV* SVS 1557, UBVM 31919, UCAC2 35177866 (PMS)
139	6 41 10.93	9 34 08.3	J06411093+0934082	17.721	15.096	13.478	B	FMS 2-1299
140	6 41 19.47	9 34 08.8		18.131	16.707	16.102	Ar	FMS 2-1465, LBM 6392
141	6 41 08.21	9 34 09.4	J06410821+0934094	13.012	11.887	11.513	Ar	FMS 2-1216, [FMS2006] 281, LBM 6002, RMS 3591, DS 367, ESO-H α 496
142	6 41 05.42	9 34 09.4	J06410542+0934095	14.545	13.946	13.623	A0	FMS 2-1097, LBM 5895, RMS 3502, VVO 32C
143	6 41 11.06	9 34 12.4	J06411106+0934123	15.337	13.733	12.908	Ar	FMS 2-1306, LBM 6105
144	6 41 14.75	9 34 13.4	J06411475+0934134	13.536	12.474	11.741	B	FMS 2-1372, FMS 410, [FMS2006] 342, LBM 6216, PSB 1540, RMS 3743, DS 413 SBL 1025, ESO-H α 516
145	6 41 08.54	9 34 13.2	J06410854+0934132	16.278	13.157	11.766	Ar	FMS 2-1228, [FMS2006] 287
146	6 40 56.31	9 34 17.9	J06405630+0934180	14.580	13.892	13.693	A0	FMS 2-827, FMS 275, [FMS2006] 130, LBM 5548, RMS 3236, DS 229, IfAH α 343
147	6 41 20.94	9 34 18.1	J06412093+0934181	16.518	15.934	15.722	A0	FMS 2-1492, FMS 438, LBM 6464, RMS 3891, DS 445, IfAH α 460
148	6 41 10.43	9 34 18.6	J06411042+0934186	17.361	14.219	12.509	Ar	FMS 2-1295, [FMS2006] 310
149	6 41 02.59	9 34 18.9	J06410258+0934190	12.421	12.060	12.003	A0	FMS 2-988, FMS 320, LBM 5761, PSB 114, RMS 3413, SBL 273, VAS 106, GSC 00750-01161 NGC 2264 148, GEN +2.22640148, UBVM 31925, UCAC2 35177872
150	6 41 17.73	9 34 21.8	J06411774+0934219	16.022	14.686	14.045	Ar	FMS 2-1428, LBM 6317
151	6 41 10.30	9 34 21.9	J06411029+0934219	18.612	14.696	12.621	Ar	FMS 2-1291, [FMS2006] 308
152	6 40 59.72	9 34 22.2	J06405972+0934222	16.246	15.132	14.468	B	FMS 2-918, LBM 5640
153	6 41 00.31	9 34 24.3	J06410030+0934243	14.974	14.371	14.065	A0	FMS 2-932, FMS 308, LBM 5663
154	6 41 18.73	9 34 25.6		17.520	16.206	15.516	Ar	FMS 2-1447, LBM 6356
155	6 40 56.96	9 34 27.2	J06405689+0934272	16.307	15.738	15.441	A0	FMS 2-846, LBM 5587
156	6 41 22.01	9 34 29.0		17.467	16.272	15.771	Ar	FMS 2-1507, LBM 6515
157	6 41 01.56	9 34 33.0	J06410156+0934329	14.281	12.237	11.238	Ar	FMS 2-957, LBM 5710
158	6 41 17.07	9 34 33.5	J06411706+0934335	14.245	11.715	10.516	Ar	FMS 2-1409, LBM 6287
159	6 41 07.44	9 34 33.6	J06410744+0934335	15.068	14.441	14.184	A0	FMS 2-1190, [FMS2006] 272, LBM 5978, RMS 3565, DS 361, ESO-H α 494
160	6 41 01.83	9 34 34.2	J06410182+0934342	16.605	13.583	11.690	B	FMS 2-971
161	6 40 56.48	9 34 37.9		17.316	16.689	16.300	A0	FMS 2-832, LBM 5555
162	6 41 20.91	9 34 39.6	J06412090+0934394	17.065	15.698	15.052	Ar	FMS 2-1491, LBM 6463
163	6 40 59.54	9 34 43.5		16.904	16.381	15.985	B	FMS 2-911, LBM 5631
164	6 40 56.42	9 34 44.3	J06405641+0934442	16.215	15.662	15.299	B	FMS 2-830, LBM 5552, RMS 3241
165	6 41 20.86	9 34 44.8	J06412085+0934448	15.066	14.376	13.985	A0	FMS 2-1490, LBM 6461, RMS 3888, DS 446, IfAH α 461
166	6 41 06.74	9 34 46.0	J06410673+0934459	11.264	9.937	8.974	B	FMS 2-1160, FMS 366, [FMS2006] 260, LBM 5949, PSB 133, RMS 3541, DS 349, V608 Mon SBL 1020, CSV 102519, KH α 112, NGC 2264 166, SV* SVS 1544 UCAC2 35177890, uvby98 222640166, [KW97] 31-55, [MRC90] IRS A (Variable Star of Orion Type)
167	6 41 05.88	9 34 46.0		16.624	13.688	12.306	Ar	FMS 2-1116, [FMS2006] 244
168	6 41 24.35	9 34 46.2	J06412434+0934461	12.543	11.396	10.952	Ar	FMS 2-1571, LBM 6693

TABLE 1—Continued

Source	Position		2MASS	<i>J</i> (mag)	<i>H</i> (mag)	<i>K_s</i> (mag)	Group ^a	note
	α -J2000.0	δ -J2000.0						
169	6 41 06.07	9 34 46.3	J06410604+0934461	16.252	13.658	12.435	Ar	FMS 2-1126, [FMS2006] 248, LBM 5920
170	6 41 07.98	9 34 46.9	J06410798+0934469	13.950	12.693	12.096	Ar	FMS 2-1207, [FMS2006] 277, LBM 5992, RMS 3580
171	6 41 19.23	9 34 49.2	J06411921+0934491	16.684	15.330	14.665	Ar	FMS 2-1461, LBM 6381
172	6 41 01.12	9 34 52.2	J06410111+0934522	13.434	12.691	12.476	A0	FMS 2-946, [FMS2006] 181, LBM 5696, DS 277, SBL 261, KH α 107
173	6 40 58.44	9 34 52.5	J06405843+0934525	15.157	14.535	14.299	A0	FMS 2-876
174	6 41 01.33	9 34 52.6	J06410133+0934526	13.644	12.873	12.526	A0	FMS 2-950, [FMS2006] 183, LBM 5701, DS 278, SBL 262, ESO-H α 462
175	6 41 03.79	9 34 53.9		16.615	16.060	15.716	A0	FMS 2-1031, LBM 5819
176	6 41 07.40	9 34 54.9	J06410740+0934549	17.943	14.082	12.023	Ar	FMS 2-1189, [FMS2006] 270
177	6 41 02.54	9 34 55.8	J06410253+0934557	12.398	11.830	11.697	A0	FMS 2-984, FMS 321, [FMS2006] 190, [FMS2000] X85, LBM 5757, PSB 112, RMS 3411 V781 Mon, J 997, MR 3312, SBL 271, VAS 105, VVO 26C, VVO C26, CSV 102518 GEN +2.22640149, NGC 2264 149, NSV 3115, UCAC2 35177870 (Variable Star of Orion Type)
178	6 41 04.17	9 34 57.1	J06410417+0934572	14.740	14.198	13.731	B	FMS 2-1046, [FMS2006] 217, LBM 5837, RMS 3463, NSV 17078, V809 Mon (Variable Star of Orion Type)
179	6 40 59.98	9 35 00.9	J06405998+0935009	16.309	14.398	13.256	B	FMS 2-924, [FMS2006] 171, LBM 5652
180	6 41 24.00	9 35 01.5	J06412399+0935016	16.558	15.645	15.209	A0	FMS 2-1562, LBM 6663
181	6 41 06.42	9 35 06.0	J06410640+0935061	16.581	15.966	15.754	A0	FMS 2-1139, LBM 5937
182	6 41 12.51	9 35 08.8	J06411251+0935088	14.060	13.446	13.162	A0	FMS 2-1333, [FMS2006] 323, LBM 6146
183	6 41 22.00	9 35 09.0	J06412199+0935089	16.976	15.361	14.687	Ar	FMS 2-1505, LBM 6516
184	6 40 59.55	9 35 10.9	J06405954+0935109	11.701	10.787	10.431	A0	FMS 2-912, FMS 305, [FMS2006] 167, [FMS2000] X71, LBM 5633, RMS 3330, DS 260, SBL 251 HBH α 715-68, J 956, MR 3171, V421 Mon, PSB 102, UBVM 31916 VVO 28C, VVO C28, GEN +2.22640136, KH α 104, NGC 2264 136, UCAC2 35177861 [KW97] 31-43 (Variable Star of Orion Type)
185	6 41 02.59	9 35 13.1	J06410258+0935131	12.950	12.271	12.116	A0	FMS 2-987, FMS 322, [FMS2006] 193, [FMS2000] X86, LBM 5762, PSB 113, RMS 3412, DS 287, SBL 272 IfAH α 368, V807 Mon, CSV 6479, GEN +2.22640150, NSV 3116 NGC 2264 150, UCAC2 35177871 (Variable Star of Orion Type)
186	6 41 10.82	9 35 14.6	J06411082+0935148	15.698	15.147	14.906	A0	FMS 2-1298, LBM 6096
187	6 40 57.47	9 35 14.7	J06405747+0935147	15.409	14.681	14.278	A0	FMS 2-856, LBM 5613, DS 239, IfAH α 351
188	6 41 20.67	9 35 16.9	J06412067+0935169	16.478	15.241	14.553	Ar	FMS 2-1484, LBM 6450
189	6 41 18.77	9 35 19.0		16.811	16.291	15.858	B	FMS 2-1449, LBM 6359
190	6 41 07.39	9 35 20.7	J06410739+0935207	14.599	13.163	12.218	B	FMS 2-1187, LBM 5975
191	6 41 04.07	9 35 21.0	J06410406+0935211	13.049	12.326	12.086	A0	FMS 2-1042, FMS 339, [FMS2006] 216, [FMS2000] X93, LBM 5832, PSB 120, RMS 3461, DS 308, SBL 282 GEN +2.22640155, IfAH α 382, NGC 2264 155, UBVM 31929 UCAC2 35177879 (PMS)
192	6 41 16.49	9 35 22.4		17.443	16.690	16.041	B	FMS 2-1399, LBM 6264
193	6 41 23.16	9 35 22.7	J06412316+0935226	14.993	14.423	14.123	A0	FMS 2-1533, [FMS2006] 390, LBM 6592, RMS 3942
194	6 41 11.83	9 35 22.8	J06411184+0935230	17.752	15.432	14.288	Ar	FMS 2-1318
195	6 41 22.16	9 35 24.3	J06412215+0935241	16.879	15.563	14.988	Ar	FMS 2-1509, LBM 6526
196	6 41 21.32	9 35 24.6	J06412131+0935244	16.998	15.623	15.020	Ar	FMS 2-1500, LBM 6485
197	6 41 03.50	9 35 24.7	J06410350+0935248	16.484	15.933	15.635	A0	FMS 2-1016, LBM 5802
198	6 41 09.51	9 35 25.4	J06410951+0935254	12.509	11.716	11.508	A0	FMS 2-1260, FMS 384, [FMS2006] 294, LBM 6057, PSB 146, RMS 3620, SBL 318 V611 Mon, SVS 1545, VVO 1C, VVO C1, GEN +2.22640176, NGC 2264 176 UBVM 31938 (Variable Star)
199	6 41 21.61	9 35 27.6		18.179	16.589	16.050	Ar	
200	6 41 05.77	9 35 29.5	J06410577+0935295	16.300	12.431	10.152	B	FMS 2-1113, [FMS2006] 242, [TLY2006] 3 (Infra-Red source)
201	6 41 12.95	9 35 32.3	J06411295+0935322	13.231	12.443	12.220	A0	FMS 2-1341, [FMS2006] 326, LBM 6162, PSB 155, NGC 2264 188, NSV 3136 (Variable Star)
202	6 41 04.30	9 35 33.3	J06410430+0935333	16.242	14.960	14.139	B	FMS 2-1055, [FMS2006] 220, LBM 5845, DS 312, IfAH α 384
203	6 41 02.82	9 35 34.3	J06410281+0935343	17.747	15.011	13.657	Ar	FMS 2-994, [FMS2006] 195
204	6 41 20.12	9 35 35.9	J06412012+0935360	15.896	15.346	15.066	A0	FMS 2-1480, LBM 6420, RMS 3872
205	6 41 22.49	9 35 36.2		17.791	16.494	15.945	Ar	FMS 2-1515, LBM 6546
206	6 41 08.02	9 35 39.5		17.639	16.275	15.431	B	[TLY2006] 11, [PAB2006] D-MM13 (millimetric Radio-source, dist: 7.92 arcsec)
207	6 41 17.38	9 35 39.7		17.964	16.454	15.796	Ar	FMS 2-1421, LBM 6305
208	6 41 15.03	9 35 41.3	J06411502+0935412	17.696	15.710	14.664	Ar	FMS 2-1378
209	6 41 17.23	9 35 43.1	J06411723+0935430	16.095	14.655	13.934	Ar	FMS 2-1415, LBM 6297
210	6 41 03.64	9 35 43.8	J06410364+0935438	18.164	15.002	13.338	Ar	FMS 2-1024, [FMS2006] 209
211	6 41 03.14	9 35 45.1	J06410313+0935450	17.076	14.321	12.873	Ar	FMS 2-1004, [FMS2006] 199
212	6 41 06.59	9 35 45.1	J06410659+0935451	12.838	12.487	12.415	A0	FMS 2-1149, FMS 365, [FMS2006] 258, LBM 5945, PSB 132, RMS 3538, SBL 304 VAS 123, GEN +2.22640167, GSC 00750-01809, NGC 2264 167, uvby98 222640167
213	6 41 13.27	9 35 47.4	J06411326+0935473	14.775	14.168	13.833	A0	FMS 2-1350, LBM 6174
214	6 41 04.32	9 35 47.7	J06410431+0935477	14.243	13.583	13.332	A0	FMS 2-1058, FMS 344, [FMS2006] 221, LBM 5847, RMS 3467
215	6 41 17.46	9 35 48.9		17.783	16.116	15.420	Ar	FMS 2-1423, LBM 6309
216	6 41 12.93	9 35 49.9	J06411293+0935499	9.366	9.359	9.368	A0	FMS 2-1340, [FMS2006] 325, PSB 154, VAS 138, HD 262013, AG+09 759, BD+09 1346 GCRV 4344, GEN +2.22640187, GSC 00750-01107, JP11 4001, NGC 2264 187 PPM 151050, SAO 114267, TYC 750-1107-1, UBVM 31946, UCAC2 35177902 uvby98 222640187, YZ 9 3139, [MRC90] IRS B, [VGK85] NGC 2264 +09 248
217	6 41 05.99	9 35 51.3	J06410599+0935513	12.382	11.911	11.805	A0	FMS 2-1125, FMS 358, [FMS2006] 247, LBM 5916, RMS 3522, VAS 120, NGC 2264 163 GEN +2.22640163, uvby98 222640163
218	6 40 59.30	9 35 52.4	J06405930+0935523	11.936	9.444	(7.771)	B	FMS 2-901, [FMS2006] 161, RMS 3320, * AR 6A+6C
219	6 41 21.53	9 35 52.2		17.525	16.260	15.652	Ar	FMS 2-1501, LBM 6492
220	6 40 56.40	9 35 53.3	J06405639+0935533	12.849	11.815	11.158	B	FMS 2-829, FMS 279, [FMS2006] 131, LBM 5551, RMS 3240, PSB 92, DS 230, SBL 232 AR 2, V350 Mon, EM* LkH α 40, CSI+09-06382 7, HBH α 715-16 NGC 2264 123, UCAC2 35177846, [KW97] 31-34 (Variable Star of Orion Type)
221	6 41 19.12	9 35 53.4		15.073	14.467	14.207	A0	FMS 2-1458, LBM 6379

TABLE 1—Continued

Source	Position		2MASS	<i>J</i> (mag)	<i>H</i> (mag)	<i>K_s</i> (mag)	Group ^{††}	note
	α J2000.0	δ J2000.0						
222	64 18.90	9 35 54.2	J06411890+0935541	14.442	13.714	13.406	A0	FMS 2-1452, FMS 429, [FMS2006] 371, LBM 6364, RMS 3849
223	64 11.00	9 35 55.7	J06411099+0935556	13.163	12.022	11.231	B	FMS 2-1302, FMS 396, [FMS2006] 311, LBM 6102, RMS 3660, DS 387, ESO-H α 509
224	64 106.97	9 35 55.9	J06410696+0935557	16.645	16.073	15.613	B	FMS 2-1168, LBM 5957
225	64 17.39	9 35 56.0	J06411738+0935559	15.506	13.839	13.078	Ar	FMS 2-1420, LBM 6306
226	64 059.34	9 35 57.0		17.063	14.510	13.255	Ar	FMS 2-904, [FMS2006] 162
227	64 100.28	9 35 59.1	J06410028+0935591	16.652	13.444	11.540	B	FMS 2-931, [FMS2006] 174
228	64 059.76	9 35 59.2	J06405975+0935592	15.783	13.289	11.891	B	FMS 2-920, LBM 5643
229	64 103.75	9 36 01.1	J06410374+0936011	15.978	14.158	13.015	B	FMS 2-1030, LBM 5818
230	64 103.62	9 36 04.6	J06410362+0936046	14.232	12.990	12.343	Ar	FMS 2-1023, [FMS2006] 208, LBM 5811
231	64 103.37	9 36 04.8	J06410337+0936048	13.491	12.352	11.900	Ar	FMS 2-1009, FMS 329, [FMS2006] 202, LBM 5792, RMS 3439, DS 300, ESO-H α 471
232	64 101.91	9 36 05.1	J06410189+0936052	17.091	16.425	16.056	A0	FMS 2-974, LBM 5730
233	64 055.79	9 36 06.1	J06405579+0936061	16.443	14.943	14.158	Ar	FMS 2-809, [FMS2006] 125, LBM 5520
234	64 101.23	9 36 09.5	J06410123+0936095	17.556	14.577	13.036	Ar	FMS 2-949, [FMS2006] 182
235	64 100.64	9 36 10.1	J06410063+0936103	14.379	12.728	11.935	Ar	FMS 2-940, [FMS2006] 178, LBM 5680
236	64 122.83	9 36 10.9	J06412282+0936108	14.840	13.773	13.278	Ar	FMS 2-1527, LBM 6574, RMS 3928
237	64 120.05	9 36 11.9		17.409	16.012	15.465	Ar	FMS 2-1477, LBM 6414
238	64 100.56	9 36 12.3		14.490	13.446	12.993	Ar	FMS 2-939, [FMS2006] 177, LBM 5679, RMS 3362
239	64 058.67	9 36 13.2	J06405867+0936132	12.406	11.571	11.182	A0	FMS 2-881, FMS 297, [FMS2006] 151, RMS 3302, DS 251, EM* LkH α 42, [KW97] 31-39 V420 Mon, CSI-09-06382 9 (Variable Star of Orion Type)
240	64 102.60	9 36 15.6	J06410258+0936156	13.358	11.118	9.914	Ar	FMS 2-989, [FMS2006] 192, LBM 5759, \neq RNO-West
241	64 102.81	9 36 16.2	J06410281+0936161	14.208	11.097	9.162	B	FMS 2-992, [FMS2006] 194, LBM 5771, [CG88] RNO-East, [SD2005] EXS-26 XMMU J064102.8+093616
242	64 116.85	9 36 20.6	J06411684+0936206	13.519	12.824	12.575	A0	FMS 2-1405, FMS 420, [FMS2006] 354, [FMS2000] X132, LBM 6276, PSB 1550, RMS 3795 SBL 1038 (PMS)
243	64 102.89	9 36 21.5	J06410288+0936214	16.571	14.131	12.947	Ar	FMS 2-995
244	64 106.20	9 36 23.0	J06410620+0936229	11.718	11.097	10.742	A0	FMS 2-1130, FMS 360, [FMS2006] 249, [FMS2000] X101, LBM 5924, PSB 131, RMS 3525, DS 342 V360 Mon, HBC 231, HBH α 715-54, ESO-H α 488, EM* LkH α 53 SBL 303, VAS 122, CSI-09-06384 4, GEN +2.22640164, GSC 00750-01759, [NYS2000] H2 NGC 2264 164, SV* SON 5181, UCAC2 35177889, uvby98 222640164 V, [KW97] 31-51 (Variable Star of Orion Type)
245	64 117.19	9 36 23.2	J06411718+0936231	17.193	15.260	14.398	Ar	FMS 2-1414, LBM 6296
246	64 104.71	9 36 26.7	J06410471+0936267	10.728	10.555	10.506	A0	FMS 2-1077, FMS 349, [FMS2006] 229, [FMS2000] X96, LBM 5865, PSB 124, SBL 290 VAS 118, HD 261939, CSI-09-06383 4, GEN +2.22640159, GSC 00750-01762 NGC 2264 159, TYC 750-1762-1, UBV M 31933, UCAC2 35177884, uvby98 222640159 (PMS) [VGK85] NGC 2264 -09 242
247	64 109.62	9 36 29.1	J06410962+0936291	15.608	13.752	12.836	Ar	FMS 2-1265, [FMS2006] 298, LBM 6061
248	64 120.52	9 36 29.7	J06412052+0936297	16.796	15.692	15.076	Ar	FMS 2-1482, LBM 6437
249	64 101.75	9 36 30.2	J06410175+0936301	18.334	15.043	13.443	Ar	FMS 2-968
250	64 056.16	9 36 31.0	J06405616+0936309	11.446	10.489	9.861	B	FMS 2-819, [FMS2006] 127, LBM 5538, PSB 91, DS 227, CI* NGC 2264 AR 1, AN 15.1924, SBL 1010, CSI-09-06382 5, NGC 2264 122, [KW97] 31-32, EM* LkH α 38, GQ Mon (Variable Star of Orion Type)
251	64 100.25	9 36 31.2	J06410025+0936311	16.108	14.173	13.088	Ar	FMS 2-929, [FMS2006] 173, LBM 5659
252	64 105.76	9 36 32.0	J06410576+0936319	14.819	14.205	13.962	A0	FMS 2-1112, FMS 354, [FMS2006] 241, LBM 5903
253	64 123.43	9 36 33.1		17.809	16.705	16.339	Ar	FMS 2-1547, LBM 6618
254	64 104.74	9 36 33.2		16.978	16.484	16.216	A0	
255	64 059.82	9 36 33.4	J06405981+0936332	18.168	16.183	14.590	C	FMS 2-921
256	64 102.59	9 36 40.2	J06410259+0936402	14.285	13.552	13.151	A0	FMS 2-990, [FMS2006] 191, LBM 5760, RMS 3414
257	64 118.07	9 36 41.1	J06411806+0936409	16.291	14.935	14.325	Ar	FMS 2-1434, LBM 6333
258	64 104.44	9 36 43.3	J06410444+0936433	13.989	13.159	12.715	A0	FMS 2-1064, [FMS2006] 225, LBM 5854, PSB 1479, DS 313, ESO-H α 477, SV* SVS 1722 V581 Mon (Variable Star)
259	64 123.98	9 36 44.8	J06412397+0936447	15.722	14.764	14.310	A0	FMS 2-1561, LBM 6661, RMS 3962
260	64 053.62	9 36 46.1	J06405362+0936461	15.964	15.425	15.146	A0	FMS 2-760, [FMS2006] 110, LBM 5392, RMS 3156
261	64 112.98	9 36 47.2		18.326	16.690	15.946	Ar	
262	64 118.74	9 36 48.2		17.773	16.618	15.893	B	FMS 2-1448, LBM 6357
263	64 103.07	9 36 52.0		18.902	16.739	15.620	Ar	
264	64 114.88	9 36 53.0		18.272	16.569	15.713	Ar	
265	64 058.09	9 36 53.4	J06405809+0936533	13.219	12.439	11.987	A0	FMS 2-869, [FMS2006] 146, RMS 3284, DS 246, ESO-H α 442
266	64 104.19	9 36 55.5	J06410419+0936556	14.677	14.072	13.810	A0	FMS 2-1047, [FMS2006] 219, LBM 5841, RMS 3465
267	64 108.20	9 36 56.1	J06410820+0936561	13.758	12.183	11.444	Ar	FMS 2-1215, [FMS2006] 280, LBM 6001, RMS 3588
268	64 059.63	9 36 57.6	J06405962+0936575	14.870	14.081	13.641	A0	FMS 2-915, [FMS2006] 169, LBM 5634, RMS 3333, DS 263, IFAH α 359
269	64 055.86	9 36 59.0	J06405586+0936590	15.835	15.329	15.129	A0	FMS 2-812, LBM 5525, RMS 3222
270	64 107.24	9 36 59.1		17.085	16.568	16.147	B	FMS 2-1183, [FMS2006] 267, LBM 5970
271	64 121.03	9 36 59.6	J06412102+0936596	15.577	14.934	14.605	A0	FMS 2-1494, LBM 6469, RMS 3894
272	64 057.62	9 37 07.5	J06405761+0937075	14.986	14.338	14.050	A0	FMS 2-858, [FMS2006] 139, LBM 5622, RMS 3270, DS 240, IFAH α 352
273	64 103.93	9 37 11.1	J06410393+0937110	13.978	12.369	11.647	Ar	FMS 2-1035, [FMS2006] 213, LBM 5824, RMS 3454
274	64 101.83	9 37 13.8	J06410183+0937139	16.987	15.219	14.317	Ar	FMS 2-972, LBM 5726
275	64 114.48	9 37 14.3	J06411448+0937143	13.855	13.145	12.896	A0	FMS 2-1370, [FMS2006] 341, [FMS2000] X125, LBM 6210, RMS 3739, DS 412 ESO-H α 515 (PMS)
276	64 117.41	9 37 15.4	J06411737+0937151	16.161	15.488	15.020	B	FMS 2-1419, [FMS2006] 358, LBM 6307
277	64 055.87	9 37 17.8	J06405586+0937177	14.488	13.907	13.630	A0	FMS 2-811, [FMS2006] 126, LBM 5526, RMS 3221, DS 225, IFAH α 341
278	64 055.42	9 37 23.8	J06405542+0937237	12.723	12.037	11.835	A0	FMS 2-802, [FMS2006] 120, [FMS2000] X59, LBM 5498, PSB 89, RMS 3211, DS 217 ESO-H α 438, SBL 228, NGC 2264 119, UCAC2 35177845 (PMS)
279	64 055.50	9 37 27.2		16.705	15.253	14.095	B	

TABLE 1—Continued

Source	Position		2MASS	J (mag)	H (mag)	K_s (mag)	Group ^{††}	note
	α -J2000.0	δ -J2000.0						
280	6 40 59.20	9 37 28.3	J06405919+0937281	18.012	15.521	14.314	Ar	FMS 2-898
281	6 41 01.60	9 37 28.8	J06410160+0937287	14.639	13.826	13.276	B	FMS 2-960, LBM 5714, RMS 3386, DS 279, ESO-H α 463
282	6 41 14.82	9 37 31.8		18.122	16.502	15.836	Ar	FMS 2-1374, LBM 6217
283	6 41 23.14	9 37 34.0	J06412313+0937338	13.871	13.018	12.505	A0	FMS 2-1532, [FMS2006] 389, LBM 6589, RMS 3940, DS 452, ESO-H α 524
284	6 41 24.54	9 37 35.6	J06412454+0937355	13.452	12.776	12.537	A0	FMS 2-1574, [FMS2006] 397, LBM 6706, RMS 3980, DS 460, ESO-H α 526
285	6 41 03.04	9 37 35.8	J06410303+0937357	13.207	11.869	11.214	Ar	FMS 2-997, [FMS2006] 197, LBM 5778, RMS 3428, DS 294, ESO-H α 469
286	6 41 23.38	9 37 40.3		17.419	16.593	16.134	A0	FMS 2-1545, LBM 6613
287	6 41 11.90	9 37 43.9	J06411190+0937438	14.210	12.955	12.237	Ar	FMS 2-1322, [FMS2006] 319, LBM 6129, RMS 3681
288	6 41 11.03	9 37 43.8	J06411102+0937438	15.600	15.084	14.771	A0	FMS 2-1304, LBM 6104
289	6 40 58.44	9 37 44.5	J06405843+0937445	14.232	13.449	13.021	A0	FMS 2-875
290	6 41 03.58	9 37 45.5	J06410356+0937454	16.615	15.243	14.610	Ar	FMS 2-1019, LBM 5808
291	6 40 56.79	9 37 49.0	J06405679+0937490	12.251	11.548	11.297	A0	FMS 2-843, [FMS2006] 135, [FMS2000] X62, LBM 5575, RMS 3253, DS 234, SBL 236 EM* LkH α 41, HBC 225, HBH α 715-14, LU Mon, VAS 88, HBC 225 CSI-09-06382 8, GEN +2.22640126, NGC 2264 126, SV* SON 5178, SV* SVS 1181 UCAC2 35177849, uvby98 222640126 V, [KW97] 31-36, (Variable Star of Orion Type)
292	6 41 23.97	9 37 50.1	J06412397+0937501	16.167	15.218	14.838	A0	FMS 2-1560, LBM 6659
293	6 41 19.55	9 37 51.0		18.079	16.605	15.893	Ar	FMS 2-1467, LBM 6394
294	6 41 08.44	9 37 52.5	J06410843+0937525	14.569	14.008	13.713	A0	FMS 2-1224, [FMS2006] 285, LBM 6008, RMS 3595, DS 370, IfAH α 414
295	6 40 58.34	9 37 56.8	J06405834+0937567	14.768	14.097	13.592	B	FMS 2-871, [FMS2006] 147
296	6 41 15.20	9 37 57.6	J06411521+0937576	13.747	12.977	12.647	A0	FMS 2-1382, [FMS2006] 345, LBM 6232, DS 417, SBL 337, ESO-H α 517
297	6 41 22.46	9 38 01.6		17.927	16.763	16.119	Ar	FMS 2-1514, LBM 6544
298	6 41 20.22	9 38 02.6		17.962	16.312	15.561	Ar	
299	6 41 23.33	9 38 04.5	J06412333+0938044	15.331	14.768	14.462	A0	FMS 2-1542, [FMS2006] 392, LBM 6610, RMS 3948
300	6 41 14.64	9 38 06.9	J06411464+0938069	15.952	14.193	13.333	Ar	FMS 2-1371, LBM 6212
301	6 41 19.28	9 38 07.2	J06411928+0938071	14.210	12.837	12.087	Ar	FMS 2-1463, [FMS2006] 373, LBM 6387, RMS 3857
302	6 41 07.06	9 38 11.2	J06410705+0938112	16.111	15.573	15.253	A0	FMS 2-1170, LBM 5961
303	6 41 13.36	9 38 13.9	J06411336+0938137	13.497	12.374	11.841	Ar	FMS 2-1354, [FMS2006] 335, LBM 6181, ESO-H α 514
304	6 41 08.29	9 38 14.4	J06410828+0938143	12.606	12.282	12.188	A0	FMS 2-1220, LBM 6005, RMS 3592, SBL 311, VAS 127, NGC 2264 171
305	6 41 16.15	9 38 16.4	J06411613+0938166	16.403	15.889	15.556	A0	FMS 2-1395, LBM 6257
306	6 41 15.71	9 38 18.3	J06411571+0938182	11.957	11.629	11.570	A0	FMS 2-1390, [FMS2006] 349, LBM 6247, RMS 3768, VAS 146, GEN +2.22640194 GSC 00750-01856, NGC 2264 194, UCAC2 35177911
307	6 41 19.18	9 38 18.8		17.195	16.497	15.709	C	FMS 2-1459, LBM 6380
308	6 41 17.92	9 38 20.6	J06411791+0938204	16.238	14.233	13.156	Ar	FMS 2-1430, LBM 6328
309	6 41 07.07	9 38 24.0	J06410706+0938235	17.188	15.716	14.952	Ar	FMS 2-1172, LBM 5962
310	6 41 04.74	9 38 24.1	J06410476+0938239	17.585	16.027	15.454	Ar	FMS 2-1078, LBM 5866
311	6 41 18.08	9 38 25.5	J06411808+0938253	13.882	13.283	13.003	A0	FMS 2-1435, [FMS2006] 362, LBM 6334, RMS 3831, DS 433, ESO-H α 521
312	6 41 08.22	9 38 30.4	J06410821+0938303	13.620	12.208	11.412	Ar	FMS 2-1217, [FMS2006] 282, LBM 6003, RMS 3590, DS 366, IfAH α 412
313	6 41 04.57	9 38 30.8	J06410457+0938308	13.779	12.995	12.555	A0	FMS 2-1070, LBM 5861, RMS 3476, DS 318, EM* LkH α 50, HBC 539, SV* SON 5210 [KW97] 31-49, CSI-09-06383 10, PW Mon (Variable Star of Orion Type)
314	6 40 59.30	9 35 49.6		14.531	12.425	10.429	C	CI* NGC 2264 AR 6B (Variable Star of FU Ori type)

NOTES.—Units of right ascension are hours, minutes, and seconds, and units of declination are degrees, arcminutes, and arcseconds. Positions are from the $J-H-K_s$ image (Figure 1). Note that since source 218 was saturated in the K_s band, the K_s magnitude of 7.771 mag obtained from 2MASS Point Source Catalog was only used for the source classification (Figure 13). Also note that the aperture photometry of source 314 (AR 6B) is considered to be affected by the closest source 218 (AR 6A+6C).

[†] Classification based on a color-color diagram (see Section 4.2.1).

^{††} References to Table 1.

[†] AG: Astr. Gesellschaft katalog

[†] [AH2005]: Alvarez, C., & Hoare, M.G. 2005, A&A, 440, 569

[†] AR: Aspin, C., & Reipurth, B. 2003, AJ, 126, 2936

[†] BD: Bonner Durchmusterung

[†] [CG88]: Castelaz, M. W., & Grasdalén, G. 1988, ApJ, 335, 150

[†] CoRoT: Loeillet, B. et al. 2008, A&A, 479, 865

[†] CSI: Catalog of Stellar Identif.

[†] CSI: Jung, J. et al. 1973, BICDS, 4, 27, Ochsenbein, F. et al. 1981, A&AS, 43, 2590, EGRET, D. 1983, BICDS, 24, 109

[†] CSV: Catalog of Suspected Variable *

[†] DS: Dahm, S. E., & Simon, T. 2005, AJ, 129, 829D

[†] EM* LkH α : Lick observatory, H α Em*

[†] ESO-H α : European Southern Observatory, H α

[†] FMS or FMS 2: Flaccomio, E. et al. 1999, A&A, 345, 521F, Flaccomio, E. et al. 2006, A&A, 455, 903F

[†] [FMS2006]: Flaccomio, E. et al. 2006 A&A, 455, 903F

[†] [FMS2000]: Flaccomio, E. et al. 2000 A&A, 355, 651F

[†] GCRV: General catalogue of stellar radial velocities (Wilson R. E. 1953)

[†] GEN: Geneva Identification system

[†] GSC: Guide Star Catalog

[†] HBC: Third catalog of emission-line stars of the Orion population (Herbig, G. H., & Bell, K. R. 1988)

[†] HBH α : Hamburg-Bergedorf, H α

[†] IfAH α : Institute for Astron. in Hawaii, H α

[†] J: Jones, B. F., 1997 (see Soderblom, D. R. et al. 1999, AJ, 118, 1301)

[†] JP11: -

[†] KH α : Kiso observatory, H α

† [KW97]: Kohoutek, L., & Wehmeyer, R. 1997, AAHam, 11, 1
 † BM: Lamm, M. H. et al., 2004 A&A, 417, 557L
 † MR: Meyers-Rice, B. A., 1997, (see Kearns, K. E. et al. AJ, 114, 1098
 † [MRC90]: Mendoza, E. E. et al. 1990, MNRAS, 246, 518
 † NGC 2264: Walker, M. F. 1956, ApJS, 2, 365, Koch, R. H. & Perry, P. M. 1974, AJ, 79, 379, Kuznetsov, V. I. et al. 2000, A&AS, 142, 389
 † NSV: New catalog of Suspected Variable *
 † [PAB2006]: Peretto, N. et al. 2006 A&A, 445, 979P
 † PPM: Position and Proper Motion (Roeser, S., & Bastian, U. 1988, A&AS, 74, 449, Roeser, S. et al. 1994, A&AS, 105, 301)
 † PSB: Park B.-G. et al. 2000, AJ, 120, 894
 † RMS: Rebull, L. M. et al. 2002, AJ, 123, 1528, Lamm, M. H. et al. 2004 A&A, 417, 557L
 † SAO: Smithsonian Astrophysical Observatory
 † SBL: Sung, H. et al. 1997, AJ, 114, 2644, Sung, H. et al. 2004, AJ, 128, 1684
 † [SD2005]: Simon, T., & Dahm, S. E. 2005 ApJ, 618, 795S
 † SV* SON: Sonneberg inst.
 † SV* Son: Identifications of Sonneberg variables (Kinnunen+, 1999-2000)
 † SVS: Sovetskaya Peremennaya Zvezda (Kazarovets E.V. & Samus N. N. 1992, IBVS, 3743, 1)
 † [TLY2006]: Teixeira, P. S. et al. 2006, ApJ, 636, 45
 † TYC: Tycho mission
 † UBV: Blanco, V. M. et al. 1968, PUSNO, 21, 1
 † UCAC2: USNO CCD Astrogaphic Catalog, 2nd catalog (Zacharias, N. et al. 2004, AJ, 127, 3043)
 † uvby98: uvbyB photoelectric photometric catalogue (Hauck, B., & Mermilliod, M. 1998, A&AS, 129, 431)
 † VAS: Vasilevskis, S. et al. 1965, AJ, 70, 797
 † [VGK85]: Catalogue of BV magnitudes and spectral classes for 6000 stars (Voroshilov, V. I. et al. 1985)
 † VVO: Van Vleck Observatory
 † XMMU: XMM-Newton Observatory data, Unregistered
 † [YTL2006]: Young, E. T. et al. 2006, ApJ, 642, 972
 † YZ: Yale observatory, Zone catalog

TABLE 2
POLARIMETRY OF POINT-LIKE SOURCES IN THE SPOKES CLUSTER

Source	P_J (%)	P_H (%)	P_{K_s} (%)	θ_J ($^\circ$)	θ_H ($^\circ$)	θ_{K_s} ($^\circ$)
1	< 6.9	1.7 ± 0.5	< 4.8	...	98.4 ± 7.5	...
2	< 2.8	2.3 ± 0.5	< 10.1	...	73.6 ± 6.6	...
3	< 2.4	2.3 ± 0.3	< 3.1	...	17.3 ± 3.5	...
4	2.8 ± 0.6	1.8 ± 0.2	< 3.1	20.8 ± 5.8	5.3 ± 3.8	...
5	< 0.22	0.25 ± 0.06	< 1.0	...	128.4 ± 6.5	...
6	< 1.4	0.54 ± 0.12	< 1.13	...	144.8 ± 6.2	...
7	0.61 ± 0.12	0.23 ± 0.07	< 0.9	82.3 ± 5.3	178.8 ± 7.8	...
8	50.9 ± 9.4	6.4 ± 1.4	6.8 ± 1.8	179.1 ± 5.2	174.9 ± 6.0	143.4 ± 7.3
9	1.0 ± 0.2	0.90 ± 0.17	< 2.6	79.8 ± 6.9	100.1 ± 5.2	...
10	< 2.7	4.1 ± 0.4	< 7.9	...	179.2 ± 2.8	...
11	10.4 ± 2.9	1.1 ± 0.3	1.2 ± 0.4	112.3 ± 7.7	131.5 ± 7.3	126.9 ± 9.0
12	< 0.6	0.75 ± 0.15	< 2.6	...	65.6 ± 5.6	...
13	6.7 ± 1.5	3.5 ± 0.5	< 5.3	28.7 ± 6.0	15.1 ± 3.8	...
14	5.3 ± 0.9	2.84 ± 0.19	2.0 ± 0.3	117.5 ± 4.8	118.3 ± 1.9	118.0 ± 4.4
15	1.51 ± 0.02	0.58 ± 0.018	0.77 ± 0.06	115.4 ± 0.4	90.5 ± 0.9	116.5 ± 2.0
16	1.14 ± 0.12	1.55 ± 0.08	< 1.0	69.4 ± 2.9	95.9 ± 1.5	...
17	< 8.8	< 4.0	< 18.9
18	13.7 ± 2.5	5.84 ± 0.739	< 5.6	36.5 ± 5.1	47.4 ± 3.6	...
19	< 0.8	< 0.7	< 3.2
20	8.3 ± 0.5	5.11 ± 0.20	3.7 ± 0.6	43.1 ± 1.8	41.8 ± 1.1	44.3 ± 4.7
21	2.23 ± 0.08	1.00 ± 0.04	1.12 ± 0.16	39.5 ± 1.0	28.5 ± 1.2	47.7 ± 4.1
22	< 1.0	0.9 ± 0.3	< 3.9	...	45.8 ± 7.8	...
23	1.41 ± 0.03	1.08 ± 0.02	0.54 ± 0.05	110.6 ± 0.7	110.9 ± 0.6	117.0 ± 2.8
24	< 9.5	5.7 ± 1.0	< 9.4	...	33.6 ± 4.9	...
25	< 2.1	1.9 ± 0.6	< 8.8	...	116.7 ± 8.7	...
26	1.02 ± 0.05	0.93 ± 0.04	< 0.33	90.0 ± 1.4	99.1 ± 1.1	...
27	10.9 ± 2.0	2.8 ± 0.7	< 7.4	38.5 ± 5.2	20.3 ± 6.8	...
28	2.98 ± 0.33	2.33 ± 0.14	1.1 ± 0.3	100.3 ± 3.1	90.0 ± 1.7	71.2 ± 8.6
29	0.99 ± 0.17	0.80 ± 0.11	< 1.8	49.1 ± 4.9	48.8 ± 4.0	...
30	< 20.3	5.7 ± 1.4	< 8.5	...	90.7 ± 6.9	...
31	< 1.0	1.4 ± 0.3	< 3.5	...	153.1 ± 6.6	...
32	9.3 ± 1.0	4.9 ± 0.5	< 5.7	43.2 ± 3.1	49.7 ± 2.9	...
33	2.45 ± 0.16	2.13 ± 0.07	1.32 ± 0.13	112.2 ± 1.9	109.3 ± 0.9	127.5 ± 2.9
34	0.82 ± 0.16	0.62 ± 0.11	< 1.5	89.3 ± 5.3	85.8 ± 4.8	...
35	2.3 ± 0.6	1.3 ± 0.4	< 4.4	166.1 ± 7.2	14.2 ± 8.5	...
36	< 1.1	< 0.8	< 4.2
37	0.998 ± 0.014	1.125 ± 0.012	0.90 ± 0.02	82.5 ± 0.4	66.5 ± 0.3	49.8 ± 0.7
38	< 0.47	0.66 ± 0.11	< 1.4	...	80.8 ± 4.5	...
39	1.10 ± 0.03	0.77 ± 0.02	0.33 ± 0.07	91.9 ± 0.7	92.5 ± 0.8	97.2 ± 5.8
40	1.39 ± 0.03	0.54 ± 0.02	0.45 ± 0.05	94.3 ± 0.6	99.7 ± 1.1	65.4 ± 3.2
41	< 7.3	< 3.71	< 16.5
42	< 1.4	< 0.8	< 2.2
43	< 4.9	< 5.4	< 14.6
44	44.6 ± 10.4	< 12.4	< 31.5	39.6 ± 6.5
45	< 1.8	2.6 ± 0.4	< 5.2	...	80.6 ± 4.2	...
46	0.90 ± 0.09	0.51 ± 0.08	< 0.9	73.6 ± 2.9	79.1 ± 4.3	...
47	0.68 ± 0.17	0.88 ± 0.13	< 1.8	92.9 ± 6.8	79.6 ± 4.2	...
48	7.2 ± 0.4	4.44 ± 0.16	2.1 ± 0.4	39.1 ± 1.7	40.8 ± 1.0	51.8 ± 6.0
49	8.3 ± 2.4	7.4 ± 1.0	< 9.7	46.5 ± 7.9	33.8 ± 3.9	...
50	6.2 ± 0.3	4.32 ± 0.12	1.5 ± 0.3	39.1 ± 1.6	41.5 ± 0.8	35.3 ± 6.1
51	< 1.01	0.7 ± 0.2	< 2.7	...	163.7 ± 8.7	...
52	3.00 ± 0.19	1.90 ± 0.10	< 1.3	88.6 ± 1.8	89.7 ± 1.6	...
53	0.65 ± 0.09	0.53 ± 0.06	< 0.7	83.1 ± 3.8	57.9 ± 3.2	...
54	4.0 ± 1.1	1.5 ± 0.3	< 3.1	71.2 ± 7.7	77.8 ± 5.8	...
55	0.81 ± 0.04	0.90 ± 0.03	0.67 ± 0.07	77.1 ± 1.3	53.2 ± 0.8	48.6 ± 3.1
56	12.0 ± 2.9	4.4 ± 1.1	< 11.3	21.7 ± 6.7	47.0 ± 6.7	...
57	< 36.2	< 9.3	< 27.9
58	< 17.9	< 3.4	< 6.4
59	< 0.6	0.7 ± 0.14	< 1.8	...	51.8 ± 5.3	...
60	0.63 ± 0.06	0.5 ± 0.04	< 0.3	108.2 ± 2.5	87.7 ± 2.4	...
61	2.9 ± 0.2	1.6 ± 0.13	< 1.33	56.1 ± 2.1	52.8 ± 2.3	...
62	< 2.1	< 1.4	< 7.2
63	9.9 ± 1.0	4.4 ± 0.3	< 2.5	42.5 ± 2.9	40.0 ± 1.7	...
64	< 5.2	< 4.3	24.8 ± 4.8	14.7 ± 5.5
65	0.91 ± 0.09	0.55 ± 0.08	< 1.0	137.7 ± 2.7	25.7 ± 4.1	...
66	< 8.7	2.8 ± 0.8	< 5.0	...	64.0 ± 7.4	...

TABLE 2—Continued

Source	P_J (%)	P_H (%)	P_{K_s} (%)	θ_J ($^\circ$)	θ_H ($^\circ$)	θ_{K_s} ($^\circ$)
67	< 6.0	3.5 ± 0.6	< 7.3	...	58.2 ± 5.2	...
68	12.2 ± 3.9	8.0 ± 1.6	< 17.9	72.7 ± 8.7	48.0 ± 5.6	...
69	1.55 ± 0.19	1.46 ± 0.13	< 1.7	56.5 ± 3.5	70.0 ± 2.6	...
70	0.44 ± 0.14	0.57 ± 0.09	< 1.4	84.7 ± 8.9	64.5 ± 4.5	...
71	22.0 ± 7.2	6.3 ± 2.1	< 23.4	41.4 ± 8.9	8.0 ± 8.9	...
72	4.0 ± 0.8	3.5 ± 0.3	4.9 ± 1.1	40.4 ± 5.5	43.5 ± 2.7	47.5 ± 6.1
73	< 5.9	4.0 ± 0.4	< 4.3	...	48.0 ± 3.1	...
74	4.0 ± 0.6	2.0 ± 0.3	< 3.4	24.4 ± 4.5	42.9 ± 4.7	...
75	< 12.7	< 5.9	< 26.7
76	21.7 ± 5.5	< 4.0	< 9.8	100.2 ± 7.1
77	< 3.6	< 2.7	< 12.3
78	1.8 ± 0.5	1.4 ± 0.4	< 5.5	75.9 ± 7.8	96.2 ± 7.4	...
79	< 12.2	< 6.1	< 40.3
80	< 3.3	< 2.9	< 12.6
81	< 7.7	5.0 ± 1.3	< 15.2	...	56.1 ± 7.4	...
82	1.42 ± 0.05	0.93 ± 0.03	1.24 ± 0.10	59.3 ± 1.1	55.5 ± 1.0	34.3 ± 2.3
83	< 1.6	< 1.5	< 7.5
84	13.7 ± 2.4	5.8 ± 0.8	< 6.7	37.4 ± 4.9	28.4 ± 3.8	...
85	4.8 ± 0.3	3.11 ± 0.19	2.8 ± 0.8	57.4 ± 1.7	53.5 ± 1.7	46.1 ± 8.2
86	< 1.3	< 0.8	< 4.5
87	1.81 ± 0.02	1.16 ± 0.014	0.654 ± 0.018	83.1 ± 0.3	87.4 ± 0.3	90.3 ± 0.8
88	0.46 ± 0.11	0.84 ± 0.08	1.7 ± 0.4	46.2 ± 6.4	56.8 ± 2.7	18.6 ± 6.6
89	< 6.3	< 4.5	19.1 ± 5.6	20.2 ± 8.1
90	7.5 ± 1.4	3.8 ± 0.7	< 6.0	64.4 ± 5.2	61.1 ± 5.0	...
91	< 3.1	< 3.1	< 12.3
92	0.62 ± 0.17	0.84 ± 0.13	< 1.7	61.9 ± 7.5	56.6 ± 4.2	...
93	0.7 ± 0.2	< 0.4	< 1.4	77.6 ± 8.0
94	6.9 ± 2.1	3.2 ± 0.9	< 9.0	94.6 ± 8.3	89.1 ± 8.0	...
95	< 2.8	< 2.0	< 8.2
96	0.55 ± 0.18	0.39 ± 0.12	< 1.5	93.7 ± 8.8	73.3 ± 8.3	...
97	1.54 ± 0.13	1.19 ± 0.05	0.60 ± 0.14	48.0 ± 2.5	52.9 ± 1.3	31.1 ± 6.6
98	0.919 ± 0.017	0.347 ± 0.016	0.37 ± 0.04	95.2 ± 0.5	110.0 ± 1.3	177.9 ± 2.8
99	2.8 ± 0.7	< 1.7	< 7.1	28.2 ± 6.6
100	5.1 ± 1.2	4.2 ± 0.7	< 6.5	57.9 ± 6.4	69.7 ± 5.0	...
101	< 9.4	< 4.2	17.4 ± 4.2	86.9 ± 6.7
102	< 16.6	< 4.8	< 10.8
103	< 0.46	0.94 ± 0.09	< 1.2	...	83.9 ± 2.8	...
104	0.72 ± 0.05	0.33 ± 0.04	0.64 ± 0.11	91.9 ± 2.1	90.1 ± 3.1	48.9 ± 4.9
105	< 1.2	< 1.0	< 4.2
106	< 1.0	< 0.8	3.0 ± 1.0	72.9 ± 8.7
107	0.54 ± 0.05	0.31 ± 0.04	< 0.4	86.9 ± 2.8	73.4 ± 3.6	...
108	< 0.65	< 0.4	< 1.0
109	1.63 ± 0.07	0.5 ± 0.03	0.32 ± 0.09	112.9 ± 1.1	124.6 ± 1.6	112.6 ± 7.5
110	0.75 ± 0.10	0.9 ± 0.07	< 0.9	82.2 ± 3.9	56.5 ± 2.3	...
111	4.2 ± 0.09	3.1 ± 0.04	2.51 ± 0.05	9.3 ± 0.6	9.3 ± 0.4	14.0 ± 0.6
112	< 1.1	< 0.9	< 3.74
113	< 27.2	< 10.7	< 36.3
114	7.3 ± 2.4	6.9 ± 1.1	< 10.6	87.7 ± 9.0	70.2 ± 4.4	...
115	< 4.5	< 3.4	< 17.3
116	< 9.2	< 5.1	< 18.7
117	0.902 ± 0.017	0.521 ± 0.015	0.25 ± 0.04	94.4 ± 0.6	109.6 ± 0.8	100.9 ± 3.9
118	< 14.2	< 8.0	< 27.0
119	2.21 ± 0.13	1.98 ± 0.06	1.15 ± 0.12	148.5 ± 1.6	132.4 ± 0.9	121.4 ± 3.1
120	0.25 ± 0.05	0.30 ± 0.03	0.79 ± 0.09	126.3 ± 5.3	19.9 ± 2.8	22.4 ± 3.1
121	5.1 ± 0.5	2.98 ± 0.20	< 2.2	72.2 ± 2.6	72.5 ± 1.9	...
122	< 0.16	0.50 ± 0.04	< 0.4	...	62.9 ± 2.1	...
123	0.84 ± 0.19	< 0.4	< 1.5	64.8 ± 6.4
124	< 0.846	< 0.70	< 3.7
125	< 4.1	< 4.0	< 14.6
126	0.849 ± 0.07	0.54 ± 0.05	< 0.4	102.8 ± 2.4	77.5 ± 2.4	...
127	< 13.4	< 10.1	< 34.8
128	3.6 ± 0.3	3.19 ± 0.12	1.8 ± 0.4	68.5 ± 2.4	65.1 ± 1.1	69.5 ± 6.1
129	< 6.8	< 3.4	< 11.6
130	6.7 ± 1.8	4.9 ± 0.7	< 6.1	85.7 ± 7.4	63.0 ± 3.8	...
131	< 2.8	< 2.3	< 10.5
132	0.61 ± 0.05	0.53 ± 0.04	0.71 ± 0.11	103.6 ± 2.4	66.0 ± 2.0	48.6 ± 4.6

TABLE 2—Continued

Source	P_J (%)	P_H (%)	P_{K_s} (%)	θ_J ($^\circ$)	θ_H ($^\circ$)	θ_{K_s} ($^\circ$)
133	11.0 ± 1.2	5.4 ± 0.4	3.8 ± 0.7	66.0 ± 3.2	74.3 ± 2.1	65.4 ± 5.0
134	0.20 ± 0.02	0.561 ± 0.019	0.76 ± 0.06	62.5 ± 3.0	48.0 ± 1.0	32.0 ± 2.1
135	5.6 ± 1.5	2.8 ± 0.5	< 4.0	40.8 ± 7.4	68.7 ± 4.9	...
136	23.5 ± 5.4	< 5.9	< 21.4	43.1 ± 6.4
137	< 11.6	< 4.6	< 21.3
138	0.46 ± 0.05	0.85 ± 0.03	0.52 ± 0.10	94.7 ± 2.9	108.9 ± 1.1	122.0 ± 5.6
139	< 11.8	< 1.4	< 2.1
140	< 13.6	< 5.6	< 20.7
141	3.98 ± 0.07	2.57 ± 0.05	0.92 ± 0.11	83.5 ± 0.5	79.9 ± 0.6	81.7 ± 3.5
142	1.2 ± 0.2	< 1.0	< 3.8	84.2 ± 5.4
143	4.0 ± 0.5	3.73 ± 0.15	2.1 ± 0.4	53.8 ± 3.6	57.5 ± 1.1	68.7 ± 5.6
144	0.34 ± 0.10	0.39 ± 0.05	0.74 ± 0.13	17.1 ± 7.8	34.3 ± 3.7	27.9 ± 5.1
145	16.5 ± 1.1	9.39 ± 0.15	5.18 ± 0.16	80.2 ± 1.8	78.1 ± 0.5	76.9 ± 0.9
146	< 0.672	0.90 ± 0.14	< 1.9	...	92.2 ± 4.3	...
147	4.1 ± 1.3	< 3.0	< 15.1	28.5 ± 8.6
148	7.5 ± 2.5	5.5 ± 0.2	3.5 ± 0.3	67.6 ± 8.9	66.7 ± 1.2	62.7 ± 2.2
149	0.59 ± 0.05	0.6 ± 0.04	0.48 ± 0.15	87.4 ± 2.3	108.4 ± 2.0	81.0 ± 8.6
150	7.3 ± 0.8	5.3 ± 0.3	3.3 ± 1.0	59.8 ± 3.0	59.4 ± 1.9	45.1 ± 8.6
151	< 23.9	4.0 ± 0.4	2.8 ± 0.3	...	42.3 ± 2.6	30.9 ± 3.3
152	4.4 ± 0.9	2.5 ± 0.5	< 4.57	74.4 ± 5.9	73.6 ± 5.9	...
153	1.0 ± 0.3	< 0.7	< 3.0	158.8 ± 8.5
154	< 8.4	< 3.7	15.5 ± 3.9	45.7 ± 7.0
155	< 3.0	< 2.1	< 10.2
156	< 7.7	< 3.7	< 16.0
157	4.65 ± 0.19	3.09 ± 0.06	2.03 ± 0.11	57.6 ± 1.2	60.4 ± 0.6	61.9 ± 1.6
158	8.94 ± 0.15	6.60 ± 0.03	3.85 ± 0.05	57.8 ± 0.5	60.6 ± 0.1	57.1 ± 0.3
159	< 1.1	< 0.8	< 3.3
160	12.3 ± 1.6	8.5 ± 0.2	5.51 ± 0.19	63.4 ± 3.6	62.0 ± 0.8	60.0 ± 1.0
161	< 7.9	6.6 ± 1.8	< 24.6	...	91.6 ± 7.5	...
162	< 6.7	2.6 ± 0.9	< 8.9	...	80.0 ± 9.0	...
163	< 4.6	< 4.4	< 18.5
164	3.7 ± 1.1	< 2.4	9.7 ± 3.1	56.9 ± 7.8	...	48.7 ± 8.7
165	< 1.1	< 0.7	< 3.2
166	2.77 ± 0.03	1.969 ± 0.016	0.723 ± 0.016	125.7 ± 0.3	126.8 ± 0.2	137.2 ± 0.6
167	13.1 ± 1.7	9.8 ± 0.3	4.9 ± 0.3	81.9 ± 3.6	89.3 ± 0.8	89.5 ± 1.5
168	2.15 ± 0.07	1.8 ± 0.04	1.17 ± 0.13	60.9 ± 0.9	52.6 ± 0.6	25.4 ± 3.1
169	9.5 ± 1.2	8.9 ± 0.2	4.6 ± 0.3	79.9 ± 3.5	82.9 ± 0.8	85.9 ± 1.9
170	4.40 ± 0.14	3.30 ± 0.06	2.29 ± 0.17	64.1 ± 0.9	69.4 ± 0.5	65.8 ± 2.1
171	4.6 ± 1.3	4.8 ± 0.5	< 5.4	40.7 ± 8.0	56.0 ± 3.1	...
172	0.96 ± 0.11	1.10 ± 0.07	< 0.8	84.4 ± 3.1	94.3 ± 1.8	...
173	1.2 ± 0.3	< 0.8	< 3.7	91.4 ± 7.2
174	0.48 ± 0.13	1.05 ± 0.09	< 0.8	99.6 ± 7.4	91.0 ± 2.4	...
175	5.6 ± 1.4	< 4.1	< 16.6	107.2 ± 6.8
176	< 13.4	4.5 ± 0.3	2.43 ± 0.17	...	81.6 ± 1.7	80.4 ± 2.0
177	0.65 ± 0.05	0.93 ± 0.04	0.84 ± 0.12	87.6 ± 2.2	95.3 ± 1.1	89.6 ± 4.0
178	0.9 ± 0.2	< 0.7	< 2.7	112.3 ± 7.2
179	< 3.5	< 0.9	< 1.6
180	6.3 ± 1.7	< 2.9	< 15.5	119.7 ± 7.6
181	< 3.8	4.1 ± 1.1	< 15.3	...	80.9 ± 7.2	...
182	0.52 ± 0.13	0.70 ± 0.13	< 1.4	58.7 ± 7.2	74.6 ± 5.2	...
183	< 5.8	6.0 ± 0.7	< 5.7	...	57.2 ± 3.3	...
184	0.82 ± 0.03	0.67 ± 0.02	0.63 ± 0.04	78.7 ± 1.1	88.2 ± 0.9	75.2 ± 1.9
185	0.64 ± 0.07	0.65 ± 0.05	< 0.52	96.6 ± 2.9	102.3 ± 2.2	...
186	< 2.1	< 1.2	< 7.2
187	3.1 ± 0.5	< 1.2	4.5 ± 1.2	116.9 ± 4.6	...	131.4 ± 7.6
188	4.2 ± 1.2	4.3 ± 0.5	< 5.3	47.5 ± 7.6	49.3 ± 3.1	...
189	< 4.8	4.5 ± 1.3	< 17.3	...	173.2 ± 7.9	...
190	2.1 ± 0.3	1.15 ± 0.11	1.40 ± 0.20	19.0 ± 3.4	40.3 ± 2.6	26.9 ± 3.9
191	0.59 ± 0.07	0.98 ± 0.05	0.78 ± 0.17	106.2 ± 3.4	97.4 ± 1.4	122.0 ± 6.2
192	< 9.0	< 5.5	< 21.6
193	< 1.2	< 0.9	< 3.9
194	< 11.8	5.2 ± 1.2	< 7.8	...	47.2 ± 6.2	...
195	< 4.5	4.1 ± 0.8	< 8.2	...	54.2 ± 5.6	...
196	< 5.2	2.8 ± 0.8	< 8.5	...	52.1 ± 7.6	...
197	< 3.8	< 3.9	< 13.2
198	0.22 ± 0.05	0.38 ± 0.03	< 0.3	75.7 ± 6.3	97.0 ± 2.4	...

TABLE 2—Continued

Source	P_J (%)	P_H (%)	P_{K_s} (%)	θ_J ($^\circ$)	θ_H ($^\circ$)	θ_{K_s} ($^\circ$)
199	< 14.4	6.6 ± 1.8	< 22.3	...	73.0 ± 7.7	...
200	8.8 ± 1.0	6.56 ± 0.06	4.04 ± 0.04	77.4 ± 3.3	76.9 ± 0.3	70.8 ± 0.2
201	0.46 ± 0.11	0.49 ± 0.10	< 0.8	86.6 ± 6.5	110.3 ± 5.9	...
202	3.5 ± 0.9	< 1.7	< 3.6	35.1 ± 6.9
203	< 11.4	5.3 ± 0.6	< 2.1	...	79.9 ± 3.2	...
204	< 2.4	1.7 ± 0.5	< 8.0	...	61.9 ± 7.8	...
205	< 10.2	< 5.5	< 18.6
206	< 9.5	4.7 ± 1.5	< 10.7	...	92.7 ± 8.9	...
207	< 12.3	< 5.2	< 15.8
208	< 10.3	4.5 ± 0.8	< 5.5	...	43.1 ± 5.2	...
209	9.2 ± 0.7	6.2 ± 0.3	< 2.9	47.9 ± 2.2	49.1 ± 1.6	...
210	< 14.2	4.6 ± 0.6	3.2 ± 0.6	...	74.3 ± 3.7	70.3 ± 5.0
211	< 5.7	2.4 ± 0.3	2.2 ± 0.3	...	66.0 ± 3.2	66.7 ± 4.3
212	0.53 ± 0.07	0.71 ± 0.06	< 0.7	94.2 ± 3.6	118.4 ± 2.3	...
213	< 2.3	< 1.59	< 3.4
214	< 0.5	< 0.44	< 1.5
215	13.0 ± 3.4	7.2 ± 1.5	< 11.5	63.0 ± 7.3	59.0 ± 5.7	...
216	0.477 ± 0.013	0.493 ± 0.013	0.33 ± 0.02	99.6 ± 0.8	87.3 ± 0.7	41.1 ± 1.8
217	0.57 ± 0.05	0.94 ± 0.04	0.62 ± 0.14	91.0 ± 2.4	111.5 ± 1.2	90.7 ± 6.2
218	7.19 ± 0.06	4.71 ± 0.03	...	78.3 ± 0.2	80.0 ± 0.2	...
219	< 8.6	< 4.0	< 13.6
220	0.95 ± 0.06	0.59 ± 0.04	0.66 ± 0.07	111.7 ± 1.9	103.9 ± 1.7	64.5 ± 3.1
221	< 1.1	< 0.9	< 3.7
222	< 0.6	0.50 ± 0.14	< 1.7	...	97.3 ± 7.5	...
223	1.09 ± 0.08	1.07 ± 0.04	0.59 ± 0.08	40.7 ± 2.0	59.7 ± 1.0	45.3 ± 3.9
224	< 4.2	< 3.2	< 12.6
225	7.3 ± 0.4	4.90 ± 0.16	2.8 ± 0.4	45.9 ± 1.7	45.5 ± 1.0	49.0 ± 4.1
226	< 20.9	< 7.5	< 5.4
227	6.4 ± 2.0	3.9 ± 0.2	2.51 ± 0.17	91.4 ± 8.3	99.5 ± 1.5	98.4 ± 1.9
228	7.0 ± 1.3	5.6 ± 0.5	3.5 ± 0.4	84.7 ± 5.1	87.0 ± 2.6	81.3 ± 3.1
229	3.1 ± 1.0	3.0 ± 0.3	1.7 ± 0.5	32.8 ± 8.5	33.4 ± 2.6	21.5 ± 8.0
230	1.2 ± 0.3	< 0.7	< 1.0	36.7 ± 7.5
231	1.24 ± 0.13	0.81 ± 0.09	0.59 ± 0.19	76.0 ± 2.9	75.6 ± 3.0	70.6 ± 8.9
232	< 9.4	< 11.1	< 26.3
233	< 3.3	2.3 ± 0.4	< 3.228	...	132.9 ± 5.1	...
234	< 11.3	< 1.5	< 1.3
235	1.0 ± 0.2	0.79 ± 0.10	< 0.5	140.2 ± 5.9	138.8 ± 3.4	...
236	4.0 ± 0.3	2.43 ± 0.15	3.1 ± 0.6	56.8 ± 2.2	54.0 ± 1.7	66.1 ± 5.1
237	< 8.3	5.9 ± 1.0	< 11.6	...	79.8 ± 4.7	...
238	2.1 ± 0.3	1.21 ± 0.17	1.6 ± 0.5	112.1 ± 3.5	105.8 ± 3.9	85.7 ± 7.7
239	0.33 ± 0.06	0.62 ± 0.06	0.7 ± 0.1	148.1 ± 4.9	118.2 ± 2.5	...
240	9.06 ± 0.15	6.47 ± 0.05	4.09 ± 0.06	86.4 ± 0.5	88.0 ± 0.2	...
241	8.0 ± 0.5	5.80 ± 0.10	4.17 ± 0.04	91.5 ± 1.7	97.8 ± 0.5	...
242	0.64 ± 0.11	< 0.25	< 0.9	154.0 ± 4.7
243	5.3 ± 1.6	2.7 ± 0.5	2.0 ± 0.5	91.1 ± 8.4	91.7 ± 4.7	92.5 ± 7.5
244	0.52 ± 0.03	0.67 ± 0.02	0.44 ± 0.06	156.1 ± 1.9	144.6 ± 1.0	29.7 ± 3.5
245	< 7.7	5.5 ± 0.7	< 5.0	...	37.4 ± 3.7	...
246	0.18 ± 0.02	0.44 ± 0.02	0.69 ± 0.05	68.4 ± 3.5	79.3 ± 1.5	58.9 ± 2.2
247	3.6 ± 0.5	3.51 ± 0.13	2.3 ± 0.4	12.0 ± 4.0	5.4 ± 1.0	171.2 ± 4.5
248	6.1 ± 1.6	3.0 ± 0.8	< 9.6	51.9 ± 7.3	40.6 ± 7.1	...
249	< 23.0	3.6 ± 0.7	< 2.0	...	122.4 ± 5.4	...
250	1.76 ± 0.03	1.756 ± 0.017	0.67 ± 0.03	108.4 ± 0.5	112.5 ± 0.3	116.4 ± 1.2
251	4.8 ± 1.0	4.4 ± 0.3	< 1.5	114.2 ± 5.7	105.9 ± 1.9	...
252	< 1.0	< 0.67	< 3.1
253	< 13.5	< 7.0	< 33.3
254	< 8.1	< 7.1	< 29.3
255	< 20.9	10.5 ± 2.0	< 5.5	...	114.5 ± 5.3	...
256	1.44 ± 0.16	1.18 ± 0.15	< 1.4	66.3 ± 3.2	63.8 ± 3.5	...
257	7.5 ± 1.0	4.0 ± 0.4	< 4.2	39.7 ± 3.6	53.7 ± 2.9	...
258	0.799 ± 0.14	0.80 ± 0.10	< 0.9	126.4 ± 4.9	127.7 ± 3.4	...
259	2.9 ± 0.9	< 1.6	< 6.5	51.1 ± 8.2
260	< 2.4	< 2.1	< 8.0
261	< 18.0	< 6.1	< 18.2
262	< 11.9	< 6.3	< 17.0
263	< 27.5	< 6.3	< 12.4
264	< 19.3	9.4 ± 1.8	< 15.2	...	45.4 ± 5.3	...

TABLE 2—Continued

Source	P_J (%)	P_H (%)	P_{K_s} (%)	θ_J ($^\circ$)	θ_H ($^\circ$)	θ_{K_s} ($^\circ$)
265	1.44 ± 0.08	1.59 ± 0.05	0.84 ± 0.14	74.4 ± 1.5	80.6 ± 1.0	60.2 ± 4.8
266	< 0.7	< 0.53	< 2.4
267	1.58 ± 0.12	1.58 ± 0.05	1.50 ± 0.09	64.2 ± 2.1	68.6 ± 0.8	61.6 ± 1.7
268	2.8 ± 0.3	1.94 ± 0.20	< 2.0	107.3 ± 2.6	103.3 ± 2.9	...
269	< 2.2	2.3 ± 0.5	< 7.5	...	74.7 ± 6.4	...
270	< 6.3	5.4 ± 1.8	< 19.1	...	109.1 ± 8.8	...
271	< 1.5	< 1.18	< 5.1
272	< 1.1	< 0.8	< 2.7
273	1.41 ± 0.14	1.0 ± 0.05	1.30 ± 0.11	12.8 ± 2.7	38.0 ± 1.5	43.1 ± 2.4
274	6.9 ± 1.7	3.1 ± 0.6	< 3.5	42.7 ± 6.7	47.2 ± 5.1	...
275	0.61 ± 0.12	0.28 ± 0.08	< 1.1	105.5 ± 5.7	108.3 ± 7.9	...
276	3.1 ± 0.8	< 1.85	< 7.1	78.7 ± 7.5
277	< 0.8	< 0.6	< 2.0
278	0.32 ± 0.06	0.35 ± 0.04	< 0.4	116.2 ± 5.4	118.6 ± 3.4	...
279	7.8 ± 2.2	3.0 ± 0.7	< 3.7	87.6 ± 7.9	99.6 ± 6.4	...
280	< 14.0	< 1.8	< 3.8
281	< 0.7	< 0.53	< 1.4
282	< 15.1	4.5 ± 1.3	< 16.3	...	96.4 ± 8.1	...
283	0.44 ± 0.14	0.65 ± 0.08	< 0.9	156.5 ± 8.6	139.1 ± 3.6	...
284	< 0.6	0.80 ± 0.11	< 8.5	...	20.7 ± 3.9	...
285	0.98 ± 0.08	0.64 ± 0.04	0.61 ± 0.08	61.6 ± 2.2	59.6 ± 1.8	53.6 ± 3.5
286	< 12.2	< 6.8	< 29.3
287	5.33 ± 0.16	4.56 ± 0.08	3.65 ± 0.20	60.6 ± 0.9	65.9 ± 0.5	66.6 ± 1.6
288	< 1.7	< 1.4	< 6.1
289	2.13 ± 0.18	1.48 ± 0.11	1.4 ± 0.4	109.5 ± 2.4	111.1 ± 2.2	102.3 ± 7.6
290	4.3 ± 1.2	3.4 ± 0.6	< 5.0	51.1 ± 7.4	64.5 ± 5.1	...
291	< 0.16	0.76 ± 0.03	0.48 ± 0.08	...	103.7 ± 1.1	79.0 ± 4.8
292	< 5.7	3.0 ± 0.7	< 11.2	...	50.5 ± 6.8	...
293	< 19.7	< 5.3	< 17.6
294	< 0.68	0.60 ± 0.19	< 2.2	...	53.8 ± 8.5	...
295	1.2 ± 0.3	1.68 ± 0.20	< 2.0	125.9 ± 7.4	109.8 ± 3.3	...
296	0.73 ± 0.13	0.26 ± 0.08	< 0.9	96.5 ± 4.9	87.4 ± 8.1	...
297	< 16.4	< 5.6	< 22.6
298	< 15.5	< 4.3	< 13.2
299	4.2 ± 0.9	2.7 ± 0.4	< 5.8	13.4 ± 5.9	24.8 ± 4.2	...
300	3.0 ± 0.8	2.4 ± 0.2	< 1.6	77.5 ± 7.3	77.3 ± 2.7	...
301	4.35 ± 0.17	2.75 ± 0.08	1.88 ± 0.18	74.6 ± 1.1	72.4 ± 0.8	63.7 ± 2.8
302	< 2.5	< 2.4	< 9.8
303	1.07 ± 0.10	0.30 ± 0.05	< 0.4	37.1 ± 2.6	54.3 ± 4.9	...
304	0.79 ± 0.06	0.81 ± 0.05	1.4 ± 0.2	62.5 ± 2.0	71.6 ± 1.8	76.8 ± 4.3
305	< 5.1	< 5.1	< 17.9
306	0.50 ± 0.04	0.56 ± 0.04	0.53 ± 0.14	47.2 ± 2.4	67.6 ± 2.0	70.9 ± 7.1
307	9.0 ± 2.9	< 6.2	< 17.3	88.4 ± 8.8
308	7.6 ± 1.1	4.4 ± 0.3	2.8 ± 0.6	83.6 ± 4.2	71.3 ± 1.7	70.2 ± 6.2
309	10.0 ± 2.7	< 3.8	< 9.2	110.7 ± 7.4
310	< 17.4	< 5.1	19.4 ± 5.3	30.2 ± 7.5
311	1.33 ± 0.19	0.82 ± 0.13	< 1.8	67.1 ± 4.0	42.8 ± 4.5	...
312	1.97 ± 0.14	1.38 ± 0.07	0.69 ± 0.14	72.2 ± 2.0	66.9 ± 1.4	54.0 ± 5.6
313	1.3 ± 0.2	1.74 ± 0.13	< 1.3	45.5 ± 4.4	43.4 ± 2.2	...
314	5.4 ± 0.7	< 2.4	1.6 ± 0.4	74.2 ± 3.9	...	41.5 ± 6.6

NOTES.—For sources with $P/\delta P < 3$, the $3\delta P$ upper limits are listed.